Atomic Layer Deposition of Environmental Barrier Coatings for Preventing Hydrogen Ingress

By

Sarah Kathleen Bull

B.S., Yale University, 2016

M.S., University of Colorado Boulder, 2017

A thesis submitted to the Faculty of the Graduate School of the University of Colorado in partial fulfillment of the requirement for the degree of Doctor of Philosophy

Department of Chemical Engineering

2021

Committee members:

Alan W. Weimer

Charles B. Musgrave

Sanghamitra Neogi

J. William Medlin

David Marshall

Sarah Kathleen Bull (Ph.D., Chemical Engineering)

Atomic Layer Deposition of Environmental Barrier Coatings for Preventing Hydrogen Diffusion

Thesis directed by Professor Alan W. Weimer and Professor Charles B. Musgrave

Hydrogen is an essential element of the energy industry from fuel cells to nuclear reactors and engines. However, its small molecular weight, which makes it attractive for these applications, also allows it to easily diffuse through materials and embrittle them. Hydrogen-induced damage includes increased ductile to brittle transition temperatures, precipitation of hydrides, and decreased interfacial strength between grains due to surface stabilization. Environmental barrier coatings (EBCs) can be used to alleviate hydrogen embrittlement by reducing ingress of the damaging element into susceptible substrates and thereby extend material lifetimes.

Barrier material choice, which determines hydrogen diffusivity, and coating method, which determines microstructure and defect type and concentration, are both essential in forming an effective hydrogen EBC. In this work, density functional theory is used to screen high temperature materials to determine those with the largest activation energy and therefore lowest predicted diffusivity resulting in *h*-BN, *c*-BN, HfN, ZrN, and WC predicted to perform better than the legacy material, W, for high temperature hydrogen permeation prevention. Properties including diffusing hydrogen charge state, strain energy, and redistribution of electron density were compared to trends in the magnitude of activation energy. In addition, nitrogen vacancy formation energies with respect to gaseous nitrogen and ammonia formation were used to predict nitrogen retention at elevated temperatures.

Atomic layer deposition (ALD) was used to deposit coatings of WN (decomposes to W) and BN for thermal testing. ALD uses sequential, self-limited surface reactions to form conformal,

pinhole-free coatings that are chemically bonded to the substrate. Because BN was predicted to perform well regardless of crystal structure, it was chosen to compare against W. Coatings from WN and BN were conformal and uniform on the substrate surface. The film growth rate for BN was much faster than that of WN allowing for deposition of thicker barrier coatings of BN on the same time scale. Thermal testing in 6% hydrogen atmosphere up to 1770 K confirmed both the inert character of the BN coating compared to the WN/W coating and the computational predictions of BN as an improved material choice over the legacy material, W.

To my family and my friends that have become family

Acknowledgements

Throughout my PhD work I have had the opportunity to work with collaborators both across states and agencies as well as within CU Boulder. Through them, I have learned an incredible amount outside the research reported in this document. My PhD studies were co-advised by Prof. Alan Weimer and Prof. Charles Musgrave whom I cannot thank enough for their mentorship and support. Under there guidance, I have had the freedom to pursue the aspects of my research project that interest me most and grow as a researcher yet received the assistance I needed be it for new techniques or roadblocks. They have helped shape my abilities not only to research, but also to present, write, and network. My PhD path has allowed me to spend significant time with them travelling to conferences, collaborator meetings, and grant reviews outside the official work schedule and truly showed the support they have for their graduate students. I have appreciated their academic discussions when I bring new data to our meetings and often their pep-talks when experiments do not go as planned.

I would also like to thank my many unofficial advisors and mentors. Firstly, Dr. Sai Raj (NASA GRC) for his input on our data, lively discussions, and support. Our monthly discussions helped me analyze data and plan next steps throughout the project. My PhD project also brought me to Idaho National Lab where I had the unique opportunity to learn from experts in the nuclear field. I would like to thank Dr. Robert O'Brien (INL) for making this experience possible and Dr. Bob Fox (INL) for adopting me into his group to work on my graduate fellowship project. I would also like to thank Cindi Adkins (INL) for teaching me DTA, Scott Middlemas (INL) for running samples on the DTA, and Byron White (INL) for training me on ceramic digestions and ICP. Dragan Mejic, Lucas Jones, and Maria Toscano-Leary at CU have all helped me in constructing

and maintaining my lab equipment at CU. Hans Funke has been an invaluable help in ALD reactor design and equipment debugging throughout this process.

Thank you to my lab-mates in both the Weimer and Musgrave groups for the shared academic knowledge and the friendships that extend off the campus. Wilson McNeary and Amanda Hoskins trained me on operating a fluidized bed ALD reactor. Jacob Clary, Chris Bartell and Zach Bare answered endless questions about DFT. Justin Tran, Kent Warren, and Julia Hartig offered useful discussion of experimental issues and data analysis. Hailey Loehde-Woolard always lent a hand with reactor maintenance and brought the best baked goods. Becky O'toole has discussed all reactor issues, sample characterization, DFT results and data I have ever collected with me as well as run samples on SEM. We joined our lab groups at the same time and I have been incredibly fortunate in having such a close friend throughout grad school. Three of my five grad-school years Theo Champ worked as an undergraduate researcher on my project contributing both computationally and experimentally. Maddie McGrath and Chanel Hill have also contributed their time to experimental work.

My strong support system outside the lab has celebrated my graduate school wins with me and helped me endure the late nights and lesser sides. I would like to thank my fiancé Noah Adelman who made these years in Boulder so much more fun. I am also lucky to have two brothers whose chemical engineering PhD studies overlapped with mine, including one in the lab just above mine. David and Michael Bull, thank you for listening to my research spiels and for distracting adventures on the weekends. I would also like to thank my parents, Ruth and Larry Bull, for their support often via home cooked meals and encouraging words.

I have had various fellowships and grants to support my work at CU throughout the last five years including NASA Early Stage Innovations, Department of Education's GAANN Fellowship, and Idaho National Lab's Graduate Fellowship.

Table of Contents

List of Tables

List of Figures

Chapter 1

Introduction

1.1 Overview of hydrogen-induced damage

Hydrogen is an essential element of the energy industry utilized in applications from fuel cells [1] and heat generation [2] to the plasma source in terrestrial nuclear reactors for electricity production [3, 4], and even as a propellant for in-space propulsion systems [5]. However, hydrogen is also responsible for damaging materials via hydrogen embrittlement, hydrogen-induced blistering, hydrogen-induced cracking, and hydrogen stress cracking [6-13]. Its small mass which makes it desirable for these applications also allows for large permeation rates and hydrogen damage. Johnson first described the loss of ductility of metals when immersed in acid in 1875 [14] sparking research reported in over 38,000 journal articles since then [15]. Hydrogen induced damage has been proposed due to a multitude of mechanisms: pressure buildup from bubbles, reduction in surface energy, enhanced dislocation ejection, reduction in cohesive strength, enhanced localized plasticity (HELP), vacancy production, increased ductile to brittle transition temperature, brittle hydride formation, and phase transformations [7].

Absorption of hydrogen is preceded by dissociation of the diatomic molecule (H_2) on material surfaces followed by atomic diffusion through the bulk of nascent hydrogen (H) [8]. The atom can then occupy an interstitial site in the perfect crystal lattice or become trapped at a defect site such as a vacancy, grain boundary, or dislocation core as shown in Figure 1.1 [16]. The concentration of H in defect sites often exceeds that of H dissolved in the lattice, and H's interaction with these defects forms the foundation for the proposed mechanisms of hydrogen damage [8].

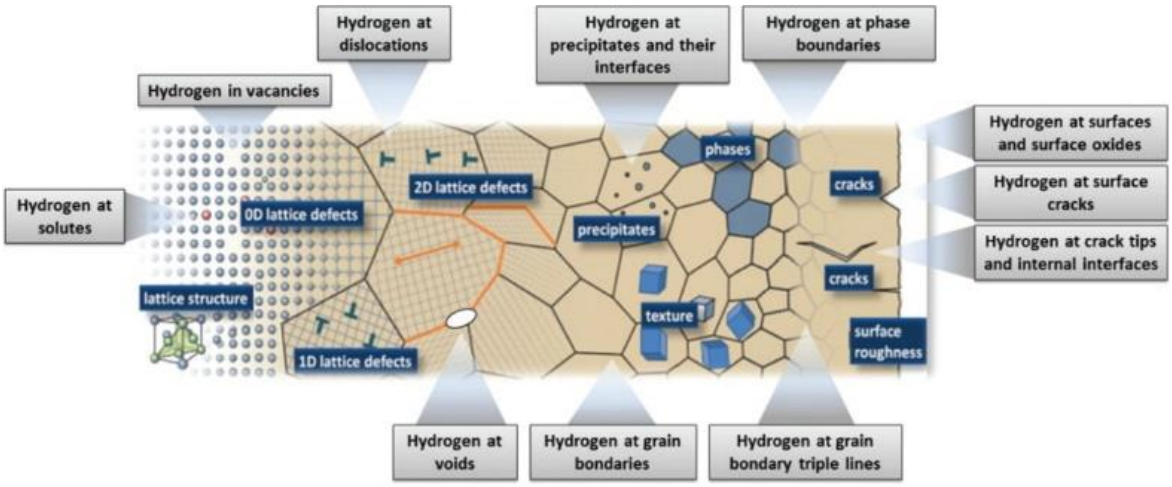

Figure 1.1 Potential hydrogen-trapping defect sites. Reproduced from Koyama [16].

Hydrogen can be introduced during material fabrication and processing leading to internal hydrogen embrittlement (IHE) or from the application atmosphere leading to hydrogen environmental embrittlement (HEE). The studies detailed in this work address the second type, hydrogen environmental embrittlement, through development of environmental barrier coatings (EBCs) also referred to as permeation barrier coatings that prevent the ingress of hydrogen into susceptible materials. Furthermore, these coatings seek to prevent unnecessary fuel loss through outward diffusion in hydrogen storage and transport applications. The work presented in this dissertation focuses on the improvement of hydrogen EBCs through both the choice of deposition method and selection of the barrier material. This chapter overviews: applications requiring the mitigation of hydrogen diffusion and its concomitant embrittlement, discussion of previous reports of EBCs either used for preventing hydrogen diffusion or for peripheral applications but formed from the materials probed in this dissertation, atomic layer deposition (ALD) – the coating method utilized, a brief overview of density functional theory – the computational method employed in this work, and finally descriptions of the project objectives.

1.2 Applications afflicted by hydrogen-induced damage

1.2.1 Nuclear thermal propulsion

Nuclear thermal propulsion (NTP) engines that utilize hydrogen as a propellant are an attractive alternative to chemical combustion engines (hydrogen and oxygen) for in-space propulsion systems because they can achieve twice the specific impulse [5]. This improvement requires the use of hydrogen as compared to alternative, more inert gases due to the dependence of specific impulse on the molecular mass of the propellant [17]. These NTP engines function by heating hydrogen to ~2700 K before expelling it from a supersonic nozzle to generate thrust [18]. Hexagonal-shaped cermet (i.e. ceramic-metallic) fuel elements containing uranium-based nuclear fuel embedded in a metallic, often tungsten (W), matrix are used to heat the hydrogen propellant using energy released from fission. Hydrogen flow channels up to only 3 mm in diameter while 1 m in length are used to maximize the interfacial surface area between the propellant and the heat-generation source. These fuel elements (Figure 1.2), however, are subject to hydrogen embrittlement causing critical fuel loss [19] such as is seen in the cracked surrogate (W-HfN) fuel element (Figure 1.3) tested by Hickman et al [20].

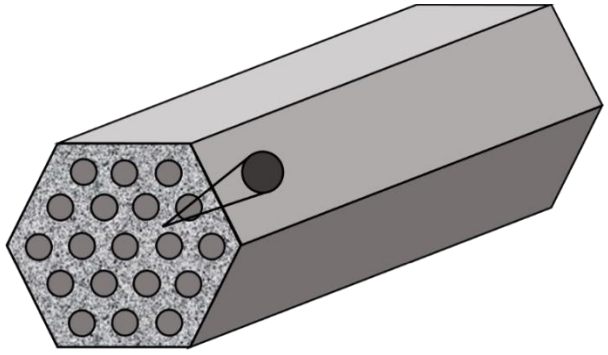

Figure 1.2 Hexagonal cermet fuel element design used to heat the hydrogen propellant. Enlarged image is used to highlight presence of uranium-based fuel kernels embedded in the tungsten matrix. Hydrogen flow channels are present throughout the length of the element.

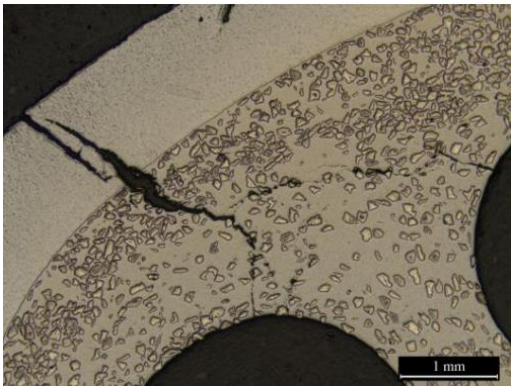

Figure 1.3 Cracked surrogate fuel element of W-HfN after 3 hours of hot hydrogen testing at 2073 K reproduced from Hickman et al. [20]

Hydrogen will attack the cermet fuel elements through formation of lower density hydrides [10, 21] and H_2 bubbles [22, 23], and surface stabilization at grain boundaries [7, 8, 24]. Previously, W EBCs have been applied to uranium oxide fuel pellets via chemical vapor deposition (CVD) before incorporation within the cermet elements, however the coatings were non-uniform and contained low-energy diffusion pathways for hydrogen to diffuse into the susceptible substrate [25]. The best method to protect the fuel, however, is to prevent its direct interaction with hydrogen by reducing the amount of these diffusion pathways. In addition, CVD utilizes gas-phase reactions to form barrier coatings, thereby depositing non-uniformly within high aspect ratio channels. This prevents it from conformally coating the length of high-aspect-ratio channels such as the hydrogen flow channels within the cermet fuel elements as shown in Figure 1.2 [26, 27].

1.2.2 Nuclear fusion power plants

Fusion power plants offer a sustainable method of generating electricity from the significant energy released through combining atomic nuclei: deuterium and tritium to form helium. This attractive reaction releases energy without forming carbon dioxide and from fuel sources that can both be extracted from seawater [28, 29]: deuterium and lithium (used to breed tritium). In addition, fusion avoids the possibility of a criticality accident such as that feared in

nuclear fission plants [30]. The fusion plant design requires barrier coatings on steel-based structural materials to prevent hydrogen embrittlement, buildup of radioactive isotopes in the plant, and diffusion into the water coolant as well as into areas with personnel in addition to withstanding irradiation and mechanical stresses [31, 32]. Much of the research regarding the interaction of hydrogen isotopes with tungsten and the development of hydrogen isotope permeation barriers arises from the nuclear community in regards to fusion reactor design.

1.2.3 The hydrogen economy and hydrogen fuel cells

As atmospheric carbon dioxide levels and global temperatures increase, so does the need for developing carbon-free energy pathways. A major movement in the clean energy sector to replace fossil fuels with hydrogen as an energy carrier accompanied by utilization of fuel cells to convert hydrogen-based fuel sources into electricity and heat is referred to as "The Hydrogen Economy." Hydrogen fuel cells react hydrogen with an oxidant to generate electricity. When using oxygen as the oxidant, these electrochemical devices produce electricity with only water as the byproduct. This technology is already utilized in public buses in the USA, Canada, across Europe, and Japan [33]. Successful implementation of fuel cell vehicles and on-site electricity generation requires use of materials that resist hydrogen permeation and embrittlement for hydrogen-facing components in these devices as well as in the transport and storage infrastructure necessary for refueling [11, 34].

1.3 Environmental barrier coatings to address hydrogen permeation

Environmental barrier coatings have the potential to limit hydrogen diffusion and enable the use of new technologies. Various growth methods and barrier materials have previously been investigated under the limitations of substrate type and application temperature. These systems have included pure metals, graphite, carbides, nitrides, and oxides, and have been formed via

aluminizing and oxidation [12, 31, 35, 36], atomic [37] and chemical [31, 38] vapor deposition, magnetically enhanced plasma ion plating [39], and packed-bed cementing [31]. Research is constantly focused on methods to decrease diffusivity and improve compatibility with the substrate material. The research presented in this dissertation focuses on computational analysis of better barrier materials and experimental analysis of three EBC materials: tungsten nitride, tungsten, and boron nitride deposited via ALD. These materials have been studied by previous researchers either using alternate deposition methods or testing in non-reducing atmospheres as summarized below.

1.3.1 Tungsten

Tungsten is the current state-of-the-art material in both NTP engines as well as for plasma-facing materials in fusion reactors due to its high melting point (3,410°C), retained strength at elevated temperatures, high thermal conductivity, and low H retention [24]. Much of the research regarding H in W stems from the nuclear field [24, 40-46]. The activation energy of at least 1.8 eV for atomic H absorption into W (110) is much larger than that of other pure metals [24, 41, 47]; however, it is not sufficiently high to avoid H absorption at temperatures above ~300°C. Furthermore, W exhibits H-induced vacancy formation [42], H trapping and bubble formation in lattice vacancies [24, 48], and blistering [49] which can further lead to crack propagation [24]. EBCs must effectively prevent interaction between H and susceptible substrates to avoid corrosion.

1.3.2 Tungsten nitride

Tungsten Nitride (WN) is widely used in the semiconductor industry as a copper diffusion barrier deposited via reactive magnetron sputtering, CVD, and ALD [50, 51]. Although its stability has been observed in these applications up to 600°C [50, 52], higher temperatures will decompose the nitride to pure W and gaseous nitrogen (N_2) [37, 53]. However, WN is still attractive to deposit via ALD for high temperature hydrogen EBC applications given the conformal deposition on metal

oxide substrates using the organometallic tungsten precursor in place of direct W deposition using WF_6 as a precursor, which is substrate-selective with the potential to etch [54].

1.3.3 Boron nitride

Thermal ALD often deposits amorphous films which can be crystallized with annealing and additional treatments. The low pressures of the ALD system limit crystallization of amorphous-deposited boron nitride (BN) films to the hexagonal layered structure (*h*-BN) [52, 55-57], as crystallization to the cubic phase requires high pressures (>5.5 GPa) and temperatures (>1773 K) [58]. Previous experimental studies, however, have examined both *h*-BN and cubic BN (*c*-BN) in the context of hydrogen diffusion with favorable results. Deposition of 1 μm of *c*-BN using a 0.5 μm thick SiC tie layer on steel substrates reduction permeability by up to two orders of magnitude in [39, 59].

The dependence of permeability on microstructure is extremely evident in *h*-BN due to its anisotropic crystal structure. Varying the deposition method of *h*-BN varies the orientation of its (002) planes thereby creating either channels for H to enter the substrate or effectively reducing diffusion. Ion beam assisted deposition (IBAD) of *h*-BN resulted in (002) planes oriented perpendicular to the substrate allowing facile diffusion and negligible film efficacy [59]. However, permeability was observed to reduce through deposition of polycrystalline *h*-BN films deposited via radio frequency magnetron sputtering [60]. In addition, He et al. observed the ability of *h*-BN flakes parallel to their substrate surface to trap H_2 bubbles up to 1073 K without outward diffusion [61]. These previous studies that underline the importance of microstructure on efficacy of BN films support the investigation of starting with an amorphous BN film deposited via ALD that can then be annealed to compare to the *h*-BN films and *c*-BN films already analyzed.

1.4 **ALD overview**

Materials investigated experimentally in this dissertation were deposited using ALD. ALD, sometimes referred to as atomic layer epitaxy, is a subcategory of CVD. The method utilizes sequential, self-limited surface reactions to build a chemically-bonded coating. Often, two precursors are used with each determining its own "half-reaction" and together defining one full ALD cycle as shown in Figure 1.4 reproduced from Grillo et al [62]. The separation of half-reactions by inert gas purges results in a conformal and low-defect film that is chemically bonded to the substrate [27, 63, 64]. This is extremely important in the application of barrier coatings to prevent the formation of avoidable low-energy diffusion pathways in comparison with other vapor deposition methods.

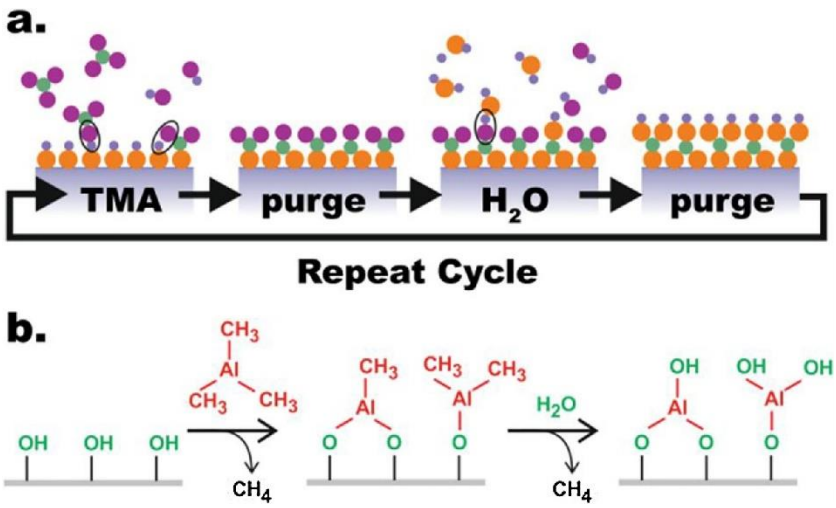

Figure 1.4 Mechanism for a single ALD cycle of alumina reproduced from Grillo et al. [62]

Because ALD half-reactions are self-limited and are not line-of-site dependent, high-aspect-ratio features such as pores and channels as well as nanoparticles can be coated [26, 27, 63]. Particle ALD utilizes a fluidized bed apparatus such as that shown in Figure 1.5 [65]. This allows for conformally coating particles without agglomeration. The uniformity of coatings from ALD is observed on both high specific surface area particles and low surface area substrates (Figure 1.6).

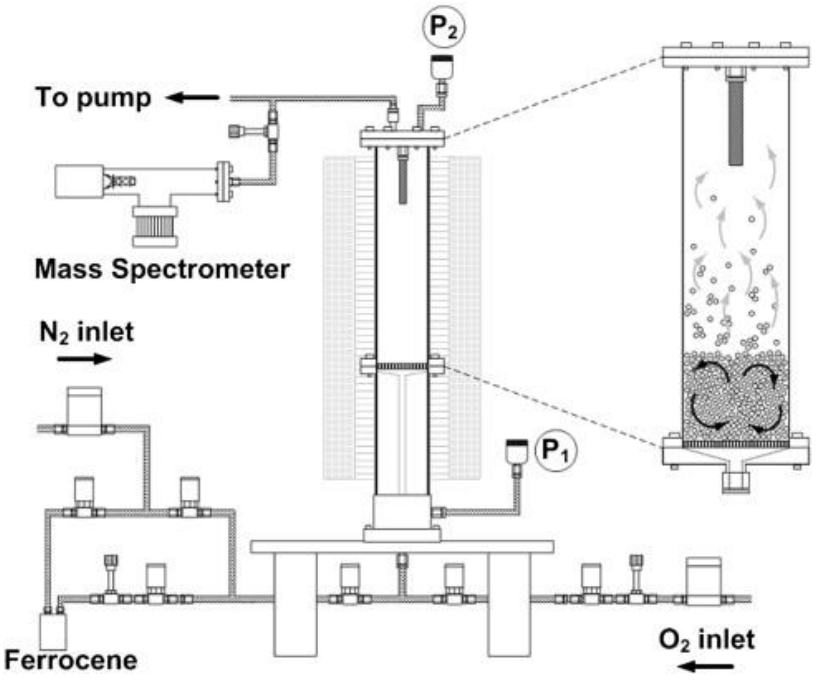

Figure 1.5 Example fluidized bed as used in this work reproduced from Scheffe et al. [65].

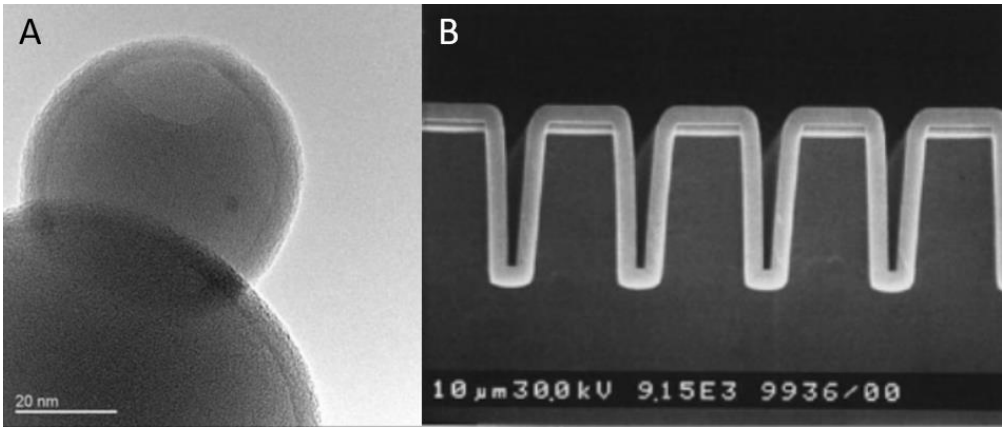

Figure 1.6 Examples of conformal alumina ALD films of 5 nm on nanoparticles (A) reproduced from Hakim et al. [66] and 300 nm on a silicon wafer (B) reproduced from Ritala et al. [67]

1.5 **DFT overview**

Computational analysis presented in this dissertation relies on the use of Vienna Ab Initio Simulation Package (VASP) which employs density functional theory (DFT) to calculate the energy of user-defined systems using periodic boundary conditions, either the strongly constrained and appropriately normed semilocal density functional (SCAN) or Perdew-Burke-Ernzerhof

(PBE) GGA method as noted in the individual chapter's methods sections and projector augmented wave (PAW) pseudopotentials [68-73].

The solution to the time-independent, many-body Schrodinger's equation [74]:

$$\hat{H}|\Psi\rangle = E|\Psi\rangle \qquad \text{Equation 1.1}$$

where $\hat{H}$ is the Hamiltonian operator, Ψ the wave function, and E the expectation energy value of the system under the Born-Oppenheimer approximation [75] reveals not only the ground state energy of a system, but would also allow for observable properties to be extracted from the wave function. However, there is no practical manner in which to solve Equation 1.1 for a solid. To create a more tractable problem that can be solved using available supercomputing resources, DFT relies on the Hohenberg-Kohn Theorems [76] with further development by Kohn and Sham [77]. The two Hohenberg-Kohn Theorems state that firstly, the electron density of a system can be used to calculate ground-state properties and secondly, the energy functional of a system is minimized when the ground state electron density is used. These theorems replaced the need to define the ground-state energy of a system in terms of a wave function dependent on N electrons to instead use the electron density at a single point. Kohn and Sham later added to these theorems to form the basis of Kohn Sham DFT by using non-interacting electrons in an effective potential in place of interacting electrons in a static potential. These developments allowed for definition of the Kohn-Sham equations:

$$\left(-\frac{\hbar^2}{2m}\nabla^2 + v_{eff}(r)\right)\varphi_i(r) = \varepsilon_i\varphi_i(r) \qquad \text{Equation 1.2}$$

$$n(r) = \sum_i^N |\varphi_i(r)|^2 \qquad \text{Equation 1.3}$$

Where φ_i is the one-electron wave function, ε_i is the eigenstate of the orbital described by the wave function, v_{eff} is a functional describing the electron-electron interactions, and n is the electron

density. The electron interactions contained in v_{eff} require an approximation of the exchange correlation energy of the electrons and utilization of more accurate functionals improves the prediction of a material's energy and associated properties. However, increased accuracy of this functional requires increased computational expense and a balance must be chosen based on the requirements of the study.

1.6 Previous uses of ALD for EBCs

The ALD process is heavily rooted in the semiconductor industry which relies on the method to deposit within the high-aspect-ratio features of micro-electronic devices [78]. This includes deposition of diffusion barrier materials to prevent copper migration and has led to significant research on increasing the maximum operating temperature, layer adhesion, and electrical conductivity while minimizing defects [78] in these barriers layers. This has resulted in published investigations of ALD of metals and metal nitrides including Ta/TaN [79], TiN [80, 81], W [82], WN [50], WN_xC_y [83], and WC [84]. Deposition of environmental barrier coatings via ALD is beginning to gain traction in other industries such as the use of alumina as a gas diffusion barrier for organic light emitting diodes [85] TiN as a Li diffusion barrier [86] and mullite to prevent oxidation of SiC in aerospace and nuclear applications [87].

1.7 Project objectives

The work detailed in this dissertation sought to improve upon high temperature EBCs by addressing two main issues: coating uniformity and barrier material permeability. This was done through utilization of ALD methods to deposit WN/W and BN and computational screening of refractory materials according to predict hydrogen diffusivity. First, the legacy material for high temperature applications, tungsten, was tested via ALD of WN and decomposition to W. Computational screening revealed BN as the best candidate for experimental testing in comparison

to W. Analysis of H diffusion in high temperature materials was further probed to correlate material characteristics with calculated activation energies for H absorption. Thin BN films were then deposited via ALD and tested to compare against WN/W coatings. The specific objectives of these three research thrusts are described below and outline the sequence of the dissertation.

1.7.1 W via WN

This work analyzed the efficacy of WN deposited via ALD as a hydrogen EBC. Its aim was to deposit a conformal coating with minimum low-energy hydrogen diffusion pathways. A fluidized bed was used to deposit WN via bis(t-butylimido)bis(dimethylamino)tungsten(VI) ((^{t}BuN)$_2$(Me$_2$N)$_2$W) and ammonia on either zirconia nanopowder or yttria stabilized zirconia microspheres. Deposition was characterized on zirconia nanopowder to determine film growth rate before coating YSZ with WN. Barrier performance was probed using differential thermal analysis in either a hydrogen or pure inert atmosphere. Hydrogen was observed to affect the WN/W coatings although increased coating thickness was observed to increase this reaction temperature. The specifics of the deposition and the coating performance are discussed in this section.

1.7.2 Computational Material Screening

Although W was initially experimentally tested due to its status as the legacy material to be used for high temperature hydrogen diffusion, it's large activation energy (E_a) for hydrogen diffusion compared to other pure metals is still less than that of refractory nitrides. Materials with melting points above 2700 K were computationally analyzed to determine their E_as for H diffusion into the first subsurface layer of the most energetically favorable surface. Candidates suggested for experimental testing are those with larger E_as than that of W and the material with the largest E_a, BN, was tested in the subsequent section. Computational methods and the material properties proposed to contribute to larger E_as are described in this work.

1.7.3 BN ALD

In order to confirm the results of the computational screening, BN was deposited via ALD on zirconia and YSZ substrates using BCl_3 and NH_3 precursors. The growth rate was observed much quicker than that of the WN chemistry, allowing for much thicker coatings to address the issue of persistent hydrogen reaction with WN-coated substrates. Samples coated with various BN thicknesses were probed for hydrogen reactivity using differential thermal analysis (DTA) in either H_2 or pure inert atmosphere. Stability of the coating was observed and recommendations for further testing at higher temperatures and hydrogen concentrations were proposed based on these positive results. In addition, DFT was used to further analyze the various diffusion pathways in the anisotropic crystal structure of *h*-BN indicating microstructure will greatly impact barrier efficacy. Details of the deposition and thermal and computational analysis are discussed in this study.

Chapter 2

Atomic Layer Deposition of Tungsten Nitride Films as Protective Barriers to Hydrogen

This chapter appears in the following manuscript:

Bull, Sarah K., W. Wilson McNeary, Cynthia A. Adkins, Theodore A. Champ, Chanel A. Hill, Robert C. O'Brien, Charles B. Musgrave*, and Alan W. Weimer*. Atomic layer deposition of tungsten nitride films as protective barriers to hydrogen. Appl. Surf. Sci. 507, 145019 (2020). [37]

2.1 Abstract

Nanoscale films of tungsten nitride (WN) were deposited as environmental barrier coatings (EBCs) by particle atomic layer deposition (ALD) on zirconia nanoparticles and yttria stabilized zirconia micropowders. Hydrogen diffusion in tungsten (W) was investigated computationally using density functional theory and experimentally using differential thermal analysis of the ALD samples in hydrogen at temperatures >1000°C. Reaction of hydrogen with the underlying material was delayed but not eliminated by the ALD film, consistent with the low computationally predicted hydrogen diffusion barrier in bulk W of 0.19 eV. This is the first study of WN ALD films as EBCs for hydrogen above 1000°C.

2.2 Introduction

Hydrogen (H_2) plays a key role in a variety of advanced energy applications from fuel cells to nuclear thermal rockets [17, 88]. However, the high diffusivity of H_2 into materials and its accompanying degradation of materials that it contacts has hindered its successful utilization. This large diffusivity is in part due to the small size of atomic hydrogen (H), which allows it to permeate more easily into structures than larger species [35]. Environmental barrier coatings (EBCs) for blocking H_2 diffusion are of interest to prevent the embrittlement of underlying substrates and extend their lifetimes. Previously studied coating materials have included pure metals as well as alloys, oxides, nitrides, carbides, and polymers [35, 36, 89, 90].

H_2 has long been considered for plasmas in nuclear fusion reactors and as a propellant for nuclear thermal propulsion [17, 31]. Development of EBCs for the latter application requires that the material withstand the high operating temperature of ~2,500˚C. Furthermore, at these temperatures H_2 and hydrogen radicals ($H^{\bullet}$) resulting from H_2 dissociation readily react with many materials, causing preferential etching and hydrogen embrittlement. In the case of nuclear thermal propulsion engines, H_2 reacts with the uranium (U) fuel to form low-density uranium hydride precipitates. The stress caused by the volumetric expansion of the precipitates subsequently leads to plastic deformation and fracture of the fuel as well as cracking of the coating film [21].

W is currently favored as an EBC material because of its high melting point (3,410˚C), retained strength at elevated temperatures, high thermal conductivity, and low H_2 retention [24]. Adsorption and diffusion of H_2 in W were previously studied in the context of nuclear fuels [24, 40-46, 91]. Density functional theory (DFT) was used to predict high energy barriers of at least 1.8 eV for atomic H absorption into W, suggesting a low concentration of H atoms in W and that W would be a good choice as an EBC [24, 41]. However, these barriers are not sufficiently high to sufficiently limit H absorption at temperatures above ~300˚C. Furthermore, W lattice vacancies are predicted to each trap up to 12 H atoms, which then recombine to form H_2 bubbles [40]. EBCs must effectively inhibit interaction between U and H to avoid corrosion [21]. In addition to examining ALD deposited WN as an EBC to H_2, the research reported herein expands on these studies by investigating charge transfer during diffusion.

Atomic layer deposition (ALD) of conformal and pinhole-free films offers a promising solution to impede the reaction of H_2 with uranium fuel substrates. ALD uses sequential, self-limited surface reactions to build low-defect films atomic layer-by-atomic layer, thereby limiting the number of low energy diffusion pathways [63]. This work focuses on the use of WN ALD to

coat surrogate fuel particles in order to test the efficacy of WN/W films as EBCs for preventing H diffusion. WN deposition was chosen in place of the traditional W chemistry involving tungsten hexafluoride (WF_6) in order to take advantage of the less corrosive ALD precursors of WN and to avoid the formation of hydrogen fluoride as a byproduct, which may etch the substrate. Deposition of WN offers the additional benefit of increased steric hindrance of H diffusion at lower temperatures before decomposing into a pure W film at higher temperatures.

Recent research on ALD of EBCs has shown similar performance between nanometer scale ALD films and micrometer scale films deposited via other techniques. For example, alumina and mullite ALD nanofilms have proven effective in mitigating steam oxidation of silicon carbide at 1,000ºC when compared to chemical vapor deposition and physical vapor deposition [87]. An additional constraint on coating materials as EBCs is that they require similar coefficients of thermal expansion to their substrates to prevent fracture or delamination, especially under thermal cycling and at the high temperatures at which nuclear thermal propulsion engines operate. Refractory metals currently chosen for their high melting point and low neutron absorption tend to exhibit a lower bulk linear thermal expansion coefficient than both uranium nitride (UN) and uranium oxide (UO_2) fuels [92, 93]. Because film elasticity is enhanced by the reduction of film thickness, nanometer scale thin films as deposited by ALD will likely have increased resilience to thermal expansion when compared to micrometer thick films currently used as EBCs [94]. Results obtained here demonstrate that WN/W films can be deposited via ALD and thermal testing shows that these films deposited with 100 ALD cycles increase the reaction temperature of the substrate with H_2 by 38°C.

2.3 Materials and methods

2.3.1 Atomic layer deposition of WN methods

Zirconia nanopowder (U.S. Research Nanomaterials) and 5% yttria stabilized zirconia (YSZ) micropowder (Glen Mills VHD milling powder) were coated with WN in a fluidized bed reactor. Schematics for particle ALD reactors are detailed elsewhere [65, 66, 95]. The ALD system consisted of a heated reactant manifold and reactor tube in a furnace in which fluidization was achieved through adequate flow rates of inert nitrogen carrier gas. Data acquisition and control used LabView™. Baratron capacitance manometers (MKS) were installed both before and after the reactor tube to measure changes in pressure. An in-line mass spectrometer (MS) (Stanford Research Systems QMS 200) tracked relevant m/z peaks to monitor concentration of precursor and reaction byproducts in the outlet gas stream.

The zirconia nanopowder particles had an average diameter of 40 nm with a specific surface area of 11.74 m^2/g. Six grams of powder were loaded into the fluidized bed reactor with no pretreatment and 2 g of powder were removed from the reactor after 10, 25, and 50 ALD cycles, respectively. The YSZ powder had an average diameter of 100 μm and a theoretical specific surface area of 0.01 m^2/g. In a separate deposition run, 8 g of the YSZ was loaded and 4 g was removed after 65 and 100 ALD cycles, respectively. The powder was secured in the reactor tube using two sintered 316SS porous metal filters. The bottom flat filter at the inlet of the precursor and inert gas streams also served as a gas distribution diffusion plate to disperse reactants into the reactor tube.

WN ALD was performed at 300˚C. This temperature is within the ALD window reported by Becker et al. [50, 53]. Tubing to and from the reactor was kept above 60ºC to prevent reactants and byproducts from condensing. The W precursor bubbler was held at 40˚C to increase reactant

vapor pressure. The WN chemistry used includes two precursors: bis(t-butylimido)bis(dimethylamino)tungsten(VI) (($^{t}BuN)_2(Me_2N)_2W$) and high purity ammonia as first described by Becker et al. [50, 53]. ($^{t}BuN)_2(Me_2N)_2W$ was acquired from Strem Chemicals with a purity of at least 97%. Anhydrous ammonia >99.98% was procured from Millipore Sigma. Dosing times depended strongly on the amount of surface area and therefore powder in the reactor. Doses averaged 15 and 20 minutes for ($^{t}BuN)_2(Me_2N)_2W$ and ammonia, respectively, and purges were performed for 45 minutes.

The effects of varied annealing conditions were tested on coated samples at either 700ºC or 725ºC for five hours under 20% H_2 in N_2 flow. The temperatures were chosen per Becker et al. who observed WN crystallization at 700ºC and sublimation of nitrogen and W crystallization at 725ºC when annealing for 30 min in forming gas [53]. Fixed monatomic nitrogen content was determined both before and after these anneals using a LECO TC600 light element analyzer.

The WN deposition rate on zirconia nanopowder was determined by inductively coupled plasma optical emission spectrometry (ICP-OES) (Thermo Scientific ARL 3410+). W weight loading on the 100 WN YSZ sample was determined using inductively coupled plasma mass spectrometry (ICP-MS) (Thermo Scientific iCAP Q). Zirconia nanopowder samples were imaged using a FEI Titan transmission electron microscope (TEM). The 50 WN ALD sample was also imaged with a Tecnai TG30-FEG STwin Scanning TEM (STEM) equipped with EDS. Specific surface area (surface area normalized to mass) measurements were taken using a Micromeritics Gemini V surface and pore size analyzer. Coated YSZ powder was imaged using scanning electron microscopy (SEM) and focused ion beam (FIB)-milled using a FEI Quanta 3D field emission gun. FIB-milled samples were imaged using a Titan Themis 200 scanning TEM equipped with an energy dispersive x-ray spectroscopy (EDS) system. The thickest coatings on both zirconia

nanopowder and YSZ powder were analyzed for surface elements with x-ray photoelectron spectroscopy (XPS) using a PHI-5600LS with a monochromatic Al (1486.6 eV) x-ray source. Charge neutralization was performed on the insulating samples, and the neutralization electron current and energy was chosen to align the C 1s peak to ~284 eV. XPS peaks were fit using values from the Handbook of X-ray Photoelectron Spectroscopy (Perkin-Elmer Corporation) [96].

2.3.2 Differential thermal analysis methods

Differential thermal analysis (DTA) was performed using a Netzsch STA 449 F3 with 20 mL alumina crucibles, which was housed in an argon-purged glovebox. The furnace could not be calibrated under the test conditions of a 6% H_2 in Ar environment because melting of calibration samples or exceeding their Curie temperature would allow for undesirable metal hydride formation, which would affect the results. Experimental data were corrected for buoyancy contributions using an empty crucible to isolate phenomena from the sample. Purge gas was fed at 20 cm^3/min throughout the experiment, and the temperature was increased at a rate of 10 K/min to the furnace maximum of 1883 K where it was held for 2 hours and then ramped down at 15 K/min to room temperature.

2.3.3 Computational methods

H diffusion was investigated using DFT both from the surface into the first subsurface layer of W as well as through bulk W. The Vienna ab initio Simulation Package (VASP) was utilized to perform DFT calculations of models of the W surface and bulk structures to predict H diffusion barriers [68-72]. Plane wave periodic boundary conditions were used with the Perdew-Burke-Ernzerhof (PBE) generalized gradient approximation (GGA) exchange correlation functional and projector augmented wave (PAW) pseudopotentials [70, 73]. Calculations using a slab model of the surface were performed using a 330 eV energy cutoff and a 3×3×1 k-point expansion. A W

slab model of the surface comprised of 96 atoms was utilized to prevent lateral interactions between diffusing H atoms with their periodic images. 12 Å of vacuum space was used to prevent interactions of H on the slab surface with the bottom of the periodic image of the slab. Selective dynamics was used to perform constrained geometry optimizations and reduce the computational expense of the surface calculations. The top three atomic layers were allowed to relax during geometry optimizations while the bottom three layers of the slab were frozen at their bulk positions. The transition state for H diffusion into the first subsurface layer was determined using the dimer method. Bader charge analysis was then used to determine the charge state of the diffusing H species. Both of these methods were integrated with VASP using code developed by the Henkelman Group [97, 98].

Bulk W calculations were performed using a supercell of 64 W atoms and a 7×7×7 K-point expansion. The K-point expansion was chosen based on a convergence test (Figure 2.1) indicating constant calculated energy above 6 k-points in each direction. Diffusion pathways from nearest neighboring tetrahedral and octahedral states were investigated using the nudged elastic band (NEB) method implemented in VASP by the Henkelman group [97, 99, 100]. This method determines the minimum energy pathway between given reactants (initial state in diffusion pathway) and products (final state in the diffusion pathway) by optimizing images interpolated between the two states. The transition state is the saddle point in the minimum energy pathway determined by the NEB method.

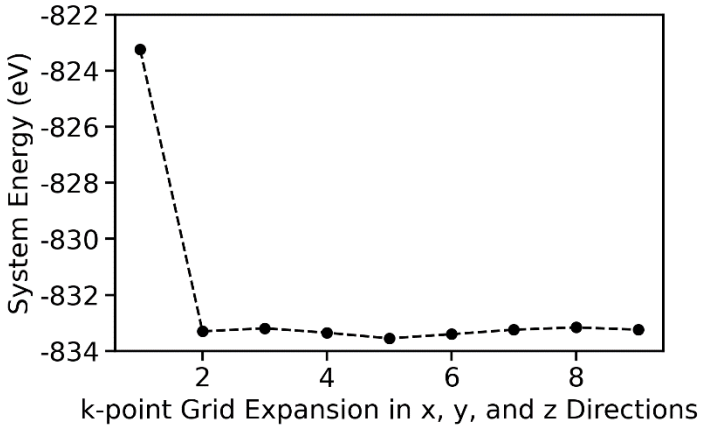

Figure 2.1 K-point convergence test showing energy versus k-point expansion in all directions for the bulk W model

2.4 **Theory/calculation**

2.4.1 Computational diffusion analysis

The approximate dependence of diffusivity on temperature is described by the equation

$$D = a^2 v \exp\left({}^{-E_a}/_{k_B T}\right) \qquad \text{Equation 2.1}$$

where E_a is the activation energy and $a^2 v$ is the pre-exponential factor, which is often referred to as simply D_0, where a is the lattice constant and v is a characteristic atomic vibrational frequency. The exponential term defines the fraction of times in which the diffusing atom will have sufficient energy to pass over the potential energy barrier, E_a. Therefore $v \exp\left({}^{-E_a}/_{k_B T}\right)$ describes the rate of successful diffusion attempts and is also known as the jump frequency. The activation energy can be calculated as the difference in energy between the transition state, E_{H+W}^{TS}, and the initial state, E_{H+W}^{0}, of the diffusing pathway. We computed this value using DFT calculations:

$$E_a = E_{H+W}^{TS} - E_{H+W}^{0} \qquad \text{Equation 2.2}$$

The pre-exponential factor,

$$D_0 = va^2 \qquad \text{Equation 2.3}$$

depends on the entropy of the system. Due to the high computational expense of phonon calculations necessary to determine the vibrational entropy contribution to the diffusion constant, D_0 was not calculated in this work. It is common to report only activation energies when comparing atomic diffusion, including diffusion through EBC materials [47].

Atomic charge states were calculated based on the quantum theory of atoms in molecules [101]. Atomic boundaries are defined where the electronic charge density is at a minimum orthogonal to the electron isodensity surface. This allows for a volume to be defined over which to integrate the charge density to calculate a total electronic charge. The difference between the calculated electronic charge and that surrounding the neutral atom of the same element is used to define an atom's charge state in this work.

2.5 Results and discussion

2.5.1 ALD growth

This work demonstrates the first deposition of WN on particles using a fluidized bed with $(^tBuN)_2(Me_2N)_2W$ and ammonia as ALD precursors. Earlier works by Becker et al. were performed on flats and colloidal crystal substrates and showed the conformal, self-limiting nature of ALD on these surfaces [53, 102]. Here we report similar results, but for nanoparticles using a fluidized bed apparatus such as that used by Hakim et al. [66, 103]. Zirconia and YSZ substrates were used as surrogates for uranium dioxide because of similarities in active surface groups for ALD and in the case of YSZ, similar thermal expansions in the temperature range tested using DTA [104-106]. Zirconia nanopowder was used for ALD chemistry characterization in order to take advantage of its high surface area and ease of imaging with an electron microscope after deposition given the thinness of the samples. Pure zirconia is also dissolved much more easily than

YSZ, which facilitates digestion for ICP analysis. In addition, reactive surface groups on zirconia are similar to those on YSZ and UO_2 making the nucleation phase of ALD – the cycles before a full monolayer has coated the surface – a good representation for oxide substrates.

Particle ALD chemistry was monitored using a MS to detect molecules in the reactor outlet, indicating when the deposition reaction is complete and the surface is saturated with precursor. Those species with the greatest partial pressures in the exhaust were chosen to be tracked during ALD. The full metal precursor is too large for detection in the MS and fractures in the ionizer. Therefore, smaller molecular weights of 45 and 71 were tracked which correspond to dimethylamino and tert-butylamino, respectively. Known gases and contaminants including water and oxygen were monitored as well to ensure that undesirable side reactions were minimized. A MS trace of a full WN ALD cycle is shown in Figure 2.2. This MS trace covers a single representative cycle of precursor dosing: 1) $(^{t}BuN)_2(Me_2N)_2W$ dose, 2) nitrogen gas purge, 3) ammonia dose, and 4) a final nitrogen gas purge. From this trace, it is evident that dimethylamino and tert-butylamino were fragments of the precursor during the metal dose as well as byproducts of the ammonia reaction during the ammonia dose. Partial pressures of precursor fragments increase with time in the MS trace; however, reaction byproducts start at their highest pressure in the MS when dosing begins and decrease with dosing time. Because ALD is self-limiting, breakthrough can be used as an indicator of a complete dosing and occurs when the surface groups on the substrate have been consumed and the precursor appears in the MS unreacted. Breakthrough is observed for the metal dose as soon as dimethylamino appears in the outlet and its signal increases above the noise. The signal increases further and then plateaus at a pressure proportional to the dosing pressure. Because the ammonia dosing pressure is large due to the high vapor pressure of the reactant, the difference in ammonia signal during surface reaction and after it has

completed is not significant enough to be used as an indicator of completed reactions. Instead, the reaction byproduct, dimethylamino, is tracked and breakthrough is indicated when the dimethylamino signal starts to decrease after peaking.

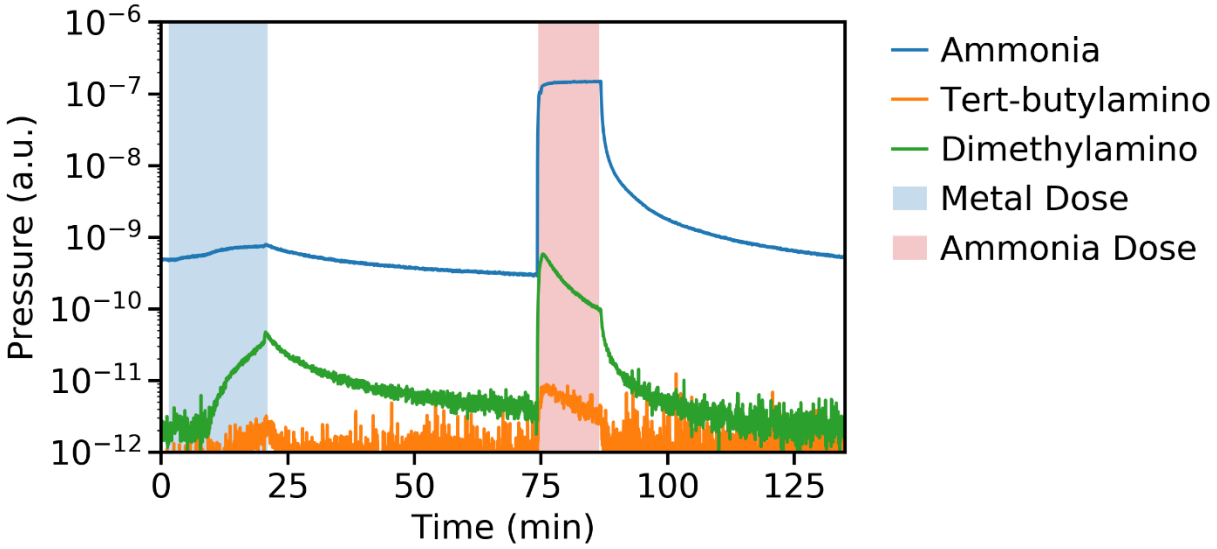

Figure 2.2 MS trace of a full WN ALD cycle. Tracked molecular weights include those of ammonia, tert-butylamino, and dimethylamino. The metal dose is highlighted in blue and the ammonia dose in red. Following the evolution of these molecules in the MS allows for the reaction progress and breakthrough to be tracked

Zirconia nanopowder was coated with either 10, 25, or 50 cycles of WN ALD. Breakthrough was seen for each cycle when the surface reaction was complete and available reactive surface groups on the substrate were consumed. The presence of deposited species is evident from the color change observed with increased cycle count shown in Figure 2.3. The number of cycles was chosen to span a range over which the nucleation of a nanofilm could be observed.

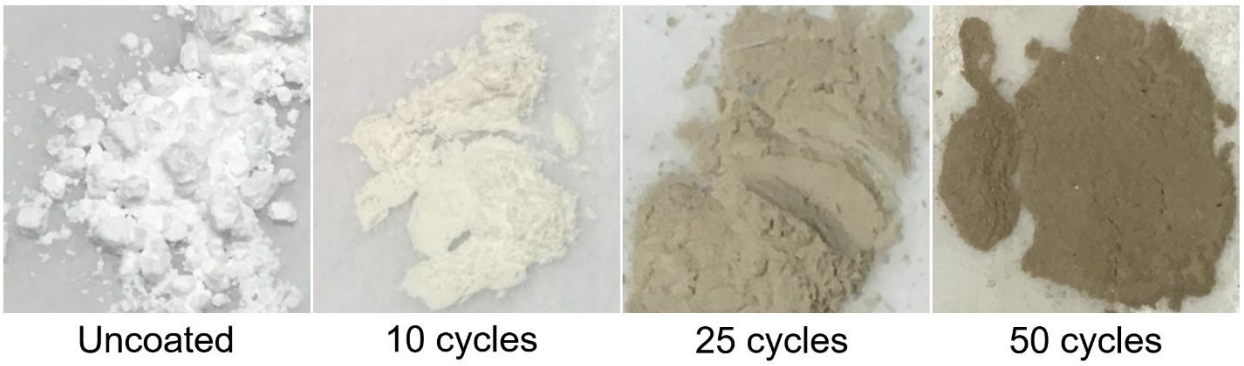

Figure 2.3 Zirconia powder after 0, 10, 25, and 50 cycles of WN ALD. These images show an increase in color intensity and decrease in particle clumping with increasing ALD cycles.

Growth rates were extracted from the ICP-OES data shown in Figure 2.4. The observed WN deposition rate on 40 nm zirconia powder of 0.17 weight % per cycle corresponds to the furnace temperature of 300ºC and dosing times of 15 and 20 minutes for the metal precursor and ammonia, respectively. Due to the low deposition rate, many cycles must be performed to reach nanometer film thicknesses. The logarithmic correlation between increased weight percent of W and number of ALD cycles performed is due to the self-limiting nature of the deposition technique on the nanopowder. Once a monolayer has been deposited, the growth rate should be constant. Below 50 ALD cycles, the ALD film is in the nucleation phase during which substrate surface groups are consumed. A logarithmic film growth curve is characteristic of this growth mode as can be seen in Figure 2.4.

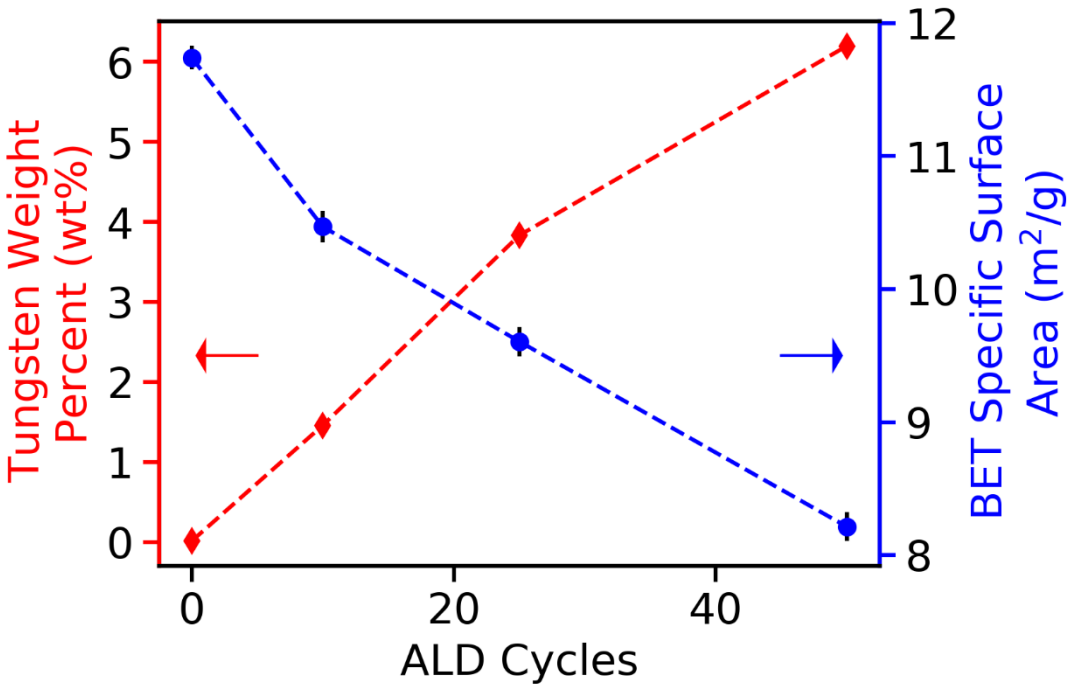

Figure 2.4 Plot of W weight percent from ICP-OES analysis (red) vs. increasing ALD cycle count on the left y-axis and BET specific surface area (blue) vs. increasing cycle count on the right y-axis. The decreasing specific surface area accompanied by increasing weight percent of W is characteristic of a growing film of higher density than its substrate and supports successful deposition of a thin film. Note that error magnitudes for ICP measurements shown here are on the order of 10^{-4} wt%.

In addition to ICP-OES, BET surface area was measured to confirm the deposition of WN on the zirconia nanopowder. The decrease in specific surface area with increased cycle count is shown in Figure 3. This is expected because the higher density of WN relative to zirconia causes the mass to increase faster than the surface area and thereby decreases the specific surface area. In addition, because particle volume is a cubic function of diameter whereas surface area only has a square dependence, the volume and its associated mass will increase faster than the surface area as diameter increases. This also contributes to a decreasing specific surface area with increasing ALD cycle count.

These films were annealed to remove nitrogen and to form crystallized W films. The difference in fixed nitrogen content of the sample coated with 50 ALD cycles before and after

annealing at either 700ºC or 725ºC is shown in Figure 2.5. The highest cycle count sample was chosen to be characterized with LECO light element analysis because it was expected to have the thickest coating and would, therefore, show the greatest contrast in nitrogen content. This data set exhibits nearly complete removal of nitrogen from the sample. It is also apparent that, at higher temperatures, more nitrogen is dissociated during the annealing step. The samples changed color from darkening shades of brown to levels of gray as seen in Figure 2.6. This is as predicted because pure W powder is dark gray. Previous studies of thin WN film annealing reported decomposition of the WN 1:1 phase into W_2N and N_2 above 550°C and stability of the W_2N phase in vacuum up to 800°C before decomposition into W and N_2 [52, 107]. The 20% H_2 environment used in this work allowed for a much lower decomposition temperature.

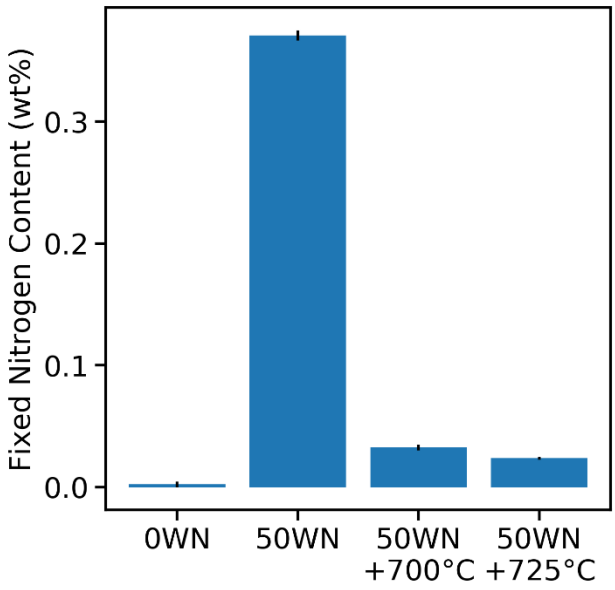

Figure 2.5 Fixed nitrogen content of samples before and after annealing in forming gas. Samples shown (left to right) include uncoated zirconia before annealing and 50 WN cycles coated zirconia before annealing and after annealing at 700ºC and 725ºC.

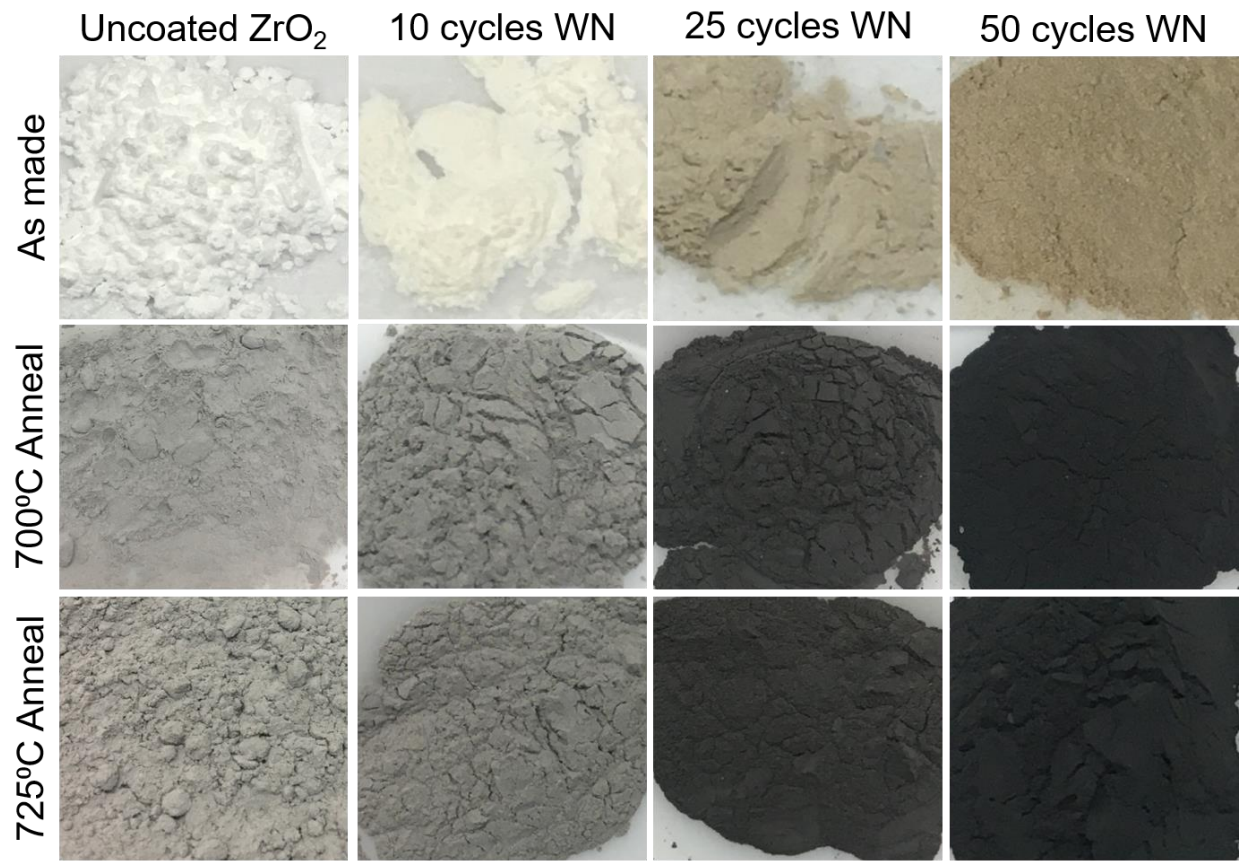

Figure 2.6 WN ALD coated zirconia powder after annealing in 20% H_2 in N_2 balance atmosphere at either 700ºC and 725ºC. The color change from brown to dark gray associated with the nitride decomposition can easily be seen.

Fixed nitrogen content for the as made 50 cycle sample also indicated that the film was not purely a 1:1 stoichiometry of WN. Based on the ICP-OES data for 50 cycles, the theoretical nitrogen content of a 1:1 W:N film is 0.47 wt%, which is 0.1% higher than observed with LECO. Although the film deposited by Becker et al. on flats was determined to have a $WN_{1.1\pm0.1}$ composition, we observed that our film must contain a mix of W oxidation states that may include WN, W_2N and/or tungsten oxide. This is a common observation in other WN deposition techniques, including reactive magnetron sputtering, which is observed to deposit mainly W_2N [108].

TEM micrographs were used to determine the film thicknesses of the coated samples. The zirconia nanopowder as received and after deposition of 25 and 50 ALD cycles of WN before annealing is shown in Figure 2.7. Islands of WN are seen on the surface of zirconia after 25 cycles. In the 50 cycle sample, island growth has continued and is observed to reach 1 nm in thickness. EDS was used on the 50 ALD sample to confirm that these islands, visible as dark spots in the TEM micrographs, were in fact due to tungsten deposition. It is necessary when depositing EBCs to determine that the film has surpassed a full monolayer in order to ensure that none of the substrate is exposed to the damaging atmosphere. Therefore, when using the chemistry on a new substrate to test film efficacy in limiting interactions between H_2 and substrate materials, greater than 50 WN ALD cycles must be performed.

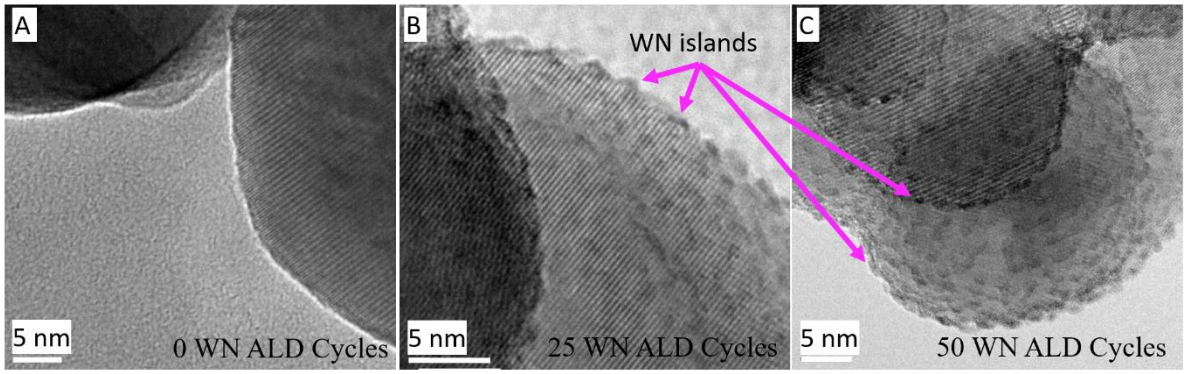

Figure 2.7 TEM micrographs of zirconia nanopowder as received (A) and coated with either 25 (B) or 50 (C) cycles of WN using ALD. Island growth can be seen in 25 and 50 ALD cycles. The presence of tungsten was confirmed using EDS on the 50 WN ALD sample.

2.5.2 WN ALD films as hydrogen EBCs

EBCs with high energy barriers (i.e., low diffusivities of H_2) can be used to protect substrates that are susceptible to H_2 embrittlement. WN was deposited on YSZ powder via ALD and tested under hot H_2 flow to examine the inhibition of H_2 reaction with the substrate. Below its decomposition temperature, WN will serve as the protective barrier. After decomposition, a pure W coating will remain to protect the substrate. It is expected that the nitrogen will assist in

preventing hydrogen diffusion through increased steric hindrance. YSZ was chosen for testing the WN/W film as an EBC as opposed to pure zirconia, which was used for characterizing the chemistry, to avoid the monoclinic to tetragonal phase transition of pure zirconia at 1170ºC during testing. 5% YSZ is partially stabilized and therefore serves as a better surrogate for UO_2 during thermal testing. YSZ has the same active hydroxyl surface groups for ALD as UO_2 as well as similar thermal expansion coefficients over the temperature range of interest.[104-106] This is necessary because phase changes and their associated density and volume changes have the potential to crack thin films.

Two coated samples were made using 65 and 100 cycles of WN ALD to elucidate the effect of thickness on substrate protection. From the deposition rate extracted from zirconia nanopowder studies, these cycle counts correlate to approximately 1.3 and 2 nm, respectively. We hypothesized that because W has a high energy barrier for atomic H diffusion, an ~1 nm thick coating would be sufficient. However, the energy barrier for H diffusion in W becomes less significant as temperature increases Equation 2.1. Therefore, the magnitude of film thickness required to prevent H diffusion up to 1610ºC was probed. XPS was used to characterize the 100 ALD cycle film on the YSZ microspheres and to compare it to the thickest zirconia nanopowder sample with 50 ALD cycles. The XPS spectra confirm the presence of tungsten and nitrogen on both substrates and are shown in Figure 2.8. The spectra shapes are very similar, although higher intensities for tungsten and nitrogen are observed for the thicker WN coating on YSZ than is seen on zirconia. Conversely, lower intensities are seen for the zirconium peaks in the YSZ sample. This is due to the additional ALD cycles performed on the YSZ microspheres to give a coating twice as thick and with higher surface coverage than that on the zirconia nanopowder. In fact, this thicker coating has clearly suppressed the zirconia signals. Adventitious oxygen and carbon are present on the surface of these

samples due to exposure to atmosphere. Yttrium is not seen in the YSZ spectrum due to film coverage.

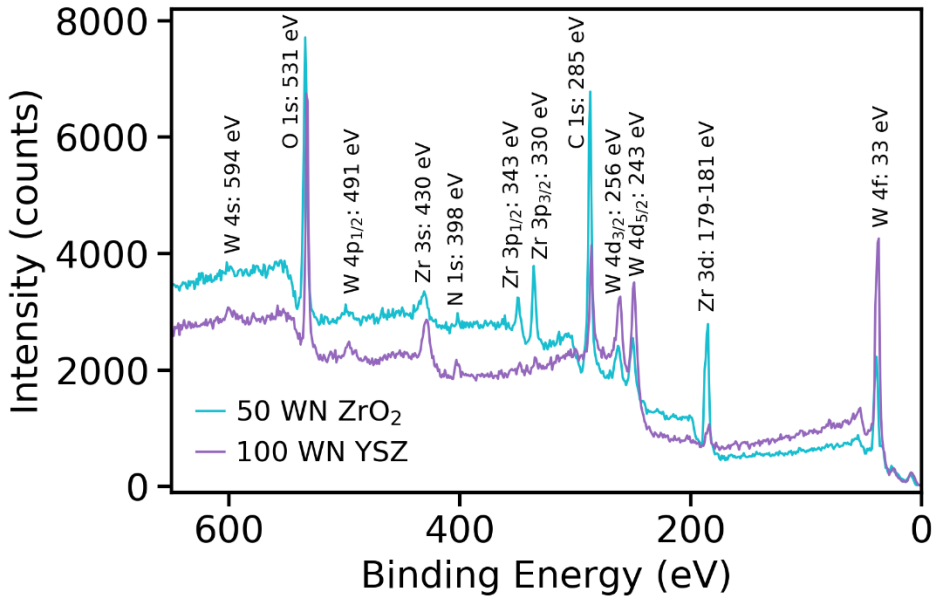

Figure 2.8 XPS spectra of the thickest coatings on the two substrates tested in this work. Samples included 50 WN ALD cycles on zirconia nanopowder and 100 WN ALD cycles on YSZ microspheres. Values next to peak labels correspond to the energy value from the database detailed in methods. Although the spectra are similar in shape, the peak heights vary according to film thickness and surface coverage. As predicted, the thicker ALD film on the microspheres show larger W and N peaks, but smaller zirconium peaks than the thinner 50 cycle film.

Microscopy was used to determine whether the deposited film had fully coated the YSZ microspheres. The SEM micrographs of the coating are shown in Figure 2.9. The increase in brightness of the particles from uncoated to coated conveys a change in interaction of the particles with the electron beam. This is attributed to the higher atomic number of the tungsten-based film on the coated surface. In addition, the surface charging seen as striations in the micrograph of the uncoated sample is not present in the coated sample. This conveys the transition from an electrically insulating surface to a conducting film. In addition to SEM, the 100-cycle sample was FIB-milled and imaged using TEM+EDS (Figure 2.10). EDS confirmed the presence of W in the coating and ICP-MS was used to determine a weight loading of 0.02 wt% W. TEM+EDS could

not, however, be used to measure the film thickness because the thin film was likely perturbed during the milling process.

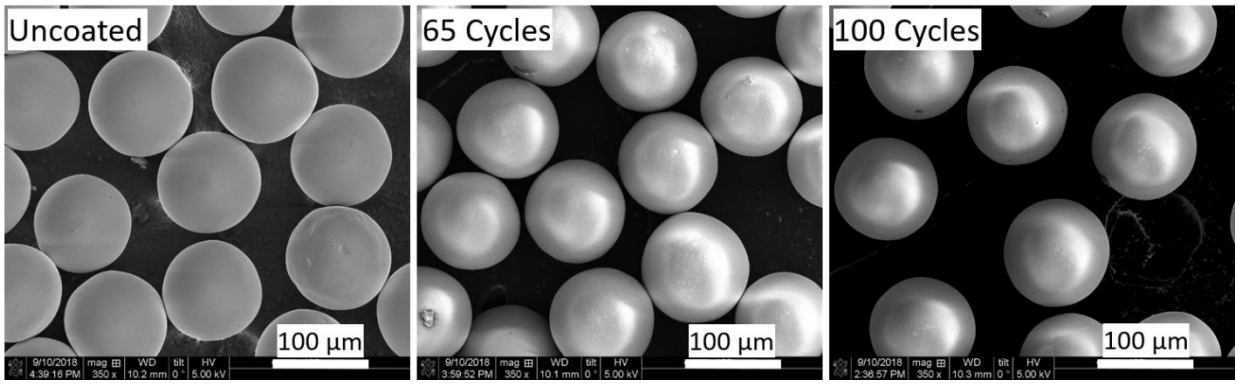

Figure 2.9 SEM micrographs of uncoated, 65 cycles, and 100 cycles of WN on 100 micrometer diameter YSZ powder. The increase in brightness of the particles from uncoated to coated indicates deposition of the WN film.

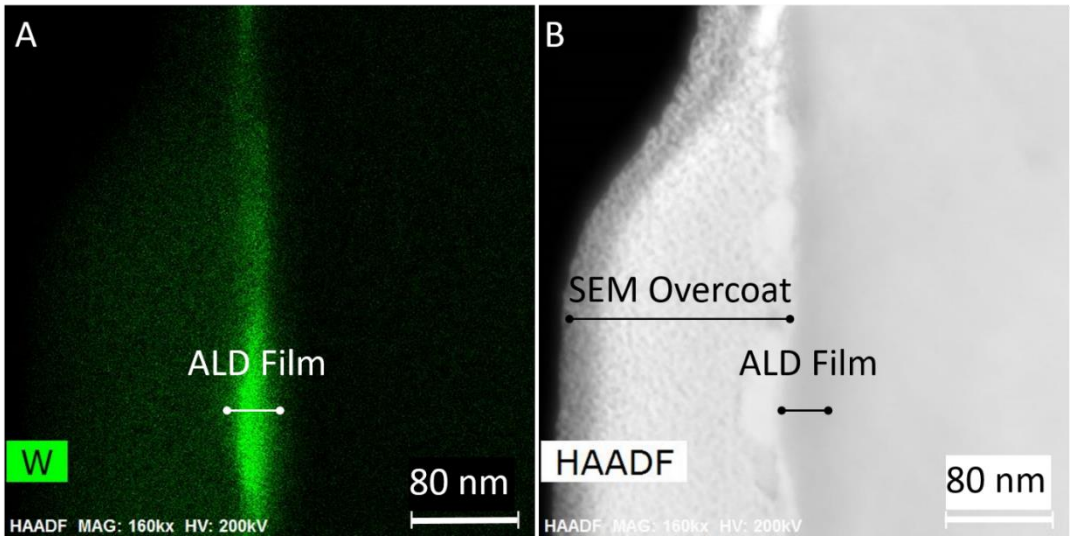

Figure 2.10 W EDS map (A) and dark field micrograph (B) of 100 WN ALD cycles on YSZ micropowder. Imaged cross-section was prepared using FIB-milling.

The three YSZ samples: uncoated, 65, and 100 cycles were tested using DTA. The overlaid DTA curves with exothermic peaks oriented downward are shown in Figure 2.11. These curves were produced using a 20 sccm flow of 6% H_2 in Ar environment. The 100 cycle WN sample was also characterized in pure Ar in order to isolate those curves that are dependent on the presence of H_2. Three noteworthy observations can be made. First, the exothermic peaks highlighted in pink

and blue appear only when testing the coated sample, indicating that the peaks are due to the ALD coating. The pink highlighted peaks indicate partial WN decomposition to form crystallized W2N from WN. The curve minimums on these peaks correspond to temperatures between 550ºC and 580ºC which indicates that, to crystallize WN without removing nitrogen, annealing must occur below 500ºC. These results agree well with the temperatures reported by Samsonow et al. for W2N formation from higher nitrogen stoichiometries above 550ºC [107]. In addition, this decomposition temperature supports the results observed from annealing the coated zirconia powder in forming gas where decomposition was observed below 700ºC. The peak highlighted in blue corresponds to a final nitride decomposition to form cubic W, likely from W_2N. This claim is based on the observation of Becker et al. of formation of crystalline W above 725°C from a thick WN ALD film [53]. These decomposition peaks convey that although a WN film was deposited, as temperature increases the film is converted from a nitride to a metallic coating. Therefore, above ~900°C, pure tungsten serves as the EBC.

The peak highlighted in green only appears when H_2 is present. The exothermic characteristic of this peak indicates the presence of a reaction between the substrate and H2. The reaction temperature is higher for samples with larger numbers of ALD cycles. The correlation between the increase in temperature and the thickness of the W/WN film suggests that the film delayed the H2 reaction with the substrate. This is a result of the lower diffusivity of H in W and WN relative to its diffusivity in the YSZ substrate. The W/WN film reduces the fraction of H atoms that reach the substrate to react. The existence of the H_2 reaction peak, even in the thicker film, indicates that H diffusivity is greater in the temperature range tested than is accounted for in these film thicknesses. Thicker ALD films will be required to increase the temperature at which

reaction between H and the substrate occurs beyond the maximum temperature of 1610ºC probed in this study.

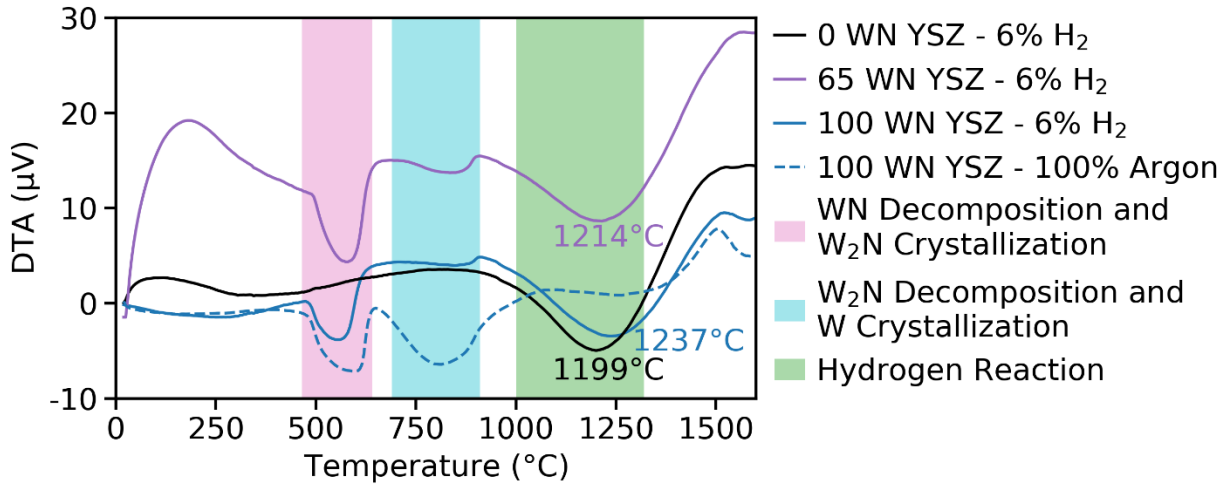

Figure 2.11 Differential thermal analysis curves for YSZ 100-micron sized powder coated with either 0, 65, or 100 ALD cycles of WN. The testing environment either contained 6% H2 in Ar or pure Ar as noted in the legend. Exothermic peaks are shown here in the downward direction. The pink and blue highlighted negative peaks are caused by decomposition of the film into W2N and W, respectively. The green highlighted negative peaks are due to reaction of the substrate with H2 and their labeled temperatures indicate the temperature at which the peaks are at their minimum µV.

2.5.3 **Computational hydrogen diffusion analysis**

The film's intended use as an EBC was motivated by the observed low atomic H diffusivity in W compared to other refractory metals. In addition to thermal analysis of the ALD films, H diffusion into perfect crystal (i.e. no defects) surfaces and through bulk W was investigated using DFT. Atomic H was analyzed because geometry optimizations of adsorbed H_2 molecules relaxed to a state of two adsorbed H atoms, predicting the spontaneous dissociation of H_2 upon adsorption. In addition, geometry optimizations of absorbed H_2 within bulk W led to its dissociation into hydrogen species that form hydrides with the surrounding W lattice atoms. The (110) W surface was determined to be the most energetically favorable and therefore most probable surface of the ALD film after an anneal in forming gas. Of the unique adsorption sites on this surface, including

the bridge, hollow, and atop sites, the hollow site was predicted to be the most energetically favorable. Adsorption at this site causes only a slight movement of the nearest neighbor W atoms of less than 0.02 Å.

To analyze H diffusion into the W film, the lowest energy position of H in the W subsurface was determined by relaxing subsurface H configurations. From the hollow adatom site, an energy barrier of 2.0 eV was calculated for diffusion into the first subsurface layer. The diffusion pathway is shown in Figure 2.12. In comparison to other pure transition metals, this is a relatively large energy barrier [47]. The H charge state was calculated at the adsorbed state, transition state, and subsurface sites on the diffusion pathway and computed to be -0.42 e, -0.44 e, and -0.47 e, respectively. This negative charge state indicates that the interstitial H species gained electrons and formed hydrides with the W atoms and that the charge on the diffusing H atom is nearly constant as it diffuses into the subsurface.

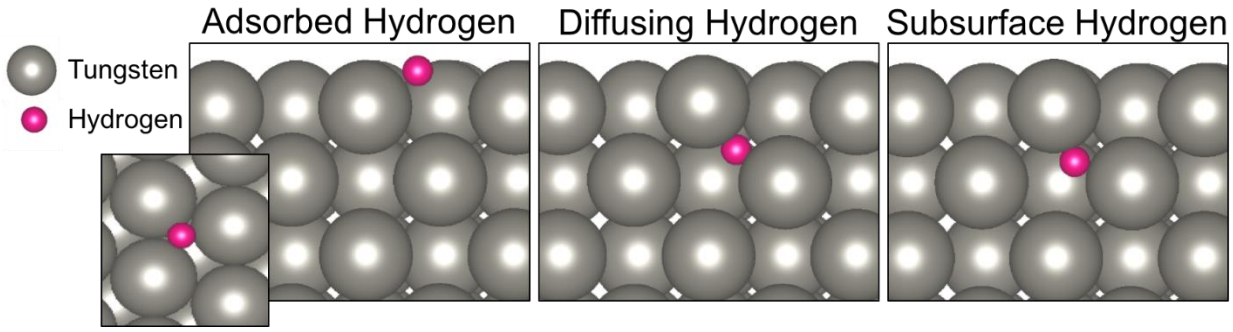

Figure 2.12 Stages of hydrogen surface absorption showing adatom site, transition state, and final subsurface site as well as the charge associated with the diffusing hydrogen.

Atomic H diffusion in bulk W was also investigated. Tetrahedral interstitial positions were found to be more favorable than octahedral positions by 0.35 eV which is slightly higher in energy than that predicted by Heinola et al. and Kong et al..[41, 109] In addition, hopping from one tetrahedral site to another provides the lowest diffusion energy barrier of 0.19 eV. H charge states were also calculated for bulk diffusion and found to be -0.48 e for tetrahedral sites, -0.24 e for

octahedral sites and -0.49 e for the transition state between two tetrahedral sites. The smaller charge state of H when it resides in octahedral interstitial sites compared to tetrahedral interstitial sites indicates that less electron density is transferred to the H atom from the surrounding W atoms. This decrease in charge localized on interstitial H may contribute to the lower stability of H in octahedral versus tetrahedral interstitial sites.

Future work will analyze the computed energy barriers of refractory materials with varying charge states of the diffusing H interstitial to elucidate a connection between these properties. The results for W reported here suggest that EBC materials that do not allow for the transfer of significant electron density from the metal lattice atoms to the diffusing H atom, as predicted for W, may result in a higher diffusion energy barrier. It is evident from our DFT calculations and DTA studies that a more effective EBC material than W is required for success of a thin film barrier at temperatures above 1000^{o}C because even at moderate temperatures the thin W film still allowed for some H to diffuse through and react with the YSZ substrate. Computational analysis can help to predict a better barrier material by screening refractory materials for energy barriers larger than that of W (2.0 eV for absorption and 0.19 eV for bulk diffusion).

2.6 **Conclusions**

This work probed WN ALD films on particles deposited using $(^{t}BuN)_2(Me_2N)_2W$ and ammonia as precursors, and the efficacy of the deposited films as hydrogen EBCs. WN was successfully deposited on zirconia nanopowders using a fluidized bed reactor. 10, 25, and 50 ALD cycles were performed to deposit films of three different thicknesses. The growth rate of this chemistry on nanoparticles was determined to be 0.2 Å/cycle based on TEM images. The transition from islands to a full monolayer occurs above 50 WN ALD cycles. After deposition, annealing conditions were probed to decompose the nitride and form a crystallized W coating.

The efficacy of the nanofilm as a hydrogen EBC was characterized using DTA. The peak reaction temperature between H_2 and the substrate increased with increasing film thickness. DTA also identified the WN decomposition temperature which peaked at 576ºC in an inert atmosphere. Nonetheless, reaction of H_2 with the substrate still occurred with the thickest film, indicating that additional ALD cycles are required to significantly reduce the interaction of H_2 with the substrate, or, a more effective barrier material should be selected.

DFT calculations were used to analyze atomic H diffusion into a W surface representative of that deposited by ALD. An energy barrier for diffusion into the first subsurface layer was found to be 2.0 eV, which is larger than for most transition metals. In addition, the charge state associated with the diffusing H was calculated to be negative and, therefore, indicates that hydrides are formed between the W atoms and the H atom. The magnitude of this charge state is smaller for H residing in octahedral interstitial sites than in tetrahedral sites, which could contribute to the lowered stability of H in octahedral sites. The calculated diffusion energy barrier in W should serve as an indicator of a lower bound for screening candidate barrier materials computationally.

2.7 Acknowledgments

Funding: This work was supported by NASA ESI grant number 80NSSC18K0254. DFT calculations were performed on the RMACC Summit supercomputer, which is supported by the National Science Foundation (awards ACI-1532235 and ACI-1532236), the University of Colorado Boulder, and Colorado State University. The Summit supercomputer is a joint effort of the University of Colorado Boulder and Colorado State University. This research made use of the resources of the High-Performance Computing Center at Idaho National Laboratory, which is supported by the Office of Nuclear Energy of the U.S. Department of Energy and the Nuclear Science User Facilities under Contract No. DE-AC07-05ID14517. The authors would also like to

acknowledge Fredrick Luiszer for ICP-OES analysis and Alexander Harris for inert handling of the ALD precursor.

Chapter 3

Ab initio Screening of Refractory Nitrides for High Temperature Hydrogen Permeation Barriers

Most of the content in this chapter appears verbatim in the following manuscript:

Sarah K. Bull, Theodore Champ, Sai Raj, Alan W. Weimer*, and Charles B. Musgrave*. Ab initio Screening of Refractory Nitrides for High Temperature Hydrogen Permeation Barriers. (2021) [In preparation]

3.1 Abstract

Density functional theory was used to screen 11 refractory materials including 2 pure metals, 6 nitrides, and 3 carbides as high temperature hydrogen permeation barriers to prevent hydrogen embrittlement. Activation energies were calculated for atomic hydrogen (H) diffusion into the first subsurface layer from the lowest energy surface of the high-temperature phase of each candidate material. The candidate barrier materials with the highest activation energies are *h*-BN, *c*-BN, HfN, and ZrN with predicted barriers of 3.3 eV, 3.2 eV, 3.2 eV, and 2.7 eV, respectively. Strain energies, Bader charges and density of states were calculated for the diffusing H at the relaxed initial and transition states to provide insight into contributing factors to high energy barriers. The diffusing H atom in materials with the highest predicted barriers are protic. In addition, interstitial H atoms induce mid-gap states in the density of states of both BN polymorphs. The nitrogen retention of each nitride material at high temperatures was predicted using nitrogen vacancy formation energies with respect to gaseous nitrogen and ammonia formation. Nitrogen retention was evaluated experimentally for *h*-BN, ZrN, and TiN and confirmed their resistance to N at 1773 K. However, at 2550 K, TiN is predicted to lose its fixed N content due to formation of gaseous nitrogen. This work identifies multiple promising materials that are predicted to be

effective hydrogen barriers at high temperatures and are stable at temperatures above 2700 K with BN predicted to perform best.

3.2 Introduction

From the hydrogen economy [1, 2] to nuclear reactors [4] and ammonia synthesis, hydrogen is an essential component of the energy industry. It has also been proposed as the propellant of nuclear thermal propulsion (NTP) engines for interplanetary travel [5]. However, its appealing properties as a fuel and propellant are moderated by the phenomena of hydrogen-induced damage. The low molecular weight of hydrogen, which makes it such an attractive element for storing energy and for use as a high specific impulse propellant in a NTP engine, also allows it to easily diffuse through most materials – to either embrittle or react with them [35]. Molecular hydrogen (H_2) often dissociates exothermically on metallic surfaces [110], producing atomic H that then diffuses into the bulk material and often causes H embrittlement. In metals, H embrittlement leads to higher ductile to brittle transition temperatures [7, 111], the formation of metal hydrides [111], gaseous hydrogen bubbles [22, 23], and lower adhesive strength at grain boundaries through surface stabilization [7, 24, 111]. Similar phenomena appear in ceramic materials as well including the uranium-based nuclear fuel elements in NTP engines [10, 21].

Environmental barrier coatings (EBCs)[1], sometimes referred to as permeation barriers, can combat hydrogen embrittlement from extrinsic H sources. Previously studied barrier materials include pure metals, graphite, carbides, nitrides, and oxides. The most common hydrogen permeation barrier is alumina because it has a low H diffusivity and can be grown directly on the substrate via aluminizing and oxidation [12, 31, 35, 36]. Other materials listed have been deposited

[1] It is important to note that "EBC" as used in this paper specifically refers to coatings that act as hydrogen permeation barriers to avoid confusion from its traditional use in the ceramics literature as moisture-resistant protective coatings for SiC-based ceramic matrix composites.

via atomic layer deposition (ALD) [37], chemical vapor deposition (CVD) [31, 38], magnetically enhanced plasma ion plating [39], and packed-bed cementing [31]. The choice of an EBC composition resistant to hydrogen permeation is governed by low hydrogen permeability materials, its chemical compatibility with the substrate, and the closeness of its coefficient of thermal expansion with that of the substrate. Specifically, for a NTP engine application, it is essential that the EBC possess a low neutron scattering cross section. The choice of the coating deposition method is influenced by the coating composition and coating thickness as well as the geometry and composition of the substrate. These factors are likely to influence the EBC microstructure and resulting H permeability [59, 60, 112].

At temperatures below 1640 K [113], alumina is the most common choice of EBC due to its relative ease of formation and efficacy as an EBC [35, 114]. However, at the ultrahigh temperatures >2700 K corresponding to the operating temperature of NTP engines, the number of viable EBC materials available is reduced to those that are thermally stable and that have sufficiently high diffusion barriers to still impede H permeation at these temperatures. The greater thermal energy available at high temperatures requires that the activation energies for H diffusion be large for a successful EBC. For instance, while a diffusion barrier of just over 1 eV would be sufficient at room temperature, a barrier of ~9 eV would be required at 2,700 K to effectively reduce H diffusion. At 2700 K, tungsten (W) is the preferred metal due to its high melting point, strength, thermal conductivity and low H diffusivity compared to other pure metals [44, 47, 115, 116] although it is noted that most of its isotopes have a large neutron scattering cross-section [117]. The H diffusion in and potential embrittlement of pure metals, including W [24, 42, 109, 118-120] and molybdenum (Mo) [45, 120-122], have been extensively characterized

computationally and experimentally. However, fewer studies have examined H diffusion in high melting point nitrides and carbides [31, 59, 60, 90, 123, 124].

In this work, we use density functional theory (DFT) to analyze atomic hydrogen diffusion in refractory nitrides and carbides with melting points greater than 2700 K and compare their computed activation energies to those of Mo and W. Additionally, we analyzed contributions to the diffusion barrier, E_a, from steric hindrance and the redistribution of electron density during the H hopping event. Retention of fixed nitrogen content of the nitrides was predicted through calculation of nitrogen vacancy formation energies referenced against the formation of gaseous nitrogen (N_2) and ammonia (NH_3). This was compared to the experimentally determined N retention for commercially available powders. Our results from *ab initio* calculations and nitrogen retention experiments suggest that BN, HfN, and ZrN are likely to outperform the pure metals (W, Mo) currently used as NTP EBC's with respect to H diffusivity.

3.3 Materials and methods

3.3.1 Computational methods

All DFT calculations including slab and bulk model systems were performed using the Vienna ab initio Simulation Package (VASP) [68-72] with the strongly constrained and appropriately normed semi-local density functional (SCAN) [125], projector augmented-wave (PAW) pseudopotentials [70, 126] and a 520 eV energy cutoff. Surface calculations of the low Miller index surfaces were performed using a slab model of the surface and a 5×5×1 k-point expansion. The plane wave cutoff energy (Figure 3.1) and k-point expansion (Figure 3.2) were chosen to satisfy convergence requirements following a test of the convergence of the smallest slab used in this work, *c*-BN.

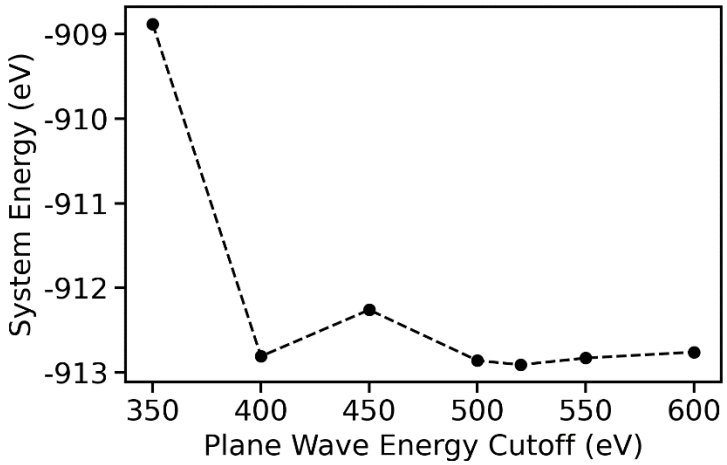

Figure 3.1 Total system energy versus plane wave energy cutoff for *c*-BN slab indicating minimum required 500 eV cutoff for cell size

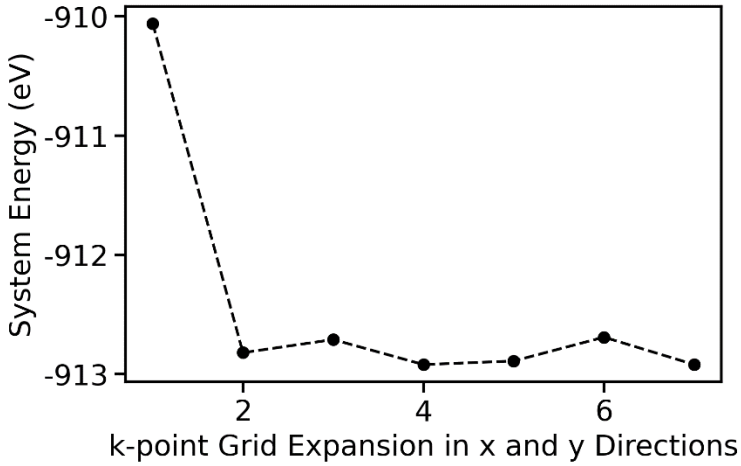

Figure 3.2 Total system energy versus k-point expansion in x and y directions for *c*-BN slab indicating a minimum of 4 k-points required

The initial crystal structures were taken as the lowest energy configuration for the specified stoichiometry from The Materials Project data base [127]. The lowest energy surface, and therefore most probable surface of each material, was determined by comparing the computed surface energies of the low Miller index surfaces and used in the slab model to simulate H diffusion. Supercells were created to serve as slab models of the surface with lattice parameters chosen to limit lateral interactions between diffusing H atoms with their periodic images. H adatoms were separated from their lateral periodic images by over 7 Å, and ~12 Å of vacuum space was used to

prevent interactions of adsorbed H on the slab surface with the bottom of the periodic image of the slab. This slab geometry was used in all subsequent H diffusion analyses. Atomic H adsorption energies were calculated for all unique adsorption sites on each material's lowest energy surface. Then, H diffusion barriers starting from only the most probable site on the lowest energy structure were computed and analyzed.

Constrained geometry optimizations were performed to reduce the computational expense of calculating structures where only the top three atomic layers of the slab were allowed to relax while all other layers were frozen at their bulk lattice positions. Transition states for H atom hopping were determined using the nudged elastic band (NEB) method [100, 128, 129] followed by the dimer method [97, 99, 130, 131] starting from the structure of the highest energy NEB image. These methods search the potential energy surface to determine the minimum energy pathway between two points (i.e. initial and final states of H hop) and converge the highest energy position to the saddle point (i.e. transition state) along this pathway. Bader charge analysis [98, 101, 132-134] was performed to determine the charge state of the diffusing H species.

The density of states (DOS) of the initial and transition states along the H diffusion pathway were computed using a 10×10×1 k-point mesh, except for ZrN, whose DOS was computed using a 5×5×1 mesh to avoid convergence issues. The computational cost of an increased k-point mesh for ZrN with semicore states included in the Zr pseudopotential exceeded the available resources. Strain energies were calculated as the difference in energy between the lattice atoms frozen at the initial and transition states of a single H hop and the relaxed slab using a 5×5×1 k-point mesh.

Nitrogen vacancy formation energies were calculated using a bulk model. Bulk calculations were performed using supercells (Table 3.1) to prevent interactions between H with its periodic images and used a 6×6×6 k-point expansion. This k-point expansion was chosen

following a convergence test (Figure 3.3) of a 48-atom TaN cell which represented the minimum expansion because all utilized supercells were larger (Table 3.1). The nitrogen (N_2) and ammonia (NH_3) reference states were calculated as an isolated diatomic N_2 molecule or single NH_3 molecule, respectively, modeled in an otherwise empty 10 Å × 10 Å × 10 Å cell. Chemical potentials were calculated at 1773 K and 2773 K using the gaseous N_2 and NH_3 reference states.

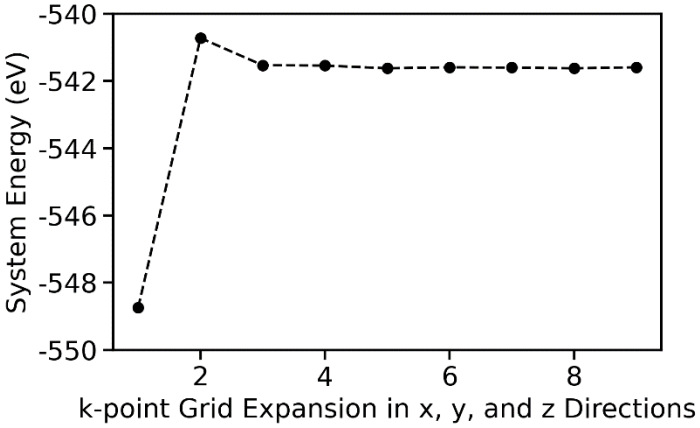

Figure 3.3 K-point convergence test (energy vs expansion) of a 48-atom TaN cell showing minimum of 5 k-points required in each direction

Material	Atoms	a (Å)	b (Å)	c (Å)
***c*-BN**	54	7.7	7.7	7.7
***h*-BN**	72	7.5	7.5	15.4
ZrN	64	9.0	9.0	9.0
TaN	72	10.4	10.4	8.7
TiN	64	8.5	8.5	8.5
HfN	64	9.2	9.2	9.2

Table 3.1 Supercell size for bulk material calculations

3.3.2 Experimental methods

Bulk powder samples of *h*-BN (HCV grade; 95% -325 mesh, Advanced Ceramics Corporation), TiN (99.7%, metals basis; <10 μm, Sigma Aldrich), and ZrN (99.5%, metals basis excluding Hf; -325 mesh powder, Alfa Aesar) were tested under hot H_2 flow for nitrogen retention. Samples were heated to 1773 K from room temperature at 10 K/min and held at the maximum temperature for 3 hours, after which they were allowed to return to room temperature at a

maximum cooling rate of 10 K/min. Temperature ramps were performed in a 40 cm^3/min flow of Ar. At the 1773 K hold, H_2 was introduced and maintained at a flow rate of 10 cm^3/min in addition to the 40 cm^3/min of Ar.

3.4 Theory/calculation

3.4.1 Computational diffusion analysis

The dependence of diffusivity on temperature is described by:

$$D = D_0 exp\left(\frac{-E_a}{k_B T}\right) \quad \text{Equation 3.1}$$

where D_0 is the pre-exponential factor, E_a is the activation energy for an atomic hop, k_B is the Boltzmann constant, and T is the absolute diffusion temperature. The pre-exponential factor D_0 is a product of the lattice constant a, the attempt frequency v, and a constant that corresponds with the number of available hop destination sites [135]:

$$D_0 = \alpha a^2 v. \quad \text{Equation 3.2}$$

The exponential term in Equation 3.1 describes the probability of overcoming the activation energy barrier, E_a. We used DFT in this work to calculate E_a as the energy difference between the transition state, E_H^{TS}, and the initial state, E_H^0, along the minimum energy pathway for an atomic hop:

$$E_a = E_H^{TS} - E_H^0. \quad \text{Equation 3.3}$$

The pre-exponential factor, D_0, was not calculated due to its high computational expense coupled with the large number of materials screened. Instead, only E_a's were compared to evaluate the material efficacy as an EBC. An examination of Equation 3.1 and Equation 3.2 suggests that the diffusion constant, D, is more sensitive to differences in E_a than differences in D_0 due to the exponential factor. A general need exists for D, D_0, and E_a included in the diffusivity equation (Equation 3.1) for refractory carbides and nitrides. However, of the materials evaluated in this

work, D_0 for H and deuterium diffusion has been reported for W and *h*-BN and are of similar magnitude of 10^{-7} to 10^{-8} [43, 60, 109, 136-138]. Experimentally determined values of D_0 for H diffusion in Mo have been reported between 10^{-4} and 10^{-8}, although it has been calculated by DFT to be on the order of 10^{-8} [139]. Reports of the computed values of D_0 for H diffusion in bulk ZrC and bulk NbC are on the order of 10^{-4} [140] and 10^{-6} [141], respectively. Despite the factor of ~100 difference for D_0 of carbide materials, a moderate difference in E_a of 1.1 eV can overcome this difference in D_0 at 2700 K. Because of the sensitivity of D to E_a due to the exponential, in addition to the computational cost of computing phonon frequencies to calculate D_0, it is common to report only E_a when comparing permeabilities of similar materials [47, 142, 143]. The similarities in composition and crystallinity of evaluated materials further supports analyzing and comparing E_a in this work.

Atomic charge states were calculated for the diffusing H atom as the difference between the electron charge associated with the atom as calculated using Bader charge analysis and the charge of the nucleus of that atom.

3.4.2 Strain energy of diffusion

As an interstitial H diffuses through a material, it forces atoms off their relaxed lattice positions as it passes through the transition state. The increase in the energy of the system due to this strain is referred to here as strain energy (E_ε) and its contribution to the energy barrier for H diffusion was computed as follows:

$$E_\varepsilon = E^{Slab-H} - E^0 \qquad \text{Equation 3.4}$$

Where $E^{Slab\text{-}H}$ is the energy of the slab fixed at the initial, transition, or final state positions with the diffusing H atom removed and E^0 is the energy of the relaxed surface before exposure to H.

3.4.3 High temperature stability of screened refractory nitrides

In order to take advantage of the high melting points and E_a's of nitrides over pure metals and metalloids, the retention of fixed N at elevated temperatures is required. These nitrides are reduced by evolving N at temperatures below their melting points through nitrogen vacancy formation accompanied by the loss of gaseous nitrogen (N_2) or gaseous ammonia (NH_3) in a H-environment. The N vacancy formation energy relative to N_2 (E_{vf,N_2}) of a single N vacancy in the supercell was calculated:

$$E_{vf,N_2} = E_{v,bulk} - E_{bulk} + \frac{1}{2}E_{N_2} \qquad \text{Equation 3.5}$$

where $E_{v,bulk}$ is the energy of the system with a N vacancy, and E_{bulk} the energy of the defect-free system, and E_{N_2} the energy of N_2 in vacuum adjusted for changes in chemical potential (μ) at finite temperatures. Similarly, the N vacancy formation energy relative to forming NH_3, E_{vf,NH_3}, was calculated:

$$E_{vf,NH_3} = E_{v,bulk} - E_{bulk} + E_{NH_3} - \frac{3}{2}E_{H_2} \qquad \text{Equation 3.6}$$

where again $E_{v,bulk}$ is the energy of the system with a N vacancy and E_{bulk} the energy of the defect-free system. The terms E_{NH_3} and E_{H_2} are the energies of NH_3 and H_2, respectively, in vacuum adjusted for changes in chemical potential, μ, at finite temperatures.

The chemical potential at temperature *T* is calculated as [144]:

$$\Delta\mu(T, P_0) = \left[H_0 + C_p(T - T_0)\right] - T\left[S_0 + C_p \ln\left({}^{T}/_{T_0}\right)\right] \qquad \text{Equation 3.7}$$

Where P_0, T_0, H_0, and S_0, are the reference pressure, temperature, enthalpy, and entropy, respectively, and C_p the heat capacity. Tabulated values were used for the standard diatomic N_2 gas reference, NH_3 gas reference and H_2 gas reference [145]. A larger vacancy formation energy suggests a more thermodynamically stable material relative to N_2 or NH_3 formation.

3.5 Results and discussion

3.5.1 Screened materials

The need for H permeation barriers at temperatures above 2700 K motivated the screening of refractory nitrides and carbides to evaluate their viability relative to the most common pure metals for these applications, W and Mo. The screened materials were selected because their melting points exceed 2700 K, the operating temperature of a NTP engine. The materials screened are Mo, W, *c*-BN, *h*-BN, HfN, TaN, TiN, ZrN, NbC, WC, and ZrC. In order to predict the performance of candidate materials as H diffusion barriers that effectively limit H ingress, E_a for atomic H diffusion into the lowest energy surface from the most favorable absorption site on that surface was calculated and compared to the computed values of E_a for legacy materials W and Mo. Initial bulk structures were chosen as the lowest energy structure of the specified stoichiometry using tabulated formation enthalpies in The Materials Project [127]. The computational details, slab dimensions, space group, lowest DFT-calculated energy surface plane, and most favorable adsorption site are shown for each screened material in Table 3.2. The favorability of the three-fold coordinated site (hollow site) on the pure metals matches previous DFT findings [47] as well as the top of B site for *h*-BN [146] top of N site for *c*-BN [147] top of transition metal site for cubic metal nitrides [148, 149], and top of C site for cubic metal carbides [150]. However, previous studies for H adsorption on the hexagonal TaN (110) and WC (100) surfaces are not available for comparison.

Material	**Atoms/ unit cell**	**a**	**b**	**c**	**Space Group**	**Lowest Energy Surface**	**Most Favorable Adsorption Site**
Mo	45	8.2	8.2	24.5	Im3m – BCC	(110)	Hollow
W	45	8.2	8.2	24.5	Im3m – BCC	(110)	Hollow

c-BN	96	7.7	7.2	23.0	F43m – FCC	(110)	N
h-BN	72	7.5	7.5	26.8	P63/mmc – Hex.	(001)	B
HfN	108	9.5	9.5	27.0	Fm3m – FCC	(100)	Hf
TaN	72	8.7	9.0	23.8	P62m – Hex.	(110)	Hollow
TiN	108	9.0	9.0	25.4	Fm3m – FCC	(100)	Ti
ZrN	108	9.7	9.7	27.5	Fm3m – FCC	(100)	Zr
NbC	108	9.4	9.4	26.6	Fm3m – FCC	(100)	C
WC	96	11.6	8.5	22.6	P6m2 – Hex.	(100)	Bridge
ZrC	108	10.0	10.0	28.2	Fm3m – FCC	(100)	C

Table 3.2 Screened materials and computational details including atoms in a unit cell for the surface slab, slab dimensions (Å), material space groups, most favorable (lowest energy) surface and adsorption site

3.5.2 Diffusion barrier energies of screened materials

Higher values of E_a indicate lower probabilities of overcoming the diffusion barrier energy for atomic hopping and consequently, lower diffusivities (Equation 3.1) Therefore, materials with a larger E_a than W, the current state-of-the-art H barrier material for high temperature applications [31, 115], are predicted to perform better and are thus recommended for additional experimental testing. The calculated values of E_a (Figure 3.4) include computed barriers of four nitrides: *c*-BN, *h*-BN, HfN and ZrN, and one carbide: WC with higher magnitudes of E_a than W. These five candidates are therefore suggested for experimental testing as superior H diffusion barriers than W. The other five materials examined: Mo, TiN, TaN, NbC, and ZrC, have computed magnitudes of E_a for H diffusion comparable to that of W. Two factors were probed to determine their contributions to the higher computed barriers of *c*-BN, *h*-BN, HfN, ZrN and WC: steric hindrance and redistribution of electron density during the H hopping event. Therefore, strain energies (Figure 3.4), H charge state (Figure 3.6), and DOS plots (Figure 3.8) were compared to provide insight into their correlation with E_a.

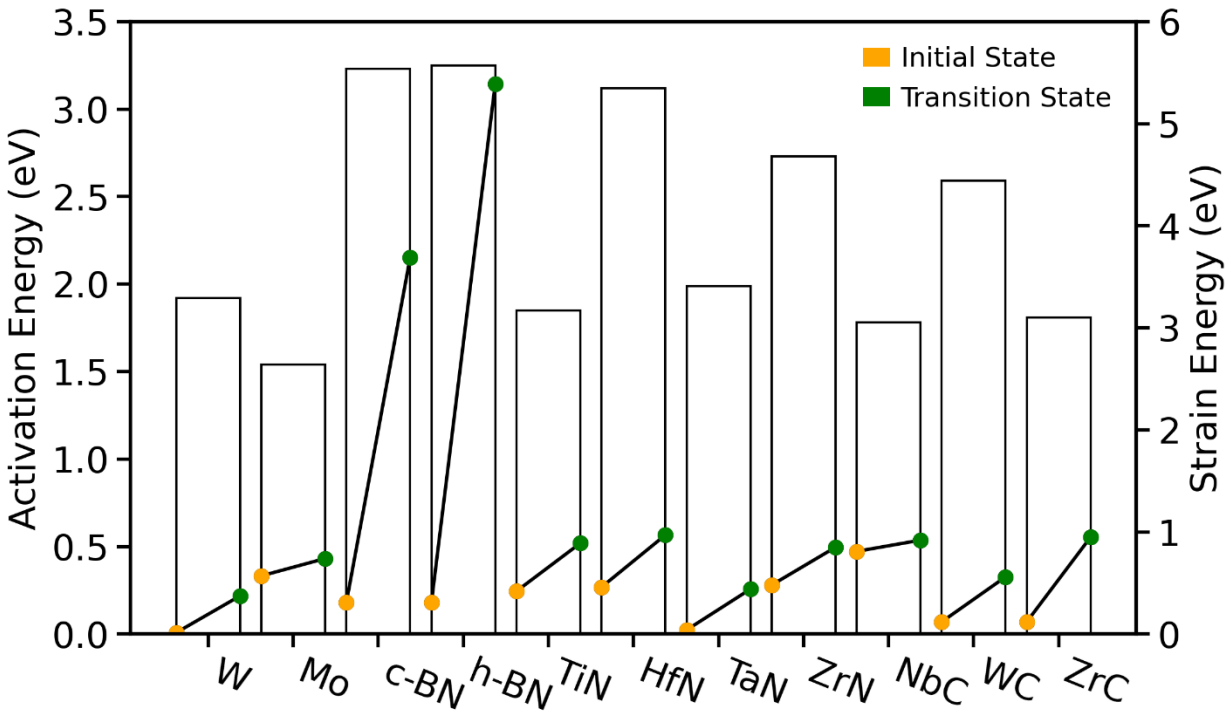

Figure 3.4 E_a (left, bars) and E_ε (lines, right) of screened materials for atomic H diffusion into the lowest energy surface from the most favorable adsorption site. Values for E_ε were calculated at the initial (orange) and transition states (green) in the H absorption pathway and are shown in that order across each E_a bar.

3.5.3 Contribution of Strain Energy to the Diffusion Barrier

The slightly higher values of E_a for H diffusion in the metal carbide and nitride materials than in the pure metals might partially result from steric hindrance and strain. As the H atom diffuses from the surface into these materials, it forces neighboring lattice atoms from their equilibrium positions. At its initial position adsorbed at the surface, the H atom is not surrounded by lattice atoms and therefore we compute much smaller strain energies for these states. These small values of E_ε are due to the relaxation of the surface atoms to minimize the energy of the adsorbed state (Figure 4.1). At the transition states, the strain energy for most nitrides and carbides is larger than that of the pure metals. This is due to the decreased interstitial space through which H can migrate in these materials because of the N and C atoms occupying interstitial positions that are normally unoccupied in pure metals. For instance, the diffusing H must pass through a cross-

sectional area defined by 3 lattice atoms in pure W (Figure 3.5 A and C) where this cross-section separates the initial and final states of the H atom hop. Thus, the strain energy correlates with the size of this cross-section. If the area is small, H must push nearest neighbor lattice atoms further from their equilibrium positions in order for the transition state to accommodate the H atom. Filling the interstitial spaces of metals with N or C reduces the cross-sectional area through which the H hops. In comparing WC to W, the cross section is now defined by 4 atoms (Figure 3.5 B) and the transition state for H shifts to directly between two W atoms in WC (Figure 3.5 D) from a position that extends into the open triangular space in W (Figure 3.5 C). The E_ε at the initial and transition states for WC are therefore slightly higher than for W, and the E_a is also larger.

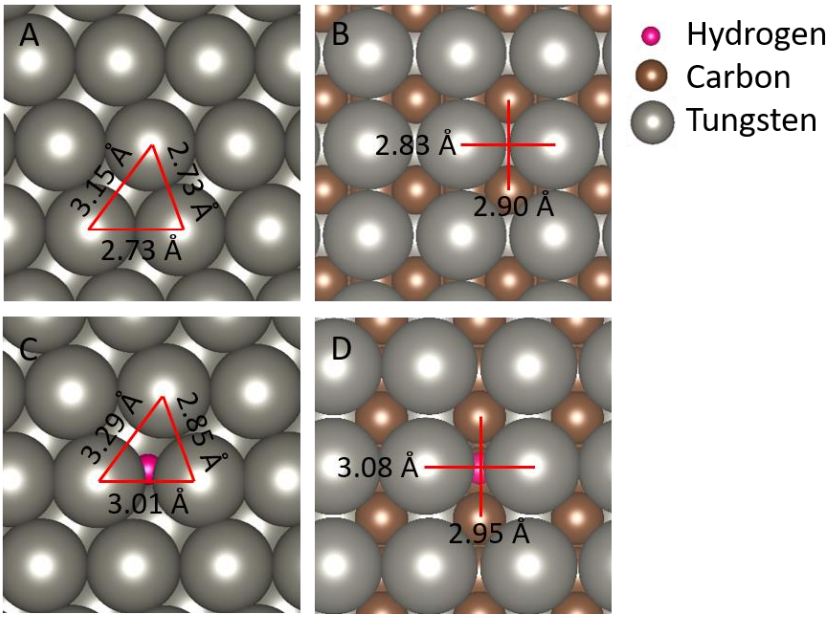

Figure 3.5 Interatomic spacing for the W (110) surface (A) and WC (100) surface (B) and interatomic distances at the transition state for H diffusion for W (C) and WC (D).

Increases in strain energy within the subset of transition metal nitrides and carbides screened does not, however, appear to correlate with an increase in E_a. This indicates a different characteristic is important in suggesting the magnitude of E_a. Across all materials analyzed, two

outliers exist that have both largest E_a and E_ε. These two outliers are both polymorphs of BN (Figure 3.4).

One of the primary differences between BN and the other materials examined is the presence of a bandgap. Wide bandgaps of 5.84 eV for *h*-BN [151] and 6.4 eV for *c*-BN [152] have been reported. Similar to what is observed in this work for H in BN, interstitial H atoms in wide bandgap oxide materials cause large displacements of the nearest neighbor lattice atoms [153]. Li and Robertson attributed the displacement of neighboring atoms in these oxides to electrostatic attraction between the negatively-charged neighboring atoms and the positively charged interstitial H or vice versa in the case of negatively charged H interstitials [153]. The connection between the charge state of the interstitial H and the displacement of neighboring lattice atoms suggests that the redistribution of electron density during the hopping event contributes to E_a and may also be the underlying cause of the high E_ε of the BN polymorphs where at the transition states, H forms a B-H-N complex that displaces the B and N atoms from their lattice positions.

3.5.4 H charge states along the diffusion pathway

The nature of the diffusing H atom within these materials was investigated through its charge state, which was calculated at the initial and transition states of a single H atom hop into the slab surface (Figure 3.6). Charge transfer between H and the investigated materials is dominated by electronegativity differences. H is more electronegative than the transition metals and boron (B) and is less electronegative than N and C (Table 3.1) [154]. Therefore, it is more likely to adopt a negative charge when bonded to a metal or B and a positive charge when bonded to C or N.

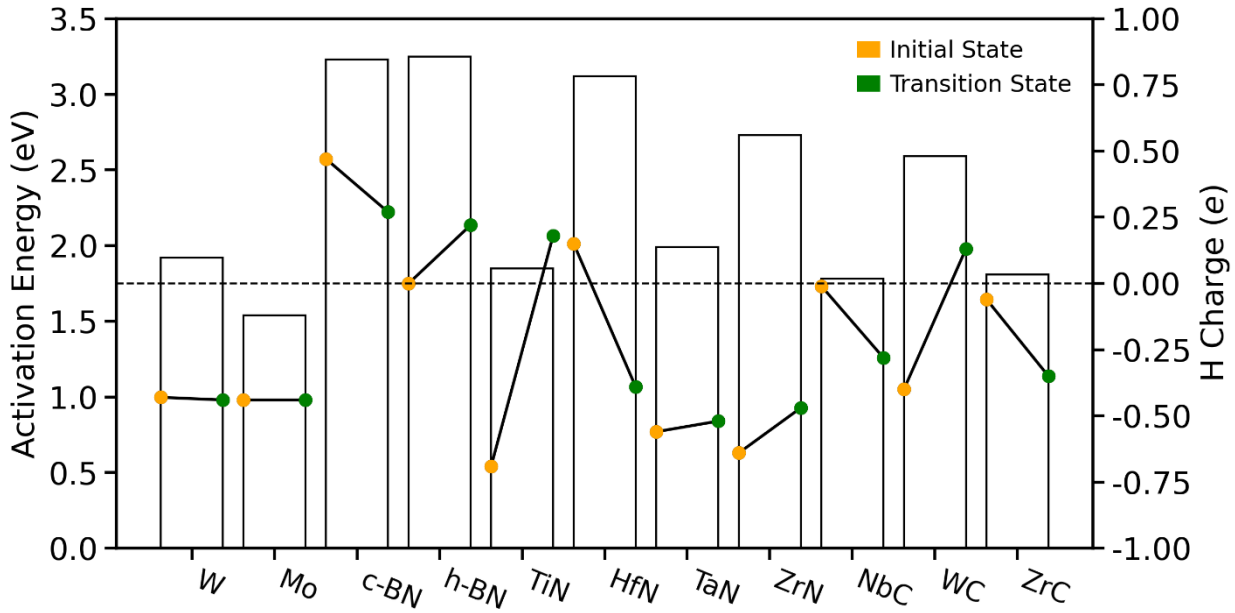

Figure 3.6 Activation energy (bars, left axis) and H charge state (solid lines, right axis) for diffusion of a single H atom into the lowest energy surface of the labeled refractory material. H charge states were calculated for the adsorbed adatom at the initial state on the surface and for the transition state for absorption into the surface, shown respectively across each bar.

Element	Pauling Electronegativity [154]
N	3
C	2.5
H	2.1
B	2
Mo	1.8
W	1.7
Nb	1.5
Ta	1.5
Ti	1.5
Zr	1.4
Hf	1.3

Table 3.3 Pauling electronegativities of each element within screened materials

Of the five materials with the largest values for E_a, both BN structures, HfN, and WC all show a positive H charge state along the diffusion pathway, indicating protic interstitial H diffuses less easily than hydridic H and is correlated with larger magnitudes of E_a. This trend is illustrated in comparing E_a to the sum (Σq) of the H charge states (q) at the initial and transition states of the

hopping event, which shows increasing E_a with increasing Σq (Figure 3.7). However, ZrN has a comparable barrier to the materials with protic H diffusion without following this trend (Figure 3.6). In this case, the large atomic size of Zr [155] may screen the diffusing H atom from the interstitial N atoms of greater electronegativity.

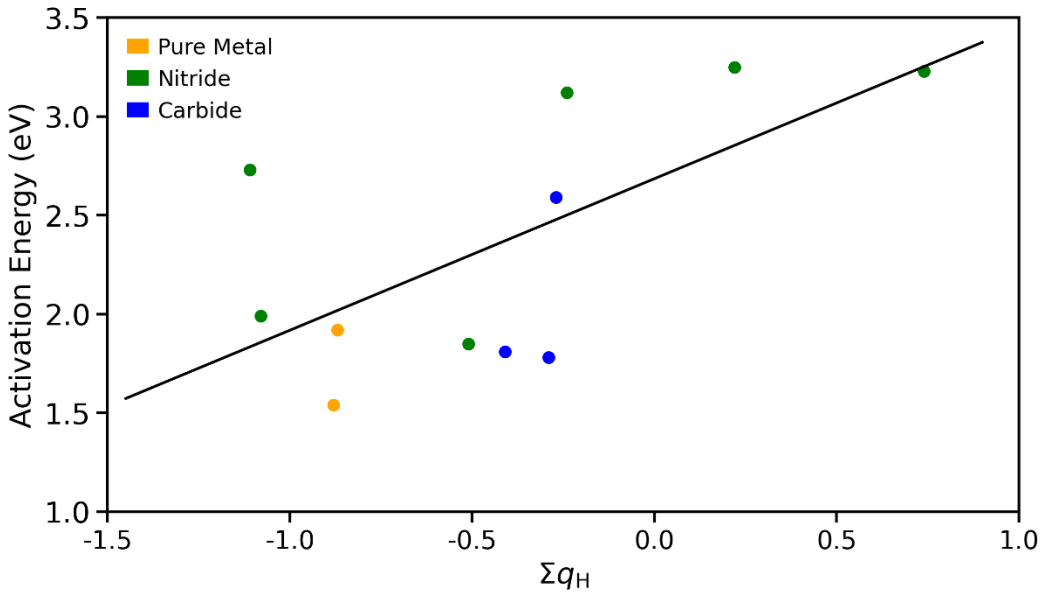

Figure 3.7 Activation energy versus the sum of hydrogen charge at the initial state and transition state for H absorption. Positive charges are correlated with larger energy barriers.

In W and Mo, H has a near-constant, negative charge state (Figure 3.6) indicating that it diffuses in these materials as a hydride. The consistent magnitude of H charge throughout the H hopping event within W and Mo indicates that there is a uniform difference in electronegativity between the diffusing H atom and the surrounding lattice atoms and that H charge in these pure metals does not contribute to an increase in E_a. However, for H diffusion in most transition metal nitrides the magnitude of the H charge state changes along the diffusion pathway. As H enters the slab, its distance from the N interstitial atoms lessens in all metal nitrides investigated in this work. This causes an increase in H charge ranging from less negative in TaN and ZrN to positive charges in TiN when bonded to a N atom at the transition state. However, H charge in HfN is instead

positive when in an adatom position on a surface Hf atom but negative at the transition state (Figure 3.6). The positive charge on H when at the initial state of the diffusion pathway into the HfN surface is possibly due to the lower electronegativity of Hf compared to Ta, Ti, and Zr allowing for more transfer of electron density to the N atoms and away from both the Hf atoms and the diffusing H atom. At the transition state in HfN, the H atom is between two Hf atoms that it can bond with and accept electron density from compared to atop a single Hf atom on the surface. At the transition state for H diffusion into the TiN surface, the H atom moves close to a N atom where it forms a bond and loses electron density unlike in TaN, HfN, and ZrN where it is most favorable to diffuse furthest from the N atoms and between two metal atoms. This difference in diffusion pathways could be due to the closer spacing of the smaller Ti atoms compared to the other transition metals (2.94 Å for Ti atoms compared to 3.17 Å for Hf atoms and 3.22 Å for Zr atoms). However, because the E_a in TiN is lower than those of the other nitride materials, this diffusion pathway does not appear to elicit a significant energy penalty, unlike the other cases of protic H diffusion.

In both BN polymorphs, H loses electron density to the more electronegative N atom at the transition state but at the initial state it accepts density from B in *h*-BN and again donates density to N in *c*-BN (Figure 3.6). Although there is ample space for H to diffuse through the center of a *h*-BN ring, it is energetically favorable for H to remain bonded to the lattice atoms when passing through a sheet as evidenced by its non-neutral charge. In both polymorphs of BN, H breaks a B-N bond at the transition state to form B-H and N-H bonds, which could be due to electrostatic interactions between the induced charges on the atoms after H adsorption to the BN slab surface where N is attracted to the excess electron density on the H atom in *h*-BN and the positive H atom is attracted to the excess charge on the B atom in *c*-BN. In both BN polymorphs, the diffusing H

has a more positive charge at the transition state as well as a larger E_a than in the other screened materials.

The charge state of H in the transition metal carbides correlates well with its environment within the lattice. The H atom presents a negative charge when bonded to the metal atoms and loses electron density to become less negative or positively charged when closer to a C atom. This is consistent with the electronegativity differences of these elements (Table 3.3) [154]. The slightly negative charge of the H atom when adsorbed to the top of a C atom in NbC and ZrC (Figure 3.6) indicates that it is bonded with both the C and the nearest metal atoms. In this position, it can gain electron density from the lower electronegativity metal atoms whereas it also loses electron density to C. On WC, which has a hexagonal crystal structure compared to the cubic structure of NbC and ZrC, H adsorbs between only W atoms where it is furthest from surface C atoms and has a more negative charge than when on the other metal carbide surfaces (Figure 3.6). However, as H diffuses into the WC slab, its distance from the nearest C atoms decreases significantly and it loses electron density thereby forcing it to take on a positive charge (Figure 3.6). This positive charge within the H hopping pathway in WC correlates with a larger E_a than those observed in the other carbides examined and is consistent with the trend observed in Figure 3.7.

3.5.5 Redistribution of electron density along the diffusion pathway

The redistribution of electron density and formation of new states from bond breakage and formation with the diffusing H atom affects the total energy of the system and therefore the magnitude of E_a. The changes seen in the DOS plots are similar within each of the four categories tested: pure metals (Figure 3.8 A), transition metal nitrides (Figure 3.8 B), boron nitrides (Figure 3.8 C) and transition metal carbides (Figure 3.8 D).

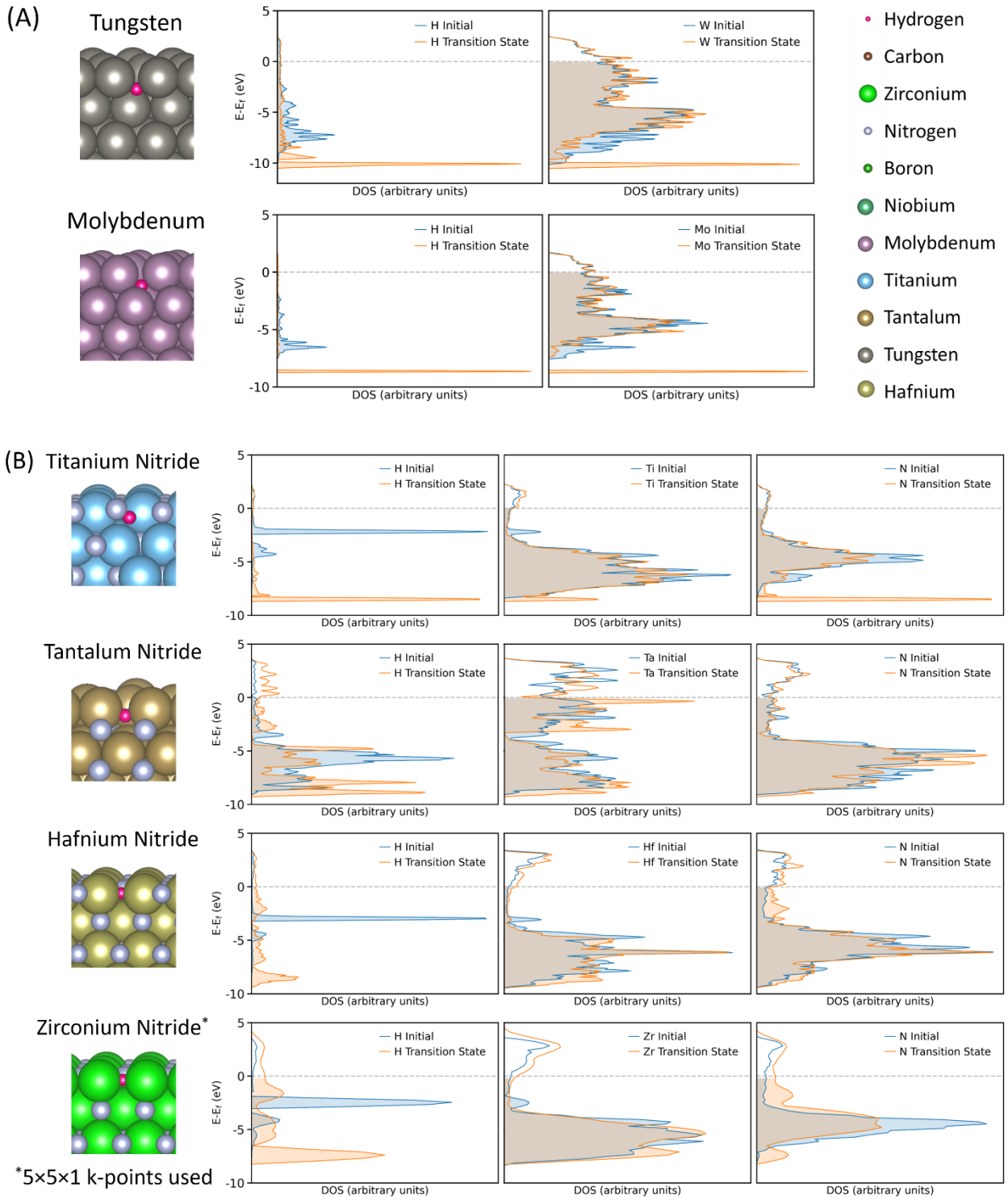
(A)
Tungsten
Molybdenum
H Initial
H Transition State
W Initial
W Transition State
Mo Initial
Mo Transition State
E-E$_f$ (eV)
DOS (arbitrary units)
Hydrogen
Carbon
Zirconium
Nitrogen
Boron
Niobium
Molybdenum
Titanium
Tantalum
Tungsten
Hafnium
(B) Titanium Nitride
Tantalum Nitride
Hafnium Nitride
Zirconium Nitride*
Ti Initial
Ti Transition State
Ta Initial
Ta Transition State
Hf Initial
Hf Transition State
Zr Initial
Zr Transition State
N Initial
N Transition State
*5×5×1 k-points used

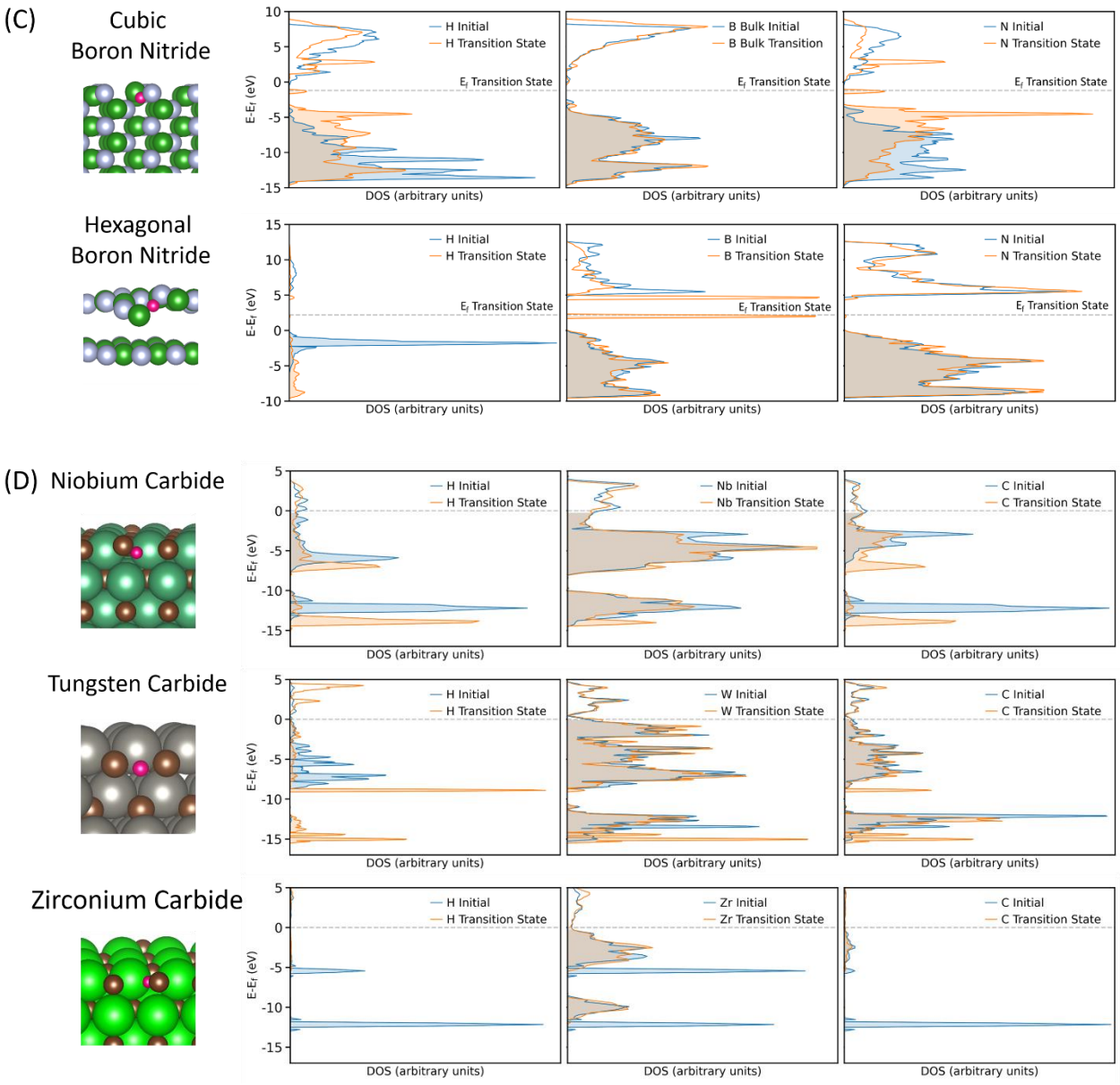

Figure 3.8 DOS plots of diffusing H atom, nearest neighbor cations, and nearest neighbor anions (from left to right) along the lowest energy diffusion pathway within each material category: pure metals (A), transition metal nitrides (B), boron nitrides (C), and transition metal carbides (D). DOS plots are overlaid for the initial and transition states and are separated by atom type (element). Left of each DOS series is an image of the transition state structure of the material named above the image.

On the surface of pure metals, H's DOS shows a broad spread in energy levels of filled states from 0 to 7.5 eV below E_F (Figure 3.8 A) that overlap with peaks in the DOS of the underlying metal atoms. As H diffuses into the pure metals, its filled states form a narrow peak

near -10 eV below the Fermi energy. This same broadening and narrowing of the filled states of the DOS has previously been reported for H interstitial defects within bulk W [40], Mo [156], and Fe [157] where interstitial H in vacancies in the metal lattice display broader DOS peaks. This is attributed to increased hybridization between the orbitals of H and the nearest neighbor metal atoms in vacancies and is correlated with the strong trapping effect of vacancies in the metal lattice on H interstitials. Atomic H is more stable within a vacancy than in an interstitial site. The similarity of the DOS plots of H on surfaces in this work to those of H in vacancies within bulk W and Mo suggests there is also stronger hybridization and therefore bonding of H to the surface atoms than at the TS of the H hop. Therefore, this loss of hybridization as H diffuses from the surface and into the material is unfavorable and contributes to the magnitude of the E_a.

At the transition states in the H hopping pathway, the shape of the DOS plots of H in transition metal nitrides (Figure 3.8 B) is similar to that of H in the pure metals (Figure 3.8 A). However, at the initial state, only the hexagonal nitride, TaN has a similar DOS to the pure metals. The DOS plots of the initial state of H on the surface of cubic nitrides (TiN, HfN and ZrN) show a narrow peak that overlaps with states in the DOS of the metal atoms in the respective lattice but not with the N atoms. This difference in the shapes of the DOS for H where broad peaks are observed on pure metals versus the narrow peaks observed on cubic nitrides could be due to the presence of N atoms pulling electron density away from the metals atoms and thereby making it unavailable for bonding between the H and metal atoms. This weaker bonding between the metal atoms with the interstitial H could be a contributor to the higher magnitudes of E_a in nitride materials than pure metals.

The discrepancy in DOS shape between the cubic and the hexagonal metal nitrides corresponds with the difference in the most favorable absorption sites for these materials. In

hexagonal TaN, H prefers a hollow site equidistant from 3 Ta atoms whereas in the cubic nitrides: TiN, HfN, and ZrN, it prefers to adsorb to the top of the metal atom. The difference in bonding of these materials is likely due to the differing number of valence electrons between group 4B elements (Ti, Hf, and Zr) and group 5B elements (Ta). Another difference observed between DOS plots is in that of TiN. Whereas TiN shows a large overlapping peak between N and H at the transition state, the other nitrides do not show such a significant overlap. This bonding between H and N in TiN is evident when examining the structure at the TS (Figure 3.8 B) where H diffuses next to a N atom in TiN and is also consistent with the positive H charge at the transition state (Figure 3.6). The H diffusion pathway in the other nitrides, however, is directly between nearest neighbor metal atoms.

The presence of H in the band gap materials analyzed in this study, *h*-BN and *c*-BN, induces the formation of filled mid-gap states at the transition state (Figure 3.8 C). The formation of mid-gap states is observed for interstitial H atoms in other insulating materials as well, such as alumina [158]. In both BN polymorphs, the H atom forms a B-H-N complex at the transition state giving the H atom a similar charge at the transition state in both materials (Figure 3.6). As H diffuses from its adsorption site on the surface and into these materials, the Fermi energy, $E_{F,}$ shifts in accordance with the energy level of the mid-gap state. As H diffuses into the slab, E_F decreases for the cubic polymorph and increases for the hexagonal polymorph relative to E_F of the adsorbed H adatom on each material's surface (Figure 3.8 C). This ΔE_F is larger at the higher-energy transition state and smaller at the relaxed final state in both crystal structures. In addition, ΔE_F is larger in the hexagonal polymorph than in the cubic polymorph indicating larger shifts in E_F is likely unfavorable because it correlates with increased system energies.

In both ZrC and NbC, H favorably adsorbs atop a surface C atom which causes the overlap of DOS peaks between H and the metal atoms at the initial state. However, in WC, H prefers to adsorb at a bridge site between two W atoms. The peak shapes at the initial state of H on the WC surface are similar to those of pure W where hybridization and strong bonding is observed. As H diffuses into the WC slab, it loses this hybridization and more narrow peaks are observed in the DOS. This unfavorable loss of hybridization in WC compared to ZrC and NbC could contribute to the much larger E_a of WC than the other two carbides.

3.5.6 Experimental validation of nitride stability

Although the nitrides and carbides examined have high melting points and in certain cases high E_a for H diffusion (e.g. BN, HfN, ZrN), decomposition into pure metals and gaseous N_2 or NH_3 can occur below the melting point. This will lower not only the E_a [47, 89], but also the melting point of the coating, posing a risk to the coating efficacy and integrity during use. Therefore, N vacancy formation energies, $E_{vf,NH3}$ and $E_{vf,N2}$, were computed and compared against both NH_3 and N_2 formation, respectively. The larger the E_{vf}, the less likely the system is to overcome the energy barrier and form a N vacancy.

Five screened nitrides were computational analyzed for E_{vf}: BN, HfN, TaN, TiN, and ZrN (Figure 3.9). Positive energies indicate thermodynamic stability with respect to N_2 and NH_3 formation, and the only material predicted to fully decompose within the plotted temperature range is TiN which favors gaseous N_2 formation over fixed N retention above 2550 K. The nitrides examined at 1773 K should retain their fixed N content during testing in H_2 given their positive values of E_{vf}. However, it should be noted that these metal nitrides begin to oxidize at ~1073 K in air [159]. The computed values for $E_{vf,NH3}$ and $E_{vf,N2}$ at 1773 K and 2773 K indicate that forming gaseous N_2 is thermodynamically more favorable than NH_3. At 1 atm, the decomposition of NH_3

into N_2 and H_2 is thermodynamically favorable above 570 K, therefore only values of $E_{vf,N2}$ were compared above 570 K.

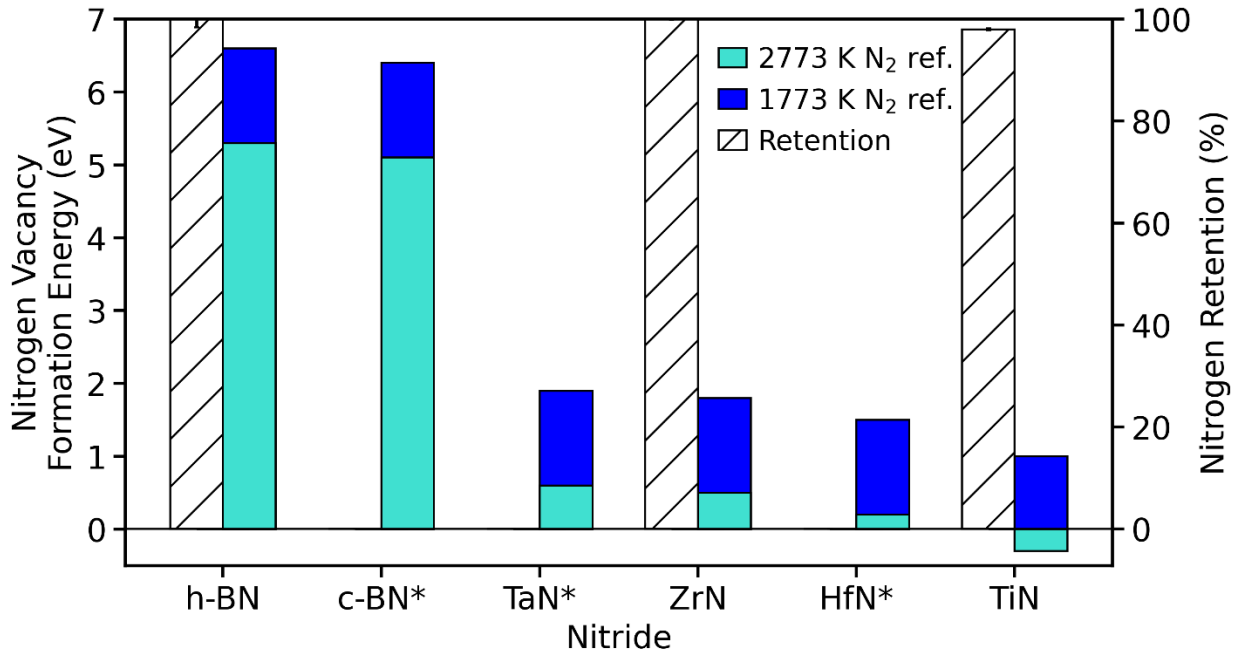

Figure 3.9 Nitrogen vacancy formation energies (solid, left axis) at 1773 K and 2773 K relative to N_2 formation as noted by the legend and fixed nitrogen retention at 1773 K (hatched, right) of commercially available refractory nitrides. Materials are shown in order of decreasing predicted stability from left to right. *c-BN, TaN, and HfN were not experimentally tested

Nitride stability under hot H_2 flow was experimentally probed to compare to computational predictions. Bulk *h*-BN, TiN, and ZrN powders were subjected to flow of 20% H_2 in Ar balance for 3 hours at 1773 K. It was seen that *h*-BN and ZrN retained all of their nitrogen content throughout the experiment and TiN retained over 98% (Figure 3.9) as predicted by their positive vacancy formation energies. It is possible that the small loss of fixed N in TiN was partially due to the slight presence of oxygen that remained in the system after inert gas purging. Only TiN and HfN are computed to have a negative $E_{vf,N2}$ below their respective melting points: TiN at 2550 K, which disqualifies it from use in NTP engines, and HfN at 2920 K which is still above the NTP operating temperature. The high values of $E_{vf,N2}$ in both BN polymorphs at 2700 K makes it the

most attractive material for NTP applications with respect to predicted N retention and the lower values of $E_{vf,N2}$ in TaN, ZrN, and HfN (in order of decreasing predicted stability) make them more susceptible to loss of N during operation.

3.6 Conclusions

Eleven materials including refractory nitrides, carbides, and pure metals were compared with respect to E_a for H diffusion. The initial and transition states of a single H hop into the surfaces of these materials were further analyzed and compared to gain insight into the contributing variables for higher or lower values of E_a. Variables investigated were E_ε, H charge state, and the redistribution of electron density as indicated by the DOS. It was observed that the materials with the largest values for E_ε, *h*-BN and *c*-BN, also had the largest values of E_a indicating the presence of an energy penalty from rearrangement of atoms. However, a pattern was not evident amongst the other materials, which suggested another variable was contributing to barrier height in addition to E_ε. Because BN was the only material screened with an electronic band gap, it is likely that bonding between H and the lattice atoms and redistribution of electron density contribute to the differences in E_a observed between the screened materials.

The majority of the high E_a materials: *h*-BN, *c*-BN, HfN, and WC, exhibited a positive H charge state along the diffusion pathway indicating H loses electron density to the lattice atoms in these materials. The negative charge state in transition metal nitrides and carbides indicated the formation of hydrides in these materials between the metal atoms and the diffusing H atom. The correlation between more positive H charge along the diffusion pathway and larger values of E_a indicates that diffusion of protic interstitial H atoms is less favorable than that of hydridic interstitial H atoms.

Changes in the DOS were also examined to analyze redistribution of electron density during H diffusion. Formation of mid-gap states in the insulating material tested, BN, were seen due to the presence of the H atom at the transition state. The large values of E_a of both BN polymorphs suggest the deep mid-gap state is unfavorable and a contributing factor to E_a. DOS plots of H diffusion into W, Mo, and WC show an energetically unfavorable loss of hybridization from the initial to the transition state which contributes to the diffusion barrier height. The lack of hybridization seen in the H DOS in the cubic transition metal nitrides and carbides analyzed compared to the pure metals is likely due to the N and C interstitial atoms pulling electron density away from the metal-H bonds, making diffusion less favorable.

Through calculation of vacancy formation energies and experimental testing, all screened metal nitrides are predicted to retain their fixed N content at 1773 K. However, TiN is computationally predicted at 2550 K to form N vacancies with respect to N_2 formation. Of the nitrides analyzed, the BN polymorphs are predicted to be most thermodynamically stable at NTP operating temperatures with respect to fixed N loss, followed by TaN, ZrN, then HfN.

The materials computationally predicted to perform best as H EBC materials are BN, HfN, ZrN, and WC which are suggested for experimental H permeation testing. Future work is suggested to determine the pre-exponential factors associated with the materials with large values of E_a.

3.7 Acknowledgements

This work was funded by the National Aeronautics and Space Administration's (NASA) Early Stage Innovations grant 80NSSC18K0254. This research made use of supercomputing resources of the High-Performance Computing Center at the Idaho National Laboratory, which is supported by the Office of Nuclear Energy of the U.S. Department of Energy and the Nuclear

Science User Facilities under Contract No. DE-AC07-05ID14517. This investigation also utilized the RMACC Summit supercomputer, which is supported by the National Science Foundation through NSF awards ACI-1532235 and ACI-1532236, the University of Colorado Boulder, and Colorado State University. The Summit supercomputer is a joint effort of the University of Colorado Boulder and Colorado State University. The authors would also like to acknowledge Dr. Jacob Clary for valuable discussions.

Chapter 4

Atomic Layer Deposited Boron Nitride Nanoscale Films Act as High Temperature Hydrogen Barriers

Most of the content in this chapter appears verbatim in the following manuscript:

Sarah K. Bull, Theodore A. Champ, Sai V. Raj, Robert C. O'Brien, Charles B. Musgrave* and Alan W. Weimer*. Atomic Layer Deposited Boron Nitride Nanoscale Films Act as High Temperature Hydrogen Barriers. (2021) [Under revision].

4.1 Abstract

Hydrogen environmental barrier coatings reduce hydrogen diffusion and concomitant hydrogen embrittlement of materials such as those used in nuclear and fuel cell applications where hydrogen is used as a fuel source. In this work, atomic layer deposition (ALD) was used to coat substrates with boron nitride (BN) films of approximately 6, 8, and 15 nm thicknesses. Differential thermal analysis of the coated samples in hydrogen gas showed resistance to reaction with hydrogen to at least 1713 K. Diffusion of atomic hydrogen into the hexagonal BN (001) surface and between sheets as well as material stability were computationally studied using density functional theory. A high activation energy of 3.25 eV was calculated for atomic hydrogen diffusion into the (001) hexagonal BN surface through a sheet. However, lower activation energies of 1.35 eV, 1.11 eV, and 0.12 eV were computed for unique hydrogen diffusion pathways between sheets, suggesting that sheet orientation parallel to the substrate surface is vital for attaining desirable barrier film properties. A predicted positive nitrogen vacancy formation energy of 5.3 eV at 2773 K suggests that hexagonal BN is stable at nuclear thermal propulsion operating temperatures, and stability was confirmed experimentally up to 1773 K.

4.2 Introduction

Nuclear thermal propulsion (NTP) engines that use hydrogen (H_2) as a propellant offer an attractive alternative to chemical combustion engines for in-space propulsion systems because of their high specific impulse [17]. These engines operate by heating H_2 in a nuclear reactor core to >2700 K before expelling it from a supersonic nozzle to generate thrust [17]. In one particular configuration, the fuel elements are hexagonal-shaped cermet rods composed of uranium dioxide (UO_2) ceramic fuel pellets that heat the propellant and are embedded in a metallic tungsten (W) matrix. High-aspect-ratio flow channels along the length of the elements maximize the interfacial surface area between the propellant and the heat source. Hydrogen is chosen as the propellant for NTP engines because its low molecular weight allows for specific impulses of 900 s, twice that of a chemical combustion engine [5]. However, H_2's small size also enables it to diffuse through materials leading to hydrogen embrittlement [7, 8, 35, 160]. The embrittlement of these cermet NTP fuel elements is primarily driven by the formation of uranium hydrides and gaseous H_2 bubbles that exert pressure on the surrounding material, resulting in catastrophic failure due to crack formation and fracture [10, 21]. For metals, such as the W that forms the matrix of the fuel elements, H_2 can decrease the interfacial strength between grains, leading to intergranular fracture and an increase in the ductile to brittle transition temperature [7, 8].

Other applications beyond NTP also require limiting H_2 diffusion. For example, the detrimental effects of hydrogen embrittlement have been observed in fuel cells operating at temperatures up to 1273 K [11, 88, 161] as well as in materials of nuclear fusion reactors for power generation that utilize hydrogen isotopes as a plasma source and operate with cooling water to maintain wall temperatures near 573 K [31]. Minimizing H_2 diffusion in pipeline materials is essential not only to prevent embrittlement, but also to improve H_2 fuel retention [9, 162]. One

approach to address these issues is to develop environmental barrier coatings (EBCs) to minimize H_2 diffusion into and through susceptible materials.

Previous EBCs have included pure metals, graphite, carbides, nitrides, and oxides, and have been formed via aluminizing and oxidation [12, 31, 35, 36], atomic [37] and chemical [31, 38] vapor deposition, magnetically enhanced plasma ion plating [39], and packed-bed cementing [31]. The current state-of-the-art EBC for NTP applications is W deposited via chemical vapor deposition (CVD) on UO_2 spheres before they are embedded in the metallic matrix. However, this method cannot uniformly coat within the H_2 flow channels given that deposition reactions are not self-limited [26]. Tungsten is chosen for its retained strength at elevated temperatures, high melting point (3683 K), thermal conductivity and low H_2 diffusivity relative to other pure metals [163]. Nevertheless, it is still subject to hydrogen embrittlement [23, 163, 164]. In the CVD process, not only do reactions occur on the substrate surface, but because reactions are not self-limiting, they also occur in the gas phase, which leads to particle formation [27]. These particles are then incorporated into the coating, creating a pore network of low-energy diffusion pathways that result in poor hydrogen diffusion barriers [25]. Gas phase reactions in CVD also generally result in irregular film deposition, especially in high-aspect-ratio channels, such as those throughout the hexagonal NTP fuel elements, where non-uniform deposition often clogs the channel entrance [26]. Development of better barrier materials that reduce H_2 diffusion and embrittlement, and deposition with a coating method that does not form particles and that uniformly coats the surfaces of high-aspect-ratio pores, is essential to the viability of this technology.

Herein, we report on the use of atomic layer deposition (ALD) to create a boron nitride (BN) EBC to reduce high temperature H_2 diffusion. ALD deposits amorphous films that would limit film crystallization to the hexagonal layered structure (*h*-BN) [55, 56] at the low pressures

used in this work, as crystallization to the cubic phase requires high pressures (>5.5 GPa) and temperatures (>1773 K) [58]. Previous experimental studies, however, have examined both *h*-BN and cubic BN (*c*-BN). Steel substrates coated with *c*-BN thin films exhibited [39, 59] up to a two order of magnitude reduction of hydrogen permeability with only a 1 μm thick film of *c*-BN and a 0.5 μm thick SiC tie layer [39]. The effectiveness of thin *h*-BN barriers has been shown to depend on the deposition method and resulting microstructure. Hexagonal BN deposited via ion beam assisted deposition (IBAD) resulted in (002) planes oriented perpendicular to the substrate and thus facile diffusion and high H_2 permeability through the film [59]. However, polycrystalline *h*-BN films deposited via radio frequency magnetron sputtering reduced the permeability of H_2 in metallic samples [60]. In addition, *h*-BN flakes parallel to their substrate surface were observed to trap molecular H_2 as bubbles that were stable up to 1073 K without outward diffusion [61]. These promising results motivated our investigation of ALD BN as a H_2 barrier coating with the goal of reducing H_2 diffusion into substrates at high temperatures, such as the operating temperatures of solid oxide fuel cells and NTP engines.

ALD utilizes sequential, self-limited surface reactions to ideally deposit a film atomic layer by atomic layer. As a result, ALD creates low-defect, nanoscale-thick films that are chemically bonded to the substrate [63]. EBCs deposited by ALD have been shown to effectively protect substrates from oxidizing environments at high temperatures [87]. In this work, the effectiveness of EBCs toward blocking hydrogen diffusion in a reducing environment is experimentally and theoretically investigated. Avoiding the formation of defects in *h*-BN sheets is critical given the calculations by Shevlin and Guo [165] that predict that both B and N vacancies as well as antisite defects (substitutions of one atom type by the other) can cause molecular H_2 adsorption to switch from an endothermic to an exothermic process, thereby making the first step in the diffusion

pathway thermodynamically favorable. In addition, ALD reactions are self-limiting; thus, ALD is not a line-of-sight deposition technique, which enables ALD to deposit uniform films on high-aspect-ratio features, such as within the long and narrow channels of NTP fuel elements [27, 55, 63]. The nanoscale thicknesses of ALD deposited films also provide the added benefit of increased elasticity compared to thicker films, lowering the risk of delamination or cracking from coefficient of thermal expansion (CTE) mismatch [94]. This issue is relevant in coatings for reducing H_2 embrittlement of ceramic fuel in NTP engines that operate at >2700 K because UO_2 and UN have larger CTEs of 10.52×10^{-6} K^{-1} and 8.61×10^{-6} K^{-1} [105], respectively, than W, the state-of-the-art coating material, which has a CTE between 6.5×10^{-6} K^{-1} and 7.7×10^{-6} K^{-1} [166] and *h*-BN with a computed CTE of 7.2×10^{-6} K^{-1} [167]. The results presented here suggest the use of nanoscale BN ALD films to protect susceptible substrates from H_2 diffusion and to serve as a candidate EBC material for NTP fuel elements.

4.3 Materials, experimental and theoretical methods

4.3.1 Atomic layer deposition of BN

Boron nitride ALD coatings were deposited on zirconia (ZrO_2) nanopowder (U.S. Research Nanomaterials) and 5 wt% yttria stabilized zirconia (YSZ) micropowder (Glen Mills VHD milling powder) using a 316 stainless-steel fluidized bed ALD reactor as detailed elsewhere [65, 66, 95]. Components of this ALD reactor system have been described in detail previously [37]. The particles of the ZrO_2 nanopowder averaged 40 nm in diameter with a specific surface area of 11.7±0.1 m^2/g. To determine the film growth rate, 80 BN ALD cycles were performed on 6 g of untreated nanopowder. The YSZ powder averaged 100 μm in diameter, giving it a theoretical specific surface area of 0.01 m^2/g. Boron nitride ALD was performed on 15 g of YSZ

micropowder, 3 g of which was removed after both 115 and 165 BN ALD cycles and the remainder after 310 ALD cycles.

Boron nitride ALD using boron trichloride (BCl_3) and high-purity ammonia (NH_3) was performed at 500 K based on the ALD window reported by Ferguson et al. [55]. Gas lines to and from the fluidized bed were kept above 373 K. Boron trichloride with a purity of at least 99.9% and anhydrous NH_3 with a purity >99.98% were procured from Sigma-Aldrich, St. Louis, Missouri. Given that the dosing time required to reach substrate saturation depends on the amount of surface area in the reactor bed, dosing times were altered in response to changes in the mass of the loaded powder and its specific surface area. Because ALD is self-limiting, dosing beyond saturation does not lead to more deposition but does waste precursor. For the loadings used in this work, doses to reach breakthrough averaged 300 s and 120 s for BCl_3 and ammonia, respectively, and nitrogen purges were performed for 1800 s and 2100 s, respectively. However, times were dynamically adjusted in response to changes in the total surface area to ensure adequate time for surface saturation and reaction completion.

The average deposition per cycle on ZrO_2 powder samples was determined using an FEI Tecnai G2 20 S-Twin transmission electron microscope (TEM). A TEM sample was prepared from YSZ powder coated with 310 BN ALD cycles by focused ion beam (FIB) milling using an FEI Quanta 3D FEG. This sample was imaged using an FEI Tecnai TF30-FEG STwin TEM equipped with energy dispersive x-ray (EDX) detectors. The thickest coating on the YSZ powder was analyzed for surface elements by x-ray photoelectron spectroscopy (XPS) using a PHI-5600LS with a monochromatic Al (1486.6 eV) x-ray source. Charge neutralization was performed on the insulating samples, and the neutralization electron current and energy were chosen to align the C

1s peak to 284.8 eV. Peak-fitting of the XPS data was performed using reported reference values [96].

4.3.2 Stability testing of bulk BN

Bulk BN of HCV grade was procured from Advanced Ceramics Corporation to analyze nitride stability at high temperatures in a 20% H_2 in argon (Ar) balance environment. An alumina crucible was loaded with 0.76 g of bulk BN powder and heated to 1773 K at a rate of 10 K/min. The sample was held at 1773 K for 3 hours and ramped down to room temperature at the same rate. Temperature ramps were done under 40 cm^3/min Ar flow and the high temperature hold was done under 10 cm^3/min H_2 in addition to the Ar flow. The powder was tested both before and after this H_2 heat treatment for fixed nitrogen content using a LECO TC600 fixed O and N light element analyzer.

4.3.3 Differential thermal analysis

Differential thermal analysis (DTA) was performed using a Netzsch STA 449 F3 housed in an Ar-purged glovebox as previously described [37] for samples tested in a H_2 environment. A Netzsch STA 449 F1 was used for sample testing in a pure Ar environment. Purge gas of either 6% H_2 in Ar or pure Ar was dosed at 20 cm^3/min throughout the experiment, in addition to 50 cm^3/min of Ar protective gas. An initial ramp rate of 10 K/min was used to reach the maximum furnace temperature of 1873 K for the F3 instrument and 1773 K for the F1 instrument followed by an isothermal hold for two hours before ramping down to room temperature at 15 K/min. Only data from the initial ramp were compared where time and temperature were equivalent on both instruments.

4.3.4 Computational methods

Atomic hydrogen (H) diffusion in *h*-BN was investigated using density functional theory (DFT). H atom hops from the most favorable adatom position atop a B atom on the lowest energy surface to the underside of the same B atom as well as hops between sheets of the first subsurface layer of *h*-BN were computed. The Vienna *Ab initio* Simulation Package (VASP) was utilized to perform DFT calculations using periodic boundary conditions, the strongly constrained and appropriately normed semi-local density functional (SCAN) [125] and the projector augmented-wave (PAW) pseudopotentials [68-73]. Calculations using a supercell slab model of the surface were performed using a 520 eV energy cutoff and a 5×5×1 *k*-point expansion. Periodically repeated BN slabs consisting of 72 atoms were separated by 12 Å of vacuum space to limit interactions between the diffusing H atom and the bottom of the slab. The lateral dimensions of the supercell were chosen to limit interactions of the H atom with its periodic image. Atomic positions of the bottom two layers of the slab were constrained to reduce the computational expense of the calculations. The transition states (TS) for H diffusion were determined using the nudged elastic band (NEB) method. Bader charge analysis was used to determine the charge state of the diffusing H atom. Both methods were implemented within VASP using scripts developed by the Henkelman Group [98, 100, 101, 128, 129, 132, 133, 168-171]. Density of states (DOS) plots were generated from a converged single-point calculation with a higher density 10×10×1 *k*-point mesh at the initial, transition, and final states. Bulk BN calculations were performed using a 72 atom supercell with a 6×6×6 *k*-point expansion and 550 eV energy cutoff. Nitrogen vacancy formation energies were calculated from these bulk systems using gaseous diatomic nitrogen as the reference state.

4.4 Atomistic Modeling of H Diffusion

4.4.1 Computational analysis of diffusion

Hexagonal BN was computationally hypothesized to be a promising material to improve upon W, the current state-of-the-art H_2 EBC material, due to *h*-BN's larger activation energy (E_a) for H diffusion into its most favorable surface, 3.25 eV compared to W's 2.0 eV [37]. The predicted performances of *h*-BN and W as H diffusion barrier materials were compared based on their computed E_as for H diffusion. The diffusion of interstitial H in materials is expressed by an Arrhenius equation as:

$$D = D_0 \exp\left({}^{-E_a}/_{k_B T}\right) \quad \text{Equation 4.1}$$

$$D_0 = \alpha a^2 v \quad \text{Equation 4.2}$$

where E_a is the activation energy for H diffusion in the material, D_0 the pre-exponential factor, α a numerical constant relating to the locations of the interstitial positions, *a* the lattice constant, and *v* the attempt frequency [135]. The exponential Boltzmann factor provides the fraction of hop attempts that have sufficient energy to surmount E_a, which is equivalent to the energy difference between the TS (E^{TS}) and the initial state (E^0) along the minimum energy diffusion pathway and was computed here using DFT:

$$E_a = E^{TS} - E^0 \quad \text{Equation 4.3}$$

The pre-exponential factor, D_0, depends on the length of an atomic hop and the frequency of hop attempts and can be related to the activation entropy through the relationship of the rate of the diffusion process and the activation free energy of an atomic hop. However, D_0 was not calculated in this work, as it was previously reported to range in order of magnitude from 10^{-7} experimentally [136] to 10^{-8} computationally [43, 109, 137] for H diffusion in W and 10^{-8} experimentally for both deuterium in h-BN [60] and H in amorphous BN [60, 138]. Given the

similarity in magnitude of these prefactors, in addition to the high computational cost of calculating them for surface absorption, only activation energies were calculated and compared. Owing to the exponential, small differences in the magnitude of E_a cause large differences in the magnitude of the exponential term as well as the resulting diffusion coefficient. However, this is partially mitigated by the high temperatures at which diffusion occurs in solid-oxide fuel cells and NTP engines. Nonetheless, given the usual high sensitivity of diffusion on the Boltzmann factor relative to the prefactor, it is common to report only activation energies when comparing material permeabilities [47, 142, 143].

The atomic charge states of the diffusing H atom were calculated based on a Bader population analysis [101] as implemented in code available from the Henkelman group [98, 132, 133, 171]. The difference between the calculated electronic charge and the charge of the nucleus of each atom was used to define an atom's charge state.

Strain energies to distort the h-BN structure to the TS were used to quantify steric hindrance along the H diffusion pathway. They were calculated as:

$$E_{\varepsilon} = E^{TS,no\ H} - E^{0,no\ H} \qquad \text{Equation 4.4}$$

where E_{ε} is strain energy, $E^{TS,no\ H}$ the energy of the B and N atoms constrained in their TS configuration with H removed, and $E^{0,no\ H}$ the energy of the B and N atoms in the bare crystalline surface as modeled by the relaxed slab before the introduction of H.

The nitrogen vacancy formation energy, $E_{vf,N}$, was calculated as:

$$E_{vf,N} = E_{v,bulk} - E_{bulk} + \frac{1}{2}E_{N_2} \qquad \text{Equation 4.5}$$

where $E_{v,bulk}$ is the energy of the system with a single N vacancy, E_{bulk} the energy of the system with no vacancies, and E_{N_2} the energy of N_2 adjusted for chemical potential at temperatures above 0 K. This adjustment is calculated as [144]:

$$\Delta\mu(T, P_0) = \left[H_0 + C_p(T - T_0)\right] - T\left[S_0 + C_p \ln\left({}^{T}/_{T_0}\right)\right] \qquad \text{Equation 4.6}$$

Tabulated values were used for the standard diatomic nitrogen gas reference [145]. Only the removed ion has a chemical potential adjustment because of the near cancellation of the term when taking the difference in energies between the bulk system with and without the vacancy. The larger the vacancy formation energy, the less likely this type of defect is to form, suggesting that the material is more stable.

4.5 Results and discussion

4.5.1 Computational H diffusion analysis

BN was chosen as an EBC material to explore experimentally for preventing H_2 diffusion due to its favorable theoretical performance compared to the legacy material, W, based on calculations in this work. This predicted performance was investigated by comparing E_as for atomic H diffusion into the surface of each material. Tungsten's computed E_a for H diffusion was 2.02 eV, corresponding to diffusion from the most favorable adsorption site into the first subsurface layer, and 0.19 eV for diffusion within the bulk [37]. Consequently, W's performance primarily depends on preventing H from entering the bulk. Only *h*-BN was computationally investigated in this work because crystallization of the amorphous as-deposited BN thin film at atmospheric pressure preferentially forms the hexagonal crystal structure.

We computed an E_a for atomic H diffusion of 3.25 eV from an absorbed position on a B surface atom on the most energetically favorable (001) crystallographic plane of the *h*-BN crystal (Figure 4.1) through the *h*-BN sheet. Additionally, activation energies for H hopping between the top two *h*-BN sheets were computed for the three pathways depicted in Figure 4.1 (b-d): 1) from the underside of a B atom of the top sheet to on top of a B atom of the subsurface sheet, 2) from the underside of a B atom on the top sheet to the underside of its nearest neighbor N atom of the

top sheet, and 3) from on top of a B atom on the second sheet to on top of the nearest neighbor N atom of the second sheet. We computed activation barriers for these three pathways of 0.12, 1.35, and 1.11, respectively. The E_a of 0.12 eV for diffusion from a B atom of one sheet to that of the neighboring sheet, calculated by DFT in this work, is very similar to the previously computed barrier of 0.08 eV from well-tempered metadynamics simulations [172]. Unlike W, *h*-BN does not catalyze the dissociation of the H_2 molecule. Instead, H_2 dissociation on *h*-BN requires a significant E_a of 2.4 eV, as calculated by Shevlin and Guo [165]. However, previous experimental studies analyzed the presence of hydrogen within *h*-BN and observed that the diffusing species were H atoms [172]. In addition, studies in amorphous BN observed an overwhelming presence of dispersed monohydrides and no trapped H_2 molecules [138], which implies that atomic H diffusion is more likely than H_2 molecular diffusion and supports analysis of only the former in the present study.

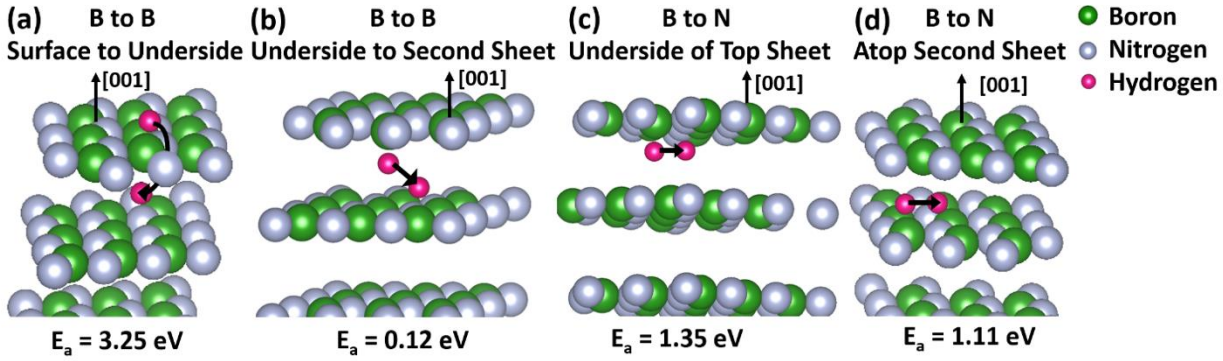

Figure 4.1 Atomic H diffusion pathways into and between *h*-BN sheets. Respective activation energies are listed below each pathway. Green spheres represent boron atoms, gray nitrogen atoms, and pink hydrogen.

The TSs along all four diffusion pathways were further analyzed and compared to the relaxed initial states in terms of the E_ε of the BN lattice atoms (Figure 4.2) and DOS (Figure 4.3). At the TS, the nearest neighbor B and N atoms to the diffusing H atom relax out-of-plane, resulting in an increase of over 5 eV in energy of the *h*-BN slab, compared to the unperturbed surface. This

is likely to contribute to the high E_a for H diffusion into the *h*-BN surface, compared to diffusion between sheets where B and N lattice atoms do not have to accommodate the diffusing species (Figure 4.2). The projected DOS of the s orbital of the diffusing H atom was computed at both the relaxed initial state and the TS along each diffusion pathway. The labels of the DOS plots in Figures 3a-d correlate with the labels of the diffusion pathways in Figures 1a-d. Dissociation of the B-N bond and the formation of a B-H-N complex at the TS for the absorption pathway into the (001) surface results in the appearance of a new mid-gap state in the TS DOS near 1.5 eV above the Fermi energy of the relaxed structure (Figure 4.3a). Similar mid-gap states are observed when hydrides are formed within insulating materials [158]. Bader charge analysis indicates that the H is protic (positively charged) at the B-H-N TS of pathways involving both B and N atoms (a, c, and d). On the other hand, Bader analysis indicates that H is hydridic (negatively charged) when absorbed to a B atom. This is consistent with the greater electronegativity of N relative to H and of H relative to B [173] and indicates that H loses electron density to N through bond formation.

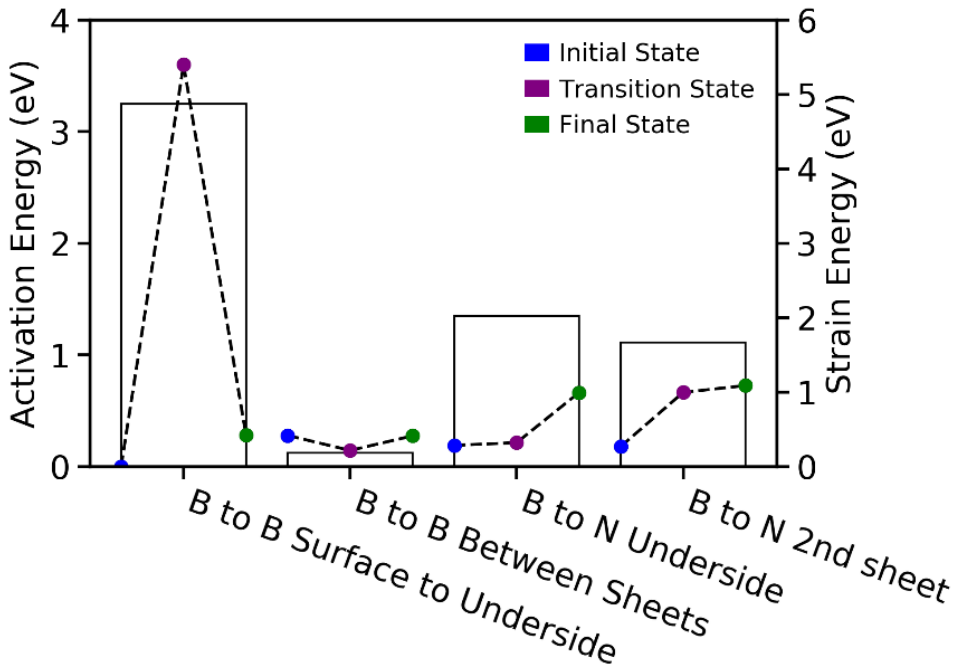

Figure 4.2 Activation energies for *h*-BN diffusion pathways (bars, left axis) and strain energies at the initial, transition, and final states, respectively, shown on the associated bar for each diffusion pathway (lines, right axis).

In addition to the appearance of mid-gap states, new states are filled between -5 eV and -10 eV of the DOS of the TS in all diffusion pathways involving a N atom (a, c, and d). The similar changes in the shapes of the DOS plots between the initial states to the TSs suggest that E_ε (i.e., distortion of the crystal structure) is a larger contributor to E_a than the redistribution of electron density. However, because the E_as for the two B-to-N surface diffusion pathways (c and d) differ from the B-to-B pathway between sheets (b) when their strain energies are very similar, the movement of electron density caused by bond formation with a N atom likely causes this disparity. The larger E_a for pathways involving a N atom than with only B atoms suggests that the transfer of electron density is energetically unfavorable, although it impacts E_a less than E_R does. This computational analysis of H diffusion in *h*-BN predicts that diffusion *through h*-BN sheets requires overcoming a substantially larger E_a than diffusion *between* sheets and, therefore, that orientation of the BN sheets on the substrate will significantly affect H diffusivity. An ideal *h*-BN EBC would

consequently be deposited with sheets parallel to the substrate surface, thereby taking advantage of the large E_a of 3.25 eV while avoiding the low energy diffusion pathways between sheets.

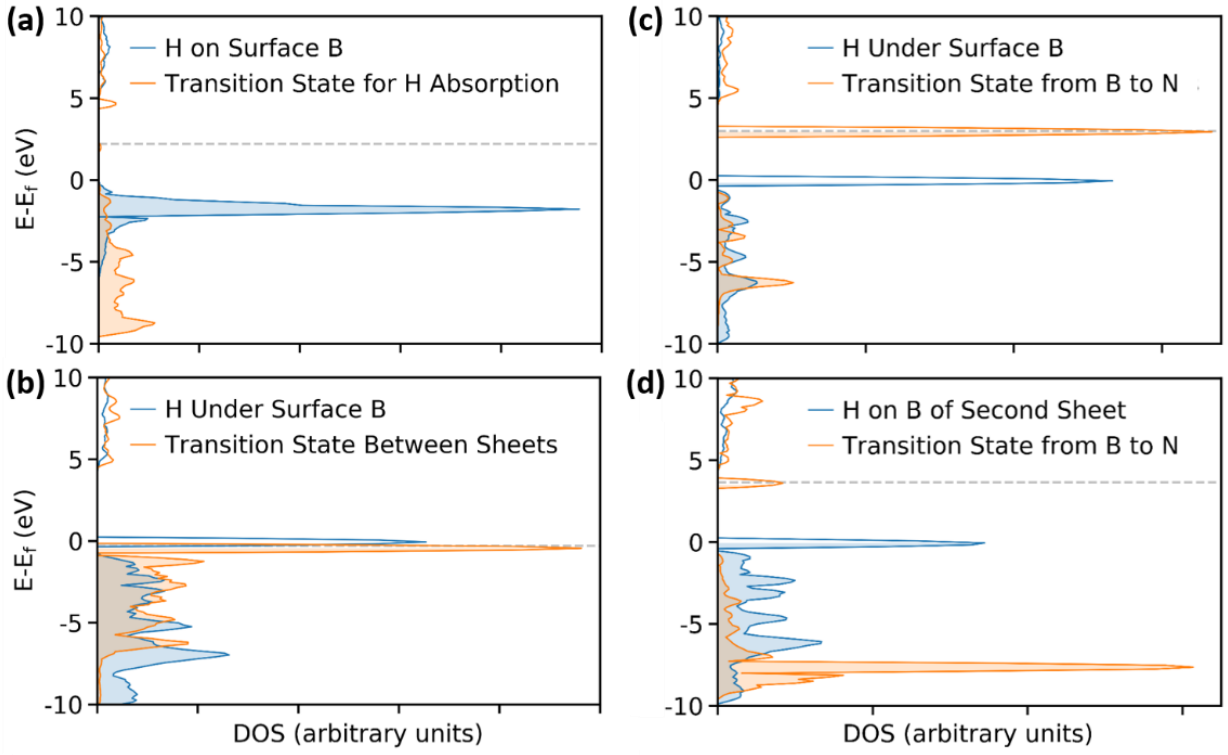

Figure 4.3 Density of states plots of projected DOS on s orbital of the diffusing H atom at the initial (blue) and transition (orange) states where the labels of panels a-d correspond to the H atom diffusion pathways shown in Figure 4.1.

4.5.2 ALD Growth

BN was deposited via ALD using BCl_3 and NH_3 precursors. Self-limiting surface chemistry was confirmed with mass spectrometry [95] where the dose times were extended beyond the required reaction times, although subsequent doses were cut off at breakthrough (Figure 4.4). Dose times lengthen with increasing total powder surface area. Dose time was therefore adjusted according to the mass of powder loaded. In each dose, the increase in the precursor signal is coupled with a sharp decrease in the byproduct signal, indicating the consumption of surface functional groups and confirming self-limiting behavior. Gaseous HCl is the major byproduct for this chemistry in both the A and B doses.

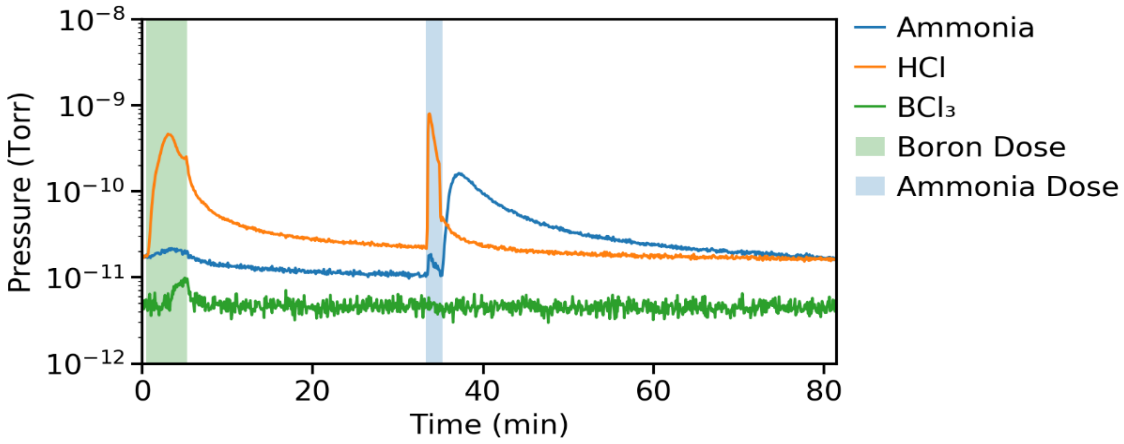

Figure 4.4 Mass spectrometer trace of a single ALD cycle of BN showing self-limited surface chemistry. The portions of the trace not highlighted indicate inert gas purges.

A BN film on coated ZrO_2 nanoparticles was confirmed by TEM where the amorphous nature of ALD films allows for clear distinction of the film from the crystalline ZrO_2 substrate. A conformal 2.5 nm BN ALD film was measured with an estimated film growth rate of 0.03 Å/cycle (Figure 4.5).

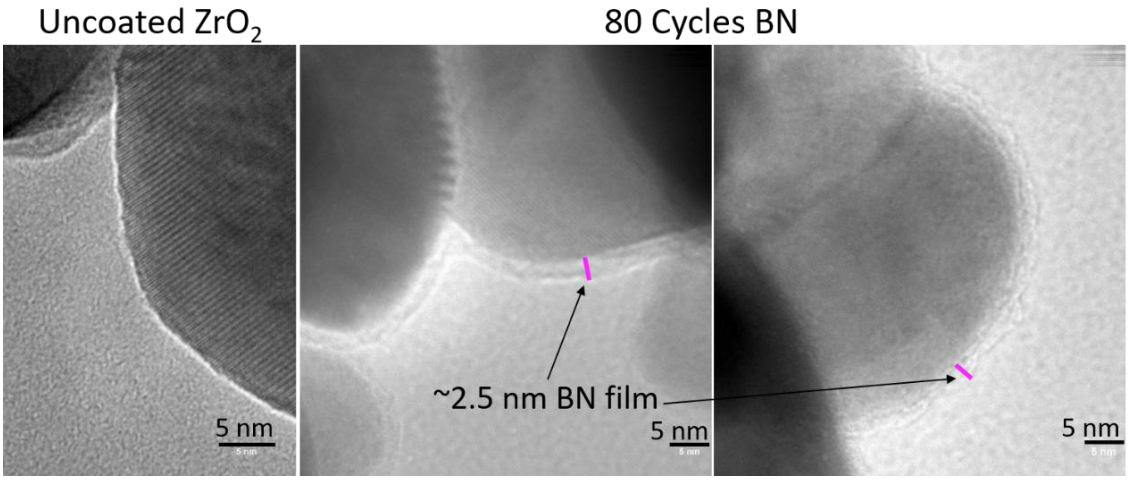

Figure 4.5 TEM micrographs of uncoated ZrO_2 and ZrO_2 coated with ~2.5 nm amorphous BN film deposited using 80 ALD cycles.

Yttria stabilized zirconia was used as a surrogate substrate for UO_2 in thermal H_2 studies due to its similar thermal expansion, particle size, and hydroxyl surface groups for ALD reactions [104-106]. Samples were coated using 115, 165, and 310 BN ALD cycles. The thickest coating

deposited using 310 ALD cycles was FIB milled and analyzed in the (S)TEM+EDS where deposition of a ~15 nm ALD film was confirmed using TEM (Figure 4.6). Large Au nanoparticles were deposited on the BN layer to mitigate sample charging, followed by deposition of a crystalline Pt overcoat to protect the sample from damage during FIB milling. The STEM+EDS spectrum over a localized area within the film confirmed the presence of B (Figure 4.7). The Fe contamination was observed as the major impurity in the coating and was likely introduced by corrosion of the inside surface of the lecture bottle containing the B precursor or from the steel reactor tube containing the powder during the coating process. The Ga and Cu present in the spectrum are due to ion implantation from the FIB and the TEM grid material, respectively.

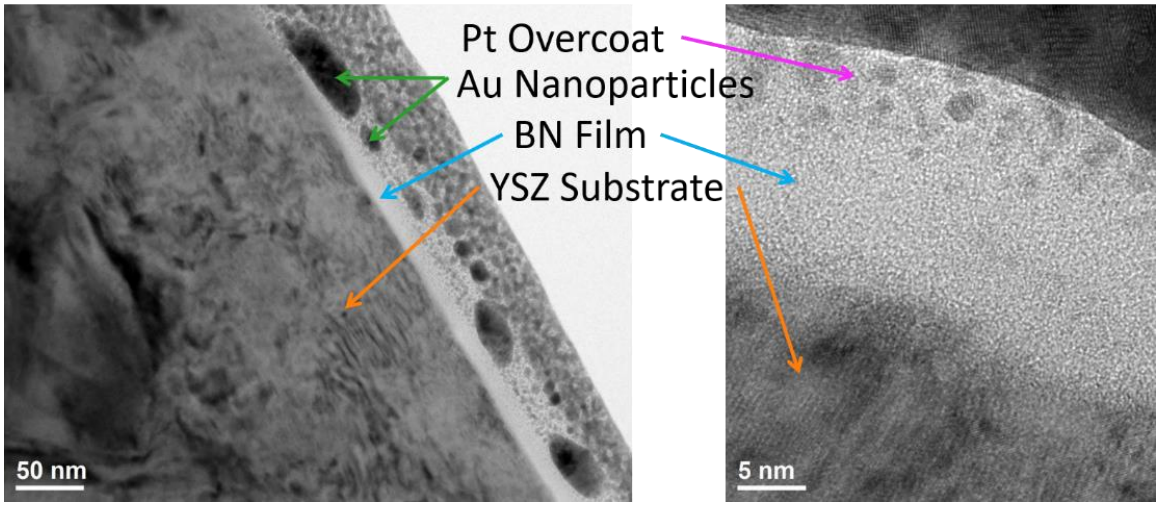

Figure 4.6 TEM micrographs of YSZ microspheres coated using 310 BN ALD cycles and prepared by FIB milling. Relevant features are highlighted, including the YSZ substrate, BN film, Au nanoparticles, and Pt overcoat. A film thickness near 15 nm was extracted from these micrographs.

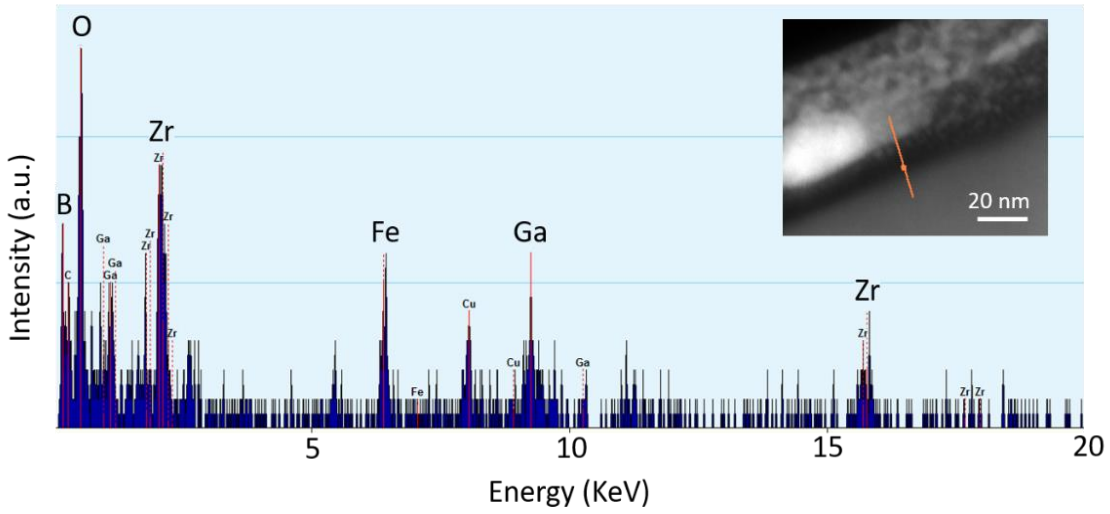

Figure 4.7 EDS spectrum of a localized area in the middle of the BN film. This area is shown as the orange dot on the inset micrograph of the same sample shown in Figure 4.6.

Elemental analysis of the coated sample surface using XPS on the 310 BN ALD sample also confirmed the presence of B and N, as well as Fe and Cl contaminants (Figure 4.8). Based on the ALD chemistry, Cl is assumed to be due to the B precursor, BCl_3. The presence of C and O in the XPS spectrum indicates that the sample surface was covered with a layer of adventitious C and O from exposure to atmosphere. This layer could not be removed due to sample charging and therefore cannot be decoupled from the intrinsic O and C content of the sample.

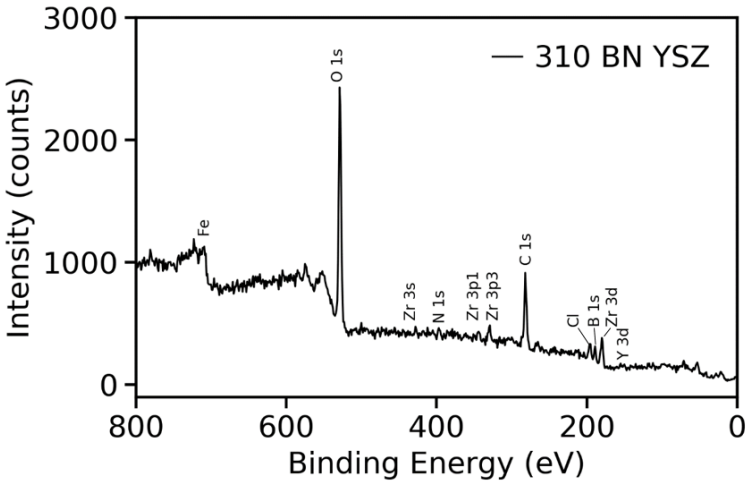

Figure 4.8 XPS spectrum of 310 BN ALD cycles (~15 nm) on YSZ microspheres that confirms the presence of B, a small amount of N, and slight amounts of Fe and Cl impurities.

4.5.3 Bulk BN stability in high temperature H_2 flow

In addition to investigating the deposition of a thin BN film, stability of bulk BN powder was computationally predicted and experimentally tested in 20% H_2 in Ar balance for three hours at 1773 K. The BN film retained nearly all of its N content throughout the experiment (Figure 4.9). This result can mostly be explained by the large N vacancy formation energy, which we calculate to be 6.3 eV at 1773 K using DFT and adjusting for the N chemical potential. Figure 4.9 shows the N vacancy formation energy at two temperatures: 1773 K and 2773 K. These temperatures were chosen to match the experimental temperature in testing bulk BN and the operating temperature of NTP engines. The positive formation energy of 5.3 eV at 2773 K suggests that the film is stable at NTP operating temperatures. The stability of *h*-BN under hot H_2 flow contributes to its desirability as a H_2 EBC and is required for the film to maintain integrity at elevated temperatures.

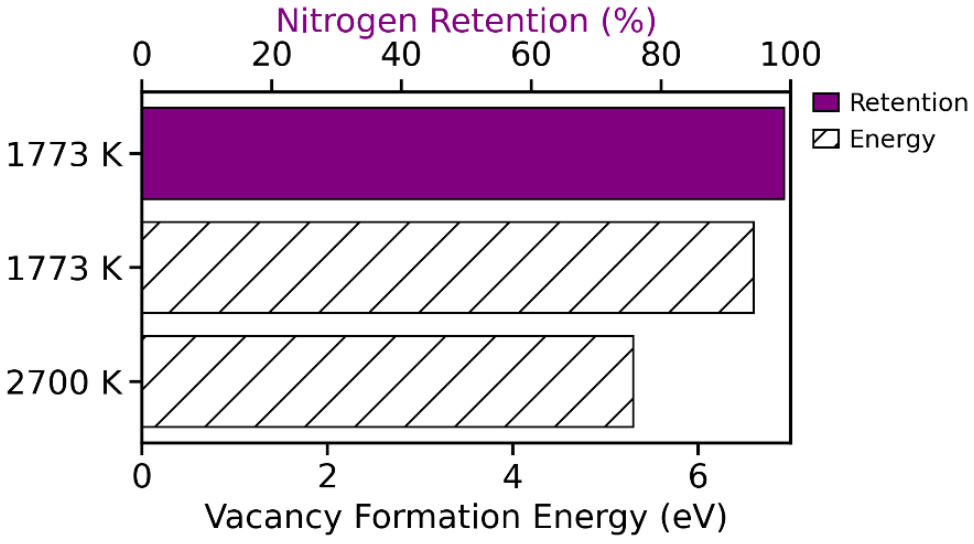

Figure 4.9 Fixed nitrogen retention (solid, top) for bulk BN powder and nitrogen vacancy formation energy from DFT calculations (striped, bottom) for bulk *h*-BN.

4.5.4 Differential thermal analysis of BN ALD films

YSZ powders coated with 115, 165, and 310 ALD cycles were tested for their resistance to reaction with H_2 using DTA (Figure 4.10). The occurrence of an exothermic process is observed for all samples at 833 K and for BN-coated samples between 953 K and 1043 K, while an endothermic event occurs in all samples above 1400 K. The gray highlighted peak is due to the tetragonal-to-cubic phase change of the yttria-stabilized tetragonal zirconia substrate. This temperature correlates well with the yttria-zirconia phase diagram [174]. The blue highlighted peak is only present in the coated samples and, therefore, likely indicates the crystallization of the amorphous BN film. These films are too thin for XRD confirmation; however, previous studies of thick CVD-deposited BN films reported film crystallization following a 1273 K anneal [175] and increasing film crystallinity of chemical vapor infiltration (CVI) BN films between 467 K and 917 K [176]. The green highlighted endothermic peaks above 1400 K indicate that the material has started to sinter, as observed in post-analysis of the final samples. These peak temperatures agree well with observations by Mazaheri et al. of sintering of 3 mol% YSZ beginning at 1373 K and continuing through 1773 K, after which further densification was not observed [177]. Additional DTA peaks are not observed within this temperature range that would indicate reaction of hydrogen with the substrate or coating. Therefore, findings from this DTA data suggest that the BN films do not react in the H_2 environment and, therefore, can be used as EBCs up to at least 1713 K.

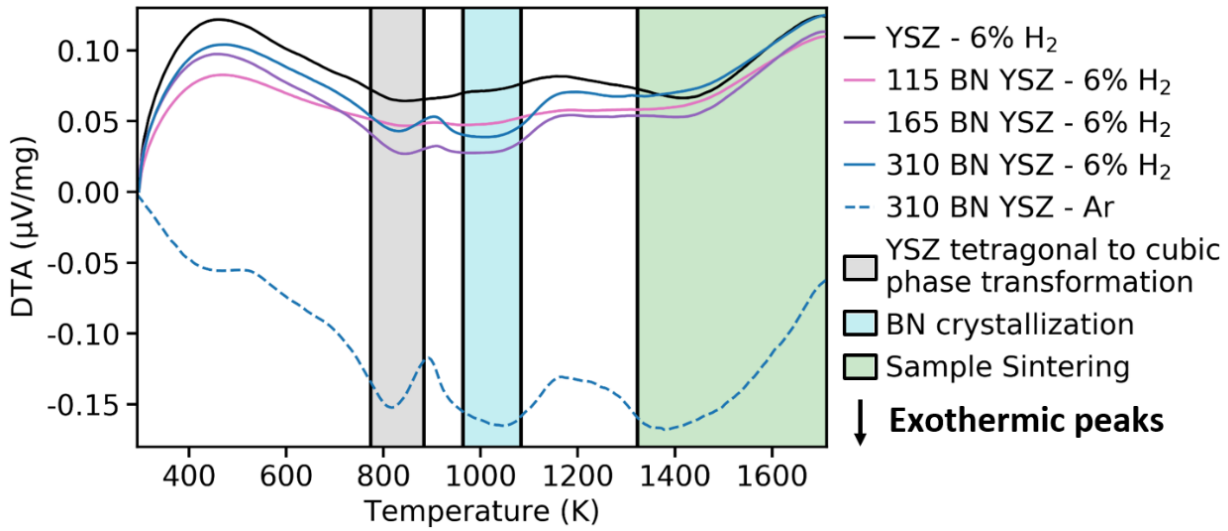

Figure 4.10 Differential thermal analysis (DTA) curves for BN-coated YSZ microspheres. Exothermic peaks are shown in the downward direction. Samples coated with 0, 115, 165, and 310 BN ALD cycles were tested in either 6% H_2 in Ar or pure Ar, as noted in the legend.

4.6 Conclusions

This study demonstrated the utility of BN deposited via ALD as a potential EBC against hot hydrogen attack in NTP engines. Atomic H diffusion was computationally analyzed in *h*-BN using DFT, and these results demonstrated that the large perturbation of both B and N atoms from their lattice sites at the TS is the main contributor to the high predicted barrier to diffusion. In addition, DOS plots of the diffusion pathways predict the formation of mid-gap states and a transfer of electron density that also contributes to the large E_a, but less so than the distortion of the lattice at the TS. The large drop in E_a from 3.25 eV to 0.12 eV for H diffusion in *h*-BN through a sheet, compared to between sheets, highlights the importance of a parallel orientation of the *h*-BN sheets relative to the substrate.

Amorphous BN coatings were deposited on ZrO_2 and YSZ substrates by ALD and tested for their efficacy as H_2 EBCs. The BN films likely crystallized during the DTA temperature ramp between 953 K and 1043 K; however, the ALD films were too thin to be confirmed with XRD. When tested using DTA in a H_2 environment, no new DTA peaks appeared in the spectrum,

compared to the inert Ar environment, indicating the stability of the film at these conditions. This supports the use of this material as an effective barrier film from room temperature up to at least 1713 K, although we suggest further high-temperature H_2 testing to demonstrate stability at nuclear thermal propulsion temperatures of >2700 K, as well as testing in more concentrated H_2 environments. Additionally, high-pressure crystallization of these films to experimentally compare the effect of crystal phase on hydrogen diffusivity is of interest because of the microstructure-dependent E_a of BN.

4.7 Acknowledgments

This work was supported by NASA ESI grant number 80NSSC18K0254. This research made use Idaho National Laboratory computing resources which are supported by the Office of Nuclear Energy of the U.S. Department of Energy and the Nuclear Science User Facilities under Contract No. DE-AC07-05ID14517. This work also utilized resources from the University of Colorado Boulder Research Computing Group, which is supported by the National Science Foundation (awards ACI-1532235 and ACI-1532236), the University of Colorado Boulder, and Colorado State University.

Chapter 5

Recommendations for future work

5.1 W via WF_6

Chapter 2 detailed the use of particle ALD to deposit WN on YSZ microspheres showing good coverage, but a low deposition rate. In addition, WN reduces to W below the operating temperatures of solid-oxide fuel cells [161], solar-thermal water splitting for hydrogen generation [178], and nuclear thermal propulsion engines [5]. This decomposition results in a volume reduction to account for in addition to the low-growth rate when determining necessary ALD cycles. Therefore, direct deposition of pure W should be investigated. Common precursors for this deposition are tungsten hexafluoride (WF_6) and disilane (Si_2H_6). However, WF_6 is substrate selective and will deposit W with a slight nucleation delay on alumina, significantly delayed on silica, and etch titania [54]. The longer the nucleation delay, the larger the surface roughness [179].

Deposition on YSZ was investigated in this dissertation with WF_6 and Si_2H_6, and an extreme nucleation delay was observed with 23 W ALD cycles before byproducts were observed in the mass spectrometer. After a total of 45 W ALD cycles nanoparticle formation on the YSZ surface was observed using SEM (Figure 5.1). After 100 ALD cycles, W islands had formed from the nucleation sites, which are evident as bright nanoparticles on the YSZ surface (Figure 5.2) and were confirmed with EDS. However, full coverage of the oxide substrate was still not observed.

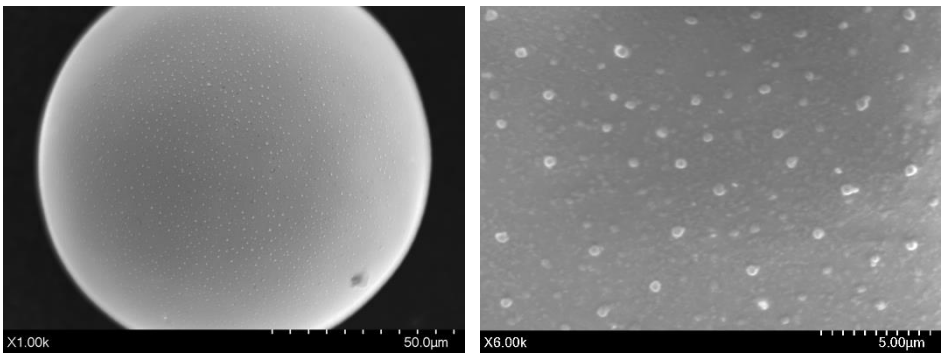

Figure 5.1 Disperse W nanoparticles on 100 µm diameter YSZ surface after 45 W ALD cycles

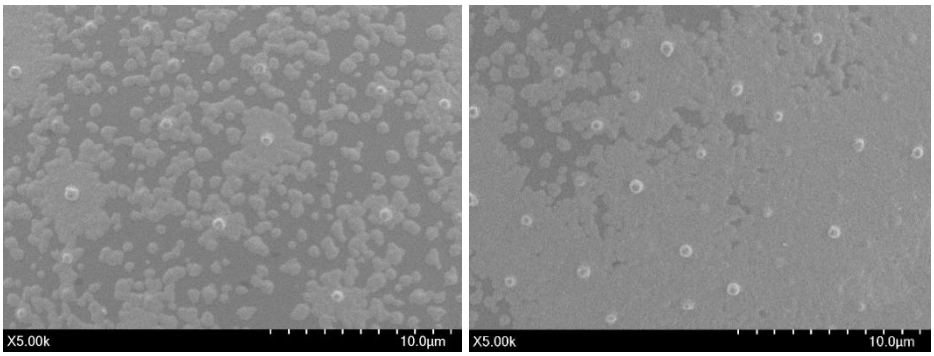

Figure 5.2 Island formation and nucleation sites after 100 W ALD cycles on 100 µm diameter YSZ substrate

The nucleation delay and non-conformal deposition on YSZ elicits the need to use an adhesion layer between the oxide substrate and metal film. A thin film of WN which was shown previously to uniformly coat this same YSZ substrate in Chapter 1 should be tested as an adhesion layer between the metal oxide and the metallic W coating. Deposition of W via ALD has previously been achieved on top of transition metal nitride films used as barriers to protect Si before metallization including TiN [180], TaN [181], and W_xN [182]. Given the beneficial effect on WF_6 reactivity observed through DFT analysis of reacting the TiN surface with borane to form B-N bonds on the surface before the WF_6 dose [180], it is also possible that BN, already shown in Chapter 4 to conformally coat the YSZ substrate, can also act as an adhesion layer for WF_6 ALD. The use of BN as an adhesion layer should, however, be analyzed for etching by the precursor and HF byproducts due to the volatility of boron trifluoride. The presence of a bandgap in BN compared to the metallic nature of the density of states in WN could affect choice of adhesion layer material for a desired application.

5.2 Additional testing of promising barrier materials

In Chapters 2 and 4, the effect of H_2 atmosphere during temperature ramps were probed on WN and BN thin films. The equipment limited the maximum H_2 content to 6%, however, further testing should be completed on the coated samples in higher H_2concentrations and at higher

temperatures. Because BN was observed to be inert to H_2 flow in these studies, it is a promising candidate for further testing at NTP conditions which represents one of the harshest environments for barrier coatings.

5.3 DFT analysis of highly permeable materials

In Chapter 3, *ab initio* studies of atomic H diffusion in refractory materials revealed *h*-BN, *c*-BN, HfN, ZrN, and WC as candidates for experimental testing. Three main material characteristics were probed: DOS plots, strain energies, and Bader charges and correlated to E_as for H diffusion into the first subsurface layer. In order to further study these material properties, they should be compared to materials with high H diffusivities such as vanadium and palladium [47] to probe how H interacts with a substrate that it can easily permeate through. In addition, calculation of pre-exponential factors should be completed to compare across materials screened in this work.

References

[1] K. Saikia, B.K. Kakati, B. Boro, A. Verma, Current Advances and Applications of Fuel Cell Technologies, in: P.K. Sarangi, S. Nanda, P. Mohanty (Eds.) Recent Advancements in Biofuels and Bioenergy Utilization, Springer Singapore, Singapore, 2018, pp. 303-337.

[2] G. Marbán, T. Valdés-Solís, Towards the hydrogen economy?, International Journal of Hydrogen Energy, 32 (2007) 1625-1637.

[3] G.W. Look, M.I. Baskes, Hydrogen profiles in tokamak fusion reactor first walls, Journal of Nuclear Materials, 85-86 (1979) 995-999.

[4] M. Claessens, ITER: The Giant Fusion Reactor: Bringing a Sun to Earth, Springer International Publishing, 2019.

[5] S.K. Borowski, D.R. McCurdy, T.W. Packard, Nuclear Thermal Propulsion (NTP): A proven growth technology for human NEO/Mars exploration missions, in: 2012 IEEE Aerospace Conference, 2012, pp. 1-20.

[6] H.R. Gray, H.G. Nelson, R.E. Johnson, W.B. McPherson, F.S. Howard, J.H. Swisher, Potential structural material problems in a hydrogen energy system, International Journal of Hydrogen Energy, 3 (1978) 105-118.

[7] I.M. Robertson, P. Sofronis, A. Nagao, M. Martin, S. Wang, D. Gross, K. Nygren, Hydrogen embrittlement understood, Metallurgical and Materials Transactions B, 46 (2015) 1085-1103.

[8] M.R. Louthan, Hydrogen Embrittlement of Metals: A Primer for the Failure Analyst, Journal of Failure Analysis and Prevention, 8 (2008) 289-307.

[9] D. Hardie, E.A. Charles, A.H. Lopez, Hydrogen embrittlement of high strength pipeline steels, Corrosion Science, 48 (2006) 4378-4385.

[10] C.J. Beevers, G.T. Newman, Hydrogen embrittlement in uranium, Journal of Nuclear Materials, 23 (1967) 10-18.

[11] T. Michler, M. Lindner, U. Eberle, J. Meusinger, Assessing hydrogen embrittlement in automotive hydrogen tanks, in, 2012, pp. 94-125.

[12] R. Jones, 14 - Gaseous hydrogen embrittlement of high performance metals in energy systems: future trends, in: R.P. Gangloff, B.P. Somerday (Eds.) Gaseous Hydrogen Embrittlement of Materials in Energy Technologies, Woodhead Publishing, 2012, pp. 471-484.

[13] B.N. Popov, Chapter 8 - Hydrogen Permeation and Hydrogen-Induced Cracking, in: B.N. Popov (Ed.) Corrosion Engineering, Elsevier, Amsterdam, 2015, pp. 327-364.

[14] W.H. Johnson, On Some Remarkable Changes Produced in Iron and Steel by the Action of Hydrogen and Acids, Nature, 11 (1875) 393-393.

[15] H.K.D.H. Bhadeshia, Prevention of Hydrogen Embrittlement in Steels, ISIJ International, 56 (2016) 24-36.

[16] M. Koyama, M. Rohwerder, C.C. Tasan, A. Bashir, E. Akiyama, K. Takai, D. Raabe, K. Tsuzaki, Recent progress in microstructural hydrogen mapping in steels: quantification, kinetic analysis, and multi-scale characterisation, Materials Science and Technology, 33 (2017) 1481-1496.

[17] W.R. Corliss, F.C. Schwenk, Nuclear Propulsion for Space, Taylor & Francis, 1968.

[18] M.G. Houts, D.P. Mitchell, K. Aschenbrenner, Low-Enriched Uranium Nuclear Thermal Propulsion Systems, in: 2017 AAS Guidance and Control Conference.

[19] M.E.M. Stewart, A Historical Review of Cermet Fuel Development and the Engine Performance Implications, in: Nuclear and Emerging Technologies for Space 2015, Albuquerque, New Mexico, 2015.

[20] R. Hickman, J. Broadway, O. Mireles, Fabrication and Testing of CERMET Fuel Materials for Nuclear Thermal Propulsion, in: 48th AIAA/ASME/SAE/ASEE Joint Propulsion Conference, Atlanta, GA, 2012.

[21] A. Loui, The Hydrogen Corrosion of Uranium: Identification of Underlying Causes and Proposed Mitigation Strategies, in, Laurence Livermore National Lab, California, 2012.

[22] J. Roth, K. Schmid, Hydrogen in tungsten as plasma-facing material, Physica Scripta, T145 (2011) 014031.

[23] L. Chen, J.L. Fan, H.R. Gong, Atomistic simulation of mechanical properties of tungsten-hydrogen system and hydrogen diffusion in tungsten, Solid State Communications, 306 (2020) 113772.

[24] D.F. Johnson, E.A. Carter, Hydrogen in tungsten: Absorption, diffusion, vacancy trapping, and decohesion, Journal of Materials Research, 25 (2010) 315-327.

[25] M.G. Houts, D.P. Mitchell, T. Kim, W.J. Emrich, R.R. Hickman, H.P. Gerrish, NASA's Nuclear Thermal Propulsion Project, (2015) 1-10.

[26] V. Cremers, R.L. Puurunen, J. Dendooven, Conformality in atomic layer deposition: Current status overview of analysis and modelling, Applied Physics Reviews, 6 (2019) 021302.

[27] S.M. George, Atomic Layer Deposition: An Overview, Chemical Reviews, 110 (2010) 111-131.

[28] S. Yang, F. Zhang, H. Ding, P. He, H. Zhou, Lithium Metal Extraction from Seawater, Joule, 2 (2018) 1648-1651.

[29] A.M. Bradshaw, T. Hamacher, U. Fischer, Is nuclear fusion a sustainable energy form?, Fusion Engineering and Design, 86 (2011) 2770-2773.

[30] J. Dietz, T. The Iter Joint Central, The Iter fusion experiment, Vacuum, 47 (1996) 911-918.

[31] G.W. Hollenberg, E.P. Simonen, G. Kalinin, A. Terlain, Tritium/hydrogen barrier development, Fusion Engineering and Design, 28 (1995) 190-208.

[32] D.L. Smith, J. Konys, T. Muroga, V. Evitkhin, Development of coatings for fusion power applications, Journal of Nuclear Materials, 307-311 (2002) 1314-1322.

[33] T. Hua, R. Ahluwalia, L. Eudy, G. Singer, B. Jermer, N. Asselin-Miller, S. Wessel, T. Patterson, J. Marcinkoski, Status of hydrogen fuel cell electric buses worldwide, Journal of Power Sources, 269 (2014) 975-993.

[34] D. Nash, D. Aklil, E. Johnson, R. Gazey, V. Ortisi, 4.05 - Hydrogen Storage: Compressed Gas, in: A. Sayigh (Ed.) Comprehensive Renewable Energy, Elsevier, Oxford, 2012, pp. 131-155.

[35] C. Henager, Hydrogen Permeation Barrier Coatings, in: R.H. Jones, G.J. Thomas (Eds.) Materials for the Hydrogen Economy, CRC Press, Florida, 2007, pp. 181-190.

[36] P. Korinko, T. Adams, G. Creech, Hydrogen permeation resistant coatings, in: Materials for the Hydrogen Economy, 2005, pp. 91-100.

[37] S.K. Bull, W.W. McNeary, C.A. Adkins, T.A. Champ, C.A. Hill, R.C. O'Brien, C.B. Musgrave, A.W. Weimer, Atomic layer deposition of tungsten nitride films as protective barriers to hydrogen, Applied Surface Science, 507 (2020) 145019.

[38] T.-H. Nam, J.-H. Lee, S.-R. Choi, J.-B. Yoo, J.-G. Kim, Graphene coating as a protective barrier against hydrogen embrittlement, International Journal of Hydrogen Energy, 39 (2014) 11810-11817.

[39] M. Tamura, M. Noma, M. Yamashita, Characteristic change of hydrogen permeation in stainless steel plate by BN coating, Surface and Coatings Technology, 260 (2014) 148-154.

[40] N. Fernandez, Y. Ferro, D. Kato, Hydrogen diffusion and vacancies formation in tungsten: Density Functional Theory calculations and statistical models, Acta Materialia, (2015) 307-318.

[41] X.-S. Kong, S. Wang, X. Wu, Y.-W. You, C.S. Liu, Q.F. Fang, J.-L. Chen, G.N. Luo, First-principles calculations of hydrogen solution and diffusion in tungsten: Temperature and defect-trapping effects, Acta Materialia, 84 (2015) 426-435.

[42] Y.-N. Liu, T. Ahlgren, L. Bukonte, K. Nordlund, X. Shu, Y. Yu, X.-C. Li, G.-H. Lu, Mechanism of vacancy formation induced by hydrogen in tungsten, AIP Advances, 3 (2013) 122111.

[43] Y.-N. Liu, T. Wu, Y. Yu, X.-C. Li, X. Shu, G.-H. Lu, Hydrogen diffusion in tungsten: A molecular dynamics study, Journal of Nuclear Materials, 455 (2014) 676-680.

[44] P.M. Piaggi, E.M. Bringa, R.C. Pasianot, N. Gordillo, M. Panizo-Laiz, J. Del Río, C. Gómez De Castro, R. Gonzalez-Arrabal, Hydrogen diffusion and trapping in nanocrystalline tungsten, Journal of Nuclear Materials, 458 (2015) 233-239.

[45] E. Serra, G. Benamati, O.V. Ogorodnikova, Hydrogen isotopes transport parameters in fusion reactor materials, Journal of Nuclear Materials, 255 (1998) 105-115.

[46] A. Moitra, K. Solanki, Adsorption and penetration of hydrogen in W: A first principles study, Computational Materials Science, 50 (2011) 2291-2294.

[47] P. Ferrin, S. Kandoi, A.U. Nilekar, M. Mavrikakis, Hydrogen adsorption, absorption and diffusion on and in transition metal surfaces: A DFT study, Surface Science, 606 (2012) 679-689.

[48] L. Sun, S. Jin, X.-C. Li, Y. Zhang, G.-H. Lu, Hydrogen behaviors in molybdenum and tungsten and a generic vacancy trapping mechanism for H bubble formation, Journal of Nuclear Materials, 434 (2013) 395-401.

[49] W.M. Shu, K. Isobe, T. Yamanishi, Temperature dependence of blistering and deuterium retention in tungsten exposed to high-flux and low-energy deuterium plasma, Fusion Engineering and Design, 83 (2008) 1044-1048.

[50] J.S. Becker, R.G. Gordon, Diffusion barrier properties of tungsten nitride films grown by atomic layer deposition from bis(tert-butylimido)bis(dimethylamido)tungsten and ammonia, Applied Physics Letters, 82 (2003) 2239-2241.

[51] B.-l. Park, J.-m. Ha, D.-h. Ko, S.-i. Lee, Method for manufacturing a capacitor in a semiconductor device using selective tungsten nitride thin film, in, Google Patents, 1998.

[52] S. Anwar, S. Anwar, Thermal stability studies of tungsten nitride thin films, Surface Engineering, 33 (2017) 276-281.

[53] J.S. Becker, S. Suh, S. Wang, R.G. Gordon, Highly Conformal Thin Films of Tungsten Nitride Prepared by Atomic Layer Deposition from a Novel Precursor, Chemistry of Materials, 15 (2003) 2969-2976.

[54] P.C. Lemaire, M. King, G.N. Parsons, Understanding inherent substrate selectivity during atomic layer deposition: Effect of surface preparation, hydroxyl density, and metal oxide composition on nucleation mechanisms during tungsten ALD, The Journal of chemical physics, 146 (2017) 052811.

[55] J.D. Ferguson, A.W. Weimer, S.M. George, Atomic layer deposition of boron nitride using sequential exposures of BCl3 and NH3, Thin Solid Films, 413 (2002) 16-25.

[56] M. Weber, E. Coy, I. Iatsunskyi, L. Yate, P. Miele, M. Bechelany, Mechanical properties of boron nitride thin films prepared by atomic layer deposition, CrystEngComm, 19 (2017) 6089-6094.

[57] P.R. Nalla, N.S. Tjokro, A. Kolics, S. Varadarajan, Through silicon via metallization, in, Google Patents, 2015.

[58] T. Taniguchi, K. Kimoto, M. Tansho, S. Horiuchi, S. Yamaoka, Phase Transformation of Amorphous Boron Nitride under High Pressure, Chemistry of Materials, 15 (2003) 2744-2751.

[59] R. Checchetto, A. Chayahara, H. Horino, A. Miotello, K. Fujii, A study of deuterium permeation through thin BN films, Thin Solid Films, 299 (1997) 5-9.

[60] R. Checchetto, A. Miotello, Deuterium diffusion through hexagonal boron nitride thin films, Journal of Applied Physics, 87 (2000) 110-116.

[61] L. He, H. Wang, L. Chen, X. Wang, H. Xie, C. Jiang, C. Li, K. Elibol, J. Meyer, K. Watanabe, T. Taniguchi, Z. Wu, W. Wang, Z. Ni, X. Miao, C. Zhang, D. Zhang, H. Wang, X. Xie, Isolating hydrogen in hexagonal boron nitride bubbles by a plasma treatment, Nature Communications, 10 (2019) 2815.

[62] F. Grillo, J.A. Moulijn, M.T. Kreutzer, J.R. van Ommen, Nanoparticle sintering in atomic layer deposition of supported catalysts: Kinetic modeling of the size distribution, Catalysis Today, 316 (2018) 51-61.

[63] A.W. Weimer, Particle atomic layer deposition, Journal of Nanoparticle Research, 21 (2019) 9.

[64] Q.H. Powell, G.P. Fotou, T.T. Kodas, B.M. Anderson, Y. Guo, Gas-phase coating of TiO2 with SiO2 in a continuous flow hot-wall aerosol reactor, Journal of Materials Research, 12 (1997) 552-559.

[65] J.R. Scheffe, A. Francés, D.M. King, X. Liang, B.A. Branch, A.S. Cavanagh, S.M. George, A.W. Weimer, Atomic layer deposition of iron(III) oxide on zirconia nanoparticles in a fluidized bed reactor using ferrocene and oxygen, Thin Solid Films, 517 (2009) 1874-1879.

[66] L.F. Hakim, J. Blackson, S.M. George, A.W. Weimer, Nanocoating Individual Silica Nanoparticles by Atomic Layer Deposition in a Fluidized Bed Reactor, Chemical Vapor Deposition, 11 (2005) 420-425.

[67] M. Ritala, M. Leskelä, J.-P. Dekker, C. Mutsaers, P.J. Soininen, J. Skarp, Perfectly Conformal TiN and Al2O3 Films Deposited by Atomic Layer Deposition, Chemical Vapor Deposition, 5 (1999) 7-9.

[68] G. Kresse, J. Furthmüller, Efficiency of ab-initio total energy calculations for metals and semiconductors using a plane-wave basis set, Computational Materials Science, 6 (1996) 15-50.

[69] G. Kresse, J. Furthmüller, Efficient iterative schemes for ab initio total-energy calculations using a plane-wave basis set, Physical Review B, 54 (1996) 11169-11186.

[70] G. Kresse, D. Joubert, From ultrasoft pseudopotentials to the projector augmented-wave method, Physical Review B, 59 (1999) 1758-1775.

[71] G. Kresse, J. Hafner, Ab initio molecular dynamics for liquid metals, Physical Review B, 47 (1993) 558-561.

[72] G. Kresse, J. Hafner, Ab initio molecular-dynamics simulation of the liquid-metal–amorphous-semiconductor transition in germanium, Physical Review B, 49 (1994) 14251-14269.

[73] J.P. Perdew, K. Burke, M. Ernzerhof, Generalized Gradient Approximation Made Simple, Physical Review Letters, 77 (1996) 3865-3868.

[74] E. Schrödinger, An Undulatory Theory of the Mechanics of Atoms and Molecules, Physical Review, 28 (1926) 1049-1070.

[75] M. Born, R. Oppenheimer, Zur Quantentheorie der Molekeln, Annalen der Physik, 389 (1927) 457-484.

[76] P. Hohenberg, W. Kohn, Inhomogeneous Electron Gas, Physical Review, 136 (1964) B864-B871.

[77] W. Kohn, L.J. Sham, Self-Consistent Equations Including Exchange and Correlation Effects, Physical Review, 140 (1965) A1133-A1138.

[78] M. Leskelä, M. Ritala, Atomic layer deposition (ALD): from precursors to thin film structures, Thin Solid Films, 409 (2002) 138-146.

[79] H. Chung, L. Chen, Integration of ALD tantalum nitride and alpha-phase tantalum for copper metallization application, in, Google Patents, 2003.

[80] J. Uhm, H. Jeon, TiN Diffusion Barrier Grown by Atomic Layer Deposition Method for Cu Metallization, Japanese Journal of Applied Physics, 40 (2001) 4657-4660.

[81] G. Beyer, A. Satta, J. Schuhmacher, K. Maex, W. Besling, O. Kilpela, H. Sprey, G. Tempel, Development of sub-10-nm atomic layer deposition barriers for Cu/low-k interconnects, Microelectronic Engineering, 64 (2002) 233-245.

[82] G. Wang, J. Luo, J. Liu, T. Yang, Y. Xu, J. Li, H. Yin, J. Yan, H. Zhu, C. Zhao, T. Ye, H.H. Radamson, pMOSFETs Featuring ALD W Filling Metal Using SiH4 and B2H6 Precursors in 22 nm Node CMOS Technology, Nanoscale Research Letters, 12 (2017) 306.

[83] S.-H. Kim, S.S. Oh, K.-B. Kim, D.-H. Kang, W.-M. Li, S. Haukka, M. Tuominen, Atomic-layer-deposited WNxCy thin films as diffusion barrier for copper metallization, Applied Physics Letters, 82 (2003) 4486-4488.

[84] J.B. Kim, S.-H. Kim, W.S. Han, D.-J. Lee, Atomic layer deposited nanocrystalline tungsten carbides thin films as a metal gate and diffusion barrier for Cu metallization, Journal of Vacuum Science & Technology A, 34 (2016) 041504.

[85] W. Keuning, P.v.d. Weijer, H. Lifka, W.M.M. Kessels, M. Creatore, Cathode encapsulation of organic light emitting diodes by atomic layer deposited Al2O3 films and Al2O3/a-SiNx:H stacks, Journal of Vacuum Science & Technology A, 30 (2012) 01A131.

[86] J. Speulmanns, A.M. Kia, K. Kühnel, S. Bönhardt, W. Weinreich, Surface-Dependent Performance of Ultrathin TiN Films as an Electrically Conducting Li Diffusion Barrier for Li-Ion-Based Devices, ACS Applied Materials & Interfaces, 12 (2020) 39252-39260.

[87] A.L. Hoskins, A.H. Coffey, C.B. Musgrave, A.W. Weimer, Nanostructured Mullite Steam Oxidation Resistant Coatings for Silicon Carbide Deposited via Atomic Layer Deposition, Journal of the American Ceramic Society, (2018).

[88] D.K. Ross, Hydrogen storage: The major technological barrier to the development of hydrogen fuel cell cars, Vacuum, 80 (2006) 1084-1089.

[89] T. Nishikiori, T. Nohira, Y. Ito, Hydrogen Impermeability of TiN Films and Its Dependence on Nitrogen Concentration at High Temperatures, Journal of The Electrochemical Society, 148 (2001) E52.

[90] R. Checchetto, M. Bonelli, L. Gratton, a. Miotello, a. Sabbioni, L. Guzman, Y. Horino, G. Benamati, Analysis of the hydrogen permeation properties of TiN-TiC bilayers deposited on martensitic stainless steel, Surface and Coatings Technology, 83 (1996) 40-44.

[91] D.F. Johnson, E.A. Carter, Hydrogen in tungsten: Absorption, diffusion, vacancy trapping, and decohesion, Journal of Materials Research, 25 (2010) 315-327.

[92] Iaea, Thermophysical Properties of Materials for Nuclear Engineering: A Tutorial and Collection of Data, in: International Atomic Energy Agency, 2008, pp. 200.

[93] F. Nix, D. MacNair, The Thermal Expansion of Pure Metals. II:Molybdenum, Palladium, Silver, Tantalujm, Tungsten, Platinum, and Lead, Phys. Rev., 61 (1941) 74.

[94] A.I. Fedorchenko, A.-B. Wang, H.H. Cheng, Thickness dependence of nanofilm elastic modulus, Applied Physics Letters, 94 (2009) 152111.

[95] D.M. King, J.A. Spencer, X. Liang, L.F. Hakim, A.W. Weimer, Atomic layer deposition on particles using a fluidized bed reactor with in situ mass spectrometry, Surface and Coatings Technology, 201 (2007) 9163-9171.

[96] J.F. Moulder, W.F. Stickle, P.E. Sobol, K.D. Bomben, Handbook of X-ray Photoelectron Spectroscopy: A Reference Book of Standard Spectra for Identification and Interpretation of XPS Data, Physical Electronics Division, Perkin-Elmer Corporation, 1992.

[97] P. Xiao, D. Sheppard, J. Rogal, G. Henkelman, Solid-state dimer method for calculating solid-solid phase transitions, The Journal of chemical physics, 140 (2014) 174104.

[98] W. Tang, E. Sanville, G. Henkelman, A grid-based Bader analysis algorithm without lattice bias, Journal of physics. Condensed matter : an Institute of Physics journal, 21 (2009) 084204.

[99] G. Henkelman, H. Jónsson, A dimer method for finding saddle points on high dimensional potential surfaces using only first derivatives, The Journal of chemical physics, 111 (1999) 7010-7022.

[100] D. Sheppard, P. Xiao, W. Chemelewski, D.D. Johnson, G. Henkelman, A generalized solid-state nudged elastic band method, The Journal of chemical physics, 136 (2012) 074103.

[101] R.F.W. Bader, Atoms in Molecules: A Quantum Theory, Clarendon Press, 1994.

[102] A. Rugge, J.S. Becker, R.G. Gordon, S.H. Tolbert, Tungsten Nitride Inverse Opals by Atomic Layer Deposition, Nano Letters, 3 (2003) 1293-1297.

[103] L.F. Hakim, S.M. George, A.W. Weimer, Conformal nanocoating of zirconia nanoparticles by atomic layer deposition in a fluidized bed reactor, Nanotechnology, 16 (2005) S375-S381.

[104] A. Dabrowski, V.A. Tertykh, Adsorption on New and Modified Inorganic Sorbents, Elsevier Science, 1996.

[105] C.P. Kempter, R.O. Elliott, Thermal Expansion of <UN>, <UO_2>, <$UO_2 \cdot ThO_2$>, and <ThO_2>, The Journal of chemical physics, 30 (1959) 1524-1526.

[106] H. Hayashi, T. Saitou, N. Maruyama, H. Inaba, K. Kawamura, M. Mori, Thermal expansion coefficient of yttria stabilized zirconia for various yttria contents, Solid State Ionics, 176 (2005) 613-619.

[107] G.V. Samsonov, Nitridy., Naukova Dumka, Kiev, Ukraine, 1969.

[108] Y.G. Shen, Y.W. Mai, D.R. McKenzie, Q.C. Zhang, W.D. McFall, W.E. McBride, Composition, residual stress, and structural properties of thin tungsten nitride films deposited by reactive magnetron sputtering, Journal of Applied Physics, 88 (2000) 1380-1388.

[109] K. Heinola, T. Ahlgren, Diffusion of hydrogen in bcc tungsten studied with first principle calculations, Journal of Applied Physics, 107 (2010) 113531.

[110] J. Greeley, M. Mavrikakis, Surface and Subsurface Hydrogen: Adsorption Properties on Transition Metals and Near-Surface Alloys, The Journal of Physical Chemistry B, 109 (2005) 3460-3471.

[111] M.R. Louthan, Hydrogen embrittlement of metals: A primer for the failure analyst, Journal of Failure Analysis and Prevention, 8 (2008) 289-307.

[112] M. Tamura, T. Eguchi, Nanostructured thin films for hydrogen-permeation barrier, Journal of Vacuum Science & Technology A, 33 (2015) 041503.

[113] A.K. Misra, Thermodynamic analysis of chemical stability of ceramic materials in hydrogen-containing atmospheres at high temperatures Final report, in, United States, 1990, pp. 26.

[114] G. Murray, J. Bouffard, D. Briggs, Retardation of hydrogen embrittlement of 17-4ph stainless steels by nonmetallic surface layers, Metallurgical Transactions A, 18 (1987) 162-164.

[115] R.R. Hickman, J.W. Broadway, O.R. Mireles, N. Marshall, S. Flight, Fabrication and Testing of CERMET Fuel Materials for Nuclear Thermal Propulsion, in: AIAA/ASME/SAE/ASEE Joint Propulsion Conference, 2012, pp. 23.

[116] E.S. Solntceva, M.L. Taubin, N.A. Bochkov, V.A. Solntsev, A.A. Yaskolko, Use of tungsten single crystals to enhance nuclear reactors structural elements properties, International Journal of Hydrogen Energy, 41 (2016) 7206-7212.

[117] V.F. Sears, Neutron scattering lengths and cross sections, Neutron News, 3 (1992) 26-37.

[118] R.A. Barker, P.J. Estrup, Hydrogen on tungsten(100): Adsorbate-induced surface reconstruction, Physical Review Letters, 41 (1978) 1307-1310.

[119] H.-B. Zhou, Y.-L. Liu, S. Jin, Y. Zhang, G.-N. Luo, G.-H. Lu, Investigating behaviours of hydrogen in a tungsten grain boundary by first principles: from dissolution and diffusion to a trapping mechanism, Nuclear Fusion, 50 (2010) 025016.

[120] R. Frauenfelder, Permeation of Hydrogen through Tungsten and Molybdenum, The Journal of Chemical Physics, 48 (1968) 3954-3965.

[121] L. Sun, S. Jin, X.C. Li, Y. Zhang, G.H. Lu, Hydrogen behaviors in molybdenum and tungsten and a generic vacancy trapping mechanism for H bubble formation, Journal of Nuclear Materials, 434 (2013) 395-401.

[122] A.P. Zakharov, V.M. Sharapov, E.I. Evko, Hydrogen permeability of polycrystalline and monocrystalline molybdenum and tungsten, Soviet Materials Science, 9 (1975) 149-153.

[123] R.A. Causey, R.A. Karnesky, C. San Marchi, Tritium barriers and tritium diffusion in fusion reactors, Comprehensive Nuclear Materials, 4 (2012) 511-549.

[124] K.S. Forcey, A. Perujo, F. Reiter, P.L. Lolli-Coreni, The Formation of Tritium Permeation Barriers by CVD, 200 (1993) 417-420.

[125] J. Sun, A. Ruzsinszky, J.P. Perdew, Strongly Constrained and Appropriately Normed Semilocal Density Functional, Physical Review Letters, 115 (2015) 036402.

[126] P.E. Blöchl, Projector augmented-wave method, Physical Review B, 50 (1994) 17953-17979.

[127] A. Jain, S.P. Ong, G. Hautier, W. Chen, W.D. Richards, S. Dacek, S. Cholia, D. Gunter, D. Skinner, G. Ceder, K.A. Persson, Commentary: The Materials Project: A materials genome approach to accelerating materials innovation, APL Materials, 1 (2013) 011002.

[128] G. Henkelman, H. Jónsson, Improved tangent estimate in the nudged elastic band method for finding minimum energy paths and saddle points, The Journal of chemical physics, 113 (2000) 9978-9985.

[129] G. Henkelman, B.P. Uberuaga, H. Jónsson, A climbing image nudged elastic band method for finding saddle points and minimum energy paths, The Journal of chemical physics, 113 (2000) 9901-9904.

[130] J. Kästner, P. Sherwood, Superlinearly converging dimer method for transition state search, The Journal of chemical physics, 128 (2008) 014106.

[131] A. Heyden, A.T. Bell, F.J. Keil, Efficient methods for finding transition states in chemical reactions: Comparison of improved dimer method and partitioned rational function optimization method, The Journal of chemical physics, 123 (2005) 224101.

[132] G. Henkelman, A. Arnaldsson, H. Jónsson, A fast and robust algorithm for Bader decomposition of charge density, Computational Materials Science, 36 (2006) 354-360.

[133] E. Sanville, S.D. Kenny, R. Smith, G. Henkelman, Improved grid-based algorithm for Bader charge allocation, J Comput Chem, 28 (2007) 899-908.

[134] M. Yu, D.R. Trinkle, Accurate and efficient algorithm for Bader charge integration, J Chem Phys, 134 (2011) 064111.

[135] C. Wert, C. Zener, Interstitial Atomic Diffusion Coefficients, Physical Review, 76 (1949) 1169-1175.

[136] R. Frauenfelder, Solution and Diffusion of Hydrogen in Tungsten, Journal of Vacuum Science and Technology, 6 (1969) 388-397.

[137] T. Ahlgren, L. Bukonte, Concentration dependent hydrogen diffusion in tungsten, Journal of Nuclear Materials, 479 (2016) 195-201.

[138] T.M. Duncan, R.A. Levy, P.K. Gallagher, M.W.W. Jr., Structural characterization of boron nitride films, Journal of Applied Physics, 64 (1988) 2990-2994.

[139] K.J. Yang, Y.-L. Liu, P. Shao, X. Zhang, Q.-F. Han, Y. Ma, H permeation in molybdenum: temperature dependence and compensation effect from first-principles simulation, Journal of Nuclear Science and Technology, 56 (2019) 1014-1028.

[140] X.-Y. Yang, Y. Lu, P. Zhang, First-principles study of the stability and diffusion properties of hydrogen in zirconium carbide, Journal of Nuclear Materials, 479 (2016) 130-136.

[141] I. Salehinia, I. Mastorakos, H.M. Zbib, Effects of Defects on Hydrogen Diffusion in NbC, Applied Surface Science, 401 (2017) 198-205.

[142] J. Greeley, M. Mavrikakis, Surface and Subsurface Hydrogen: Adsorption Properties on Transition Metals and Near-Surface Alloys, The Journal of Physical Chemistry B, 109 (2005) 3460-3471.

[143] V. Gupta, A. Kumar, N. Ray, Rapid communication: Permeability of hydrogen in two-dimensional graphene and hexagonal boron nitride sheets, Pramana, 91 (2018) 64.

[144] J. Osorio-Guillén, S. Lany, S.V. Barabash, A. Zunger, Magnetism without magnetic ions: percolation, exchange, and formation energies of magnetism-promoting intrinsic defects in CaO, Phys Rev Lett, 96 (2006) 107203.

[145] J. M.W. Chase, NIST-JANAF thermochemical tables, fourth edition, in, J. Phys. Chem. Ref. Data, Monogr. 9, 1998.

[146] R. Hao, J. Shi, L. Zhu, L. Ji, T. Sun, S. Feng, A first-principle study on adsorption of atomic hydrogen on the two-dimensional hexagonal boron nitride monolayer, Superlattices and Microstructures, 111 (2017) 696-703.

[147] H. Ruuska, K. Larsson, Surface reactivities of (111), (100), and (110) planes of c-BN: A quantum mechanical approach, Diamond and Related Materials, 16 (2007) 118-123.

[148] M. Siodmiak, N. Govind, J. Andzelm, N. Tanpipat, G. Frenking, A. Korkin, Theoretical Study of Hydrogen Adsorption and Diffusion on TiN(100) Surface, physica status solidi (b), 226 (2001) 29-36.

[149] Y. Abghoui, E. Skúlason, Hydrogen Evolution Reaction Catalyzed by Transition-Metal Nitrides, The Journal of Physical Chemistry C, 121 (2017) 24036-24045.

[150] E. Osei-Agyemang, J.F. Paul, R. Lucas, S. Foucaud, S. Cristol, Periodic DFT and Atomistic Thermodynamic Modeling of Reactivity of H2, O2, and H2O Molecules on Bare and Oxygen Modified ZrC (100) Surface, The Journal of Physical Chemistry C, 118 (2014) 12952-12961.

[151] S.-P. Gao, Crystal structures and band gap characters of h-BN polytypes predicted by the dispersion corrected DFT and GW method, Solid State Communications, 152 (2012) 1817-1820.

[152] X. Zhang, J. Meng, Chapter 4 - Recent progress of boron nitrides, in: M. Liao, B. Shen, Z. Wang (Eds.) Ultra-Wide Bandgap Semiconductor Materials, Elsevier, 2019, pp. 347-419.

[153] H. Li, J. Robertson, Behaviour of hydrogen in wide band gap oxides, Journal of Applied Physics, 115 (2014) 203708.

[154] L. Pauling, THE NATURE OF THE CHEMICAL BOND. IV. THE ENERGY OF SINGLE BONDS AND THE RELATIVE ELECTRONEGATIVITY OF ATOMS, Journal of the American Chemical Society, 54 (1932) 3570-3582.

[155] J.C. Slater, Atomic Radii in Crystals, The Journal of chemical physics, 41 (1964) 3199-3204.

[156] Y.-W. You, X.-S. Kong, X.-B. Wu, Q.F. Fang, J.-L. Chen, G.N. Luo, C.S. Liu, Effect of vacancy on the dissolution and diffusion properties of hydrogen and helium in molybdenum, Journal of Nuclear Materials, 433 (2013) 167-173.

[157] E. Hayward, C.-C. Fu, Interplay between hydrogen and vacancies in α-Fe, Physical Review B, 87 (2013) 174103.

[158] D.R. Jennison, P.A. Schultz, J.P. Sullivan, Evidence for interstitial hydrogen as the dominant electronic defect in nanometer alumina films, Physical Review B, 69 (2004) 041405.

[159] H.O. Pierson, Handbook of refractory carbides & nitrides: properties, characteristics, processing and applications, William Andrew, 1996.

[160] S. Semboshi, N. Masahashi, S. Hanada, Multiple cracking of tantalum by hydrogenation, Metallurgical and Materials Transactions A, 34 (2003) 685-690.

[161] N. Mahato, A. Banerjee, A. Gupta, S. Omar, K. Balani, Progress in material selection for solid oxide fuel cell technology: A review, Progress in Materials Science, 72 (2015) 141-337.

[162] M.W. Melaina, O. Antonia, M. Penev, Blending Hydrogen into Natural Gas Pipeline Networks: A Review of Key Issues, in, ; National Renewable Energy Lab. (NREL), Golden, CO (United States), 2013, pp. Medium: ED; Size: 4.0 MB.

[163] D.F. Johnson, E.A. Carter, Hydrogen in tungsten: Absorption, diffusion, vacancy trapping, and decohesion, Journal of Materials Research, 25 (2011) 315-327.

[164] M. Stewart, B.G. Schnitzler, A Comparison of Materials Issues for Cermet and Graphite-Based NTP Fuels, in: 49th AIAA/ASME/SAE/ASEE Joint Propulsion Conference.

[165] S.A. Shevlin, Z.X. Guo, Hydrogen sorption in defective hexagonal BN sheets and BN nanotubes, Physical Review B, 76 (2007) 024104.

[166] R.H. Knibbs, The measurement of thermal expansion coefficient of tungsten at elevated temperatures, Journal of Physics E: Scientific Instruments, 2 (1969) 515-517.

[167] S.K. Singh, M. Neek-Amal, S. Costamagna, F.M. Peeters, Thermomechanical properties of a single hexagonal boron nitride sheet, Physical Review B, 87 (2013) 184106.

[168] D. Sheppard, G. Henkelman, Paths to which the nudged elastic band converges, Journal of Computational Chemistry, 32 (2011) 1769-1771.

[169] D. Sheppard, R. Terrell, G. Henkelman, Optimization methods for finding minimum energy paths, The Journal of chemical physics, 128 (2008) 134106.

[170] H. Jónsson, G. Mills, K.W. Jacobsen, Nudged elastic band method for finding minimum energy paths of transitions, (1998).

[171] M. Yu, D.R. Trinkle, Accurate and efficient algorithm for Bader charge integration, The Journal of chemical physics, 134 (2011) 064111.

[172] Y. An, A. Kuc, P. Petkov, M. Lozada-Hidalgo, T. Heine, On the Chemistry and Diffusion of Hydrogen in the Interstitial Space of Layered Crystals h-BN, MoS_2, and Graphite, Small, 15 (2019) 1901722.

[173] S.S. Zumdahl, Introductory Chemistry: A Foundation, 5th ed., Houghton Mifflin, Boston, MA, 2002.

[174] H.G. Scott, Phase relationships in the zirconia-yttria system, Journal of Materials Science, 10 (1975) 1527-1535.

[175] Y. Shi, C. Hamsen, X. Jia, K.K. Kim, A. Reina, M. Hofmann, A.L. Hsu, K. Zhang, H. Li, Z.-Y. Juang, M.S. Dresselhaus, L.-J. Li, J. Kong, Synthesis of Few-Layer Hexagonal Boron Nitride Thin Film by Chemical Vapor Deposition, Nano Letters, 10 (2010) 4134-4139.

[176] J. Dai, Y. Wang, Z. Xu, R. Mu, L. He, Influence of BCl_3/NH_3 flow ratio on growth and microstructure of CVI-processed boron nitride interfacial coatings, Vacuum, 179 (2020) 109484.

[177] M. Mazaheri, A. Simchi, F. Golestani-Fard, Densification and grain growth of nanocrystalline 3Y-TZP during two-step sintering, Journal of the European Ceramic Society, 28 (2008) 2933-2939.

[178] C.L. Muhich, B.D. Ehrhart, I. Al-Shankiti, B.J. Ward, C.B. Musgrave, A.W. Weimer, A review and perspective of efficient hydrogen generation via solar thermal water splitting, WIREs Energy and Environment, 5 (2016) 261-287.

[179] J. Elam, C. Nelson, R. Grubbs, S. George, Nucleation and growth during tungsten atomic layer deposition on SiO2 surfaces, Thin Solid Films, 386 (2001) 41-52.

[180] H. Park, S. Lee, H.J. Kim, D. Woo, J.M. Lee, E. Yoon, G.-D. Lee, Overall reaction mechanism for a full atomic layer deposition cycle of W films on TiN surfaces: first-principles study, RSC Advances, 8 (2018) 39039-39046.

[181] H. Chung, R. Wang, N. Maity, Atomic layer deposition of tantalum based barrier materials, in, Google Patents, 2007.

[182] J.P. Lu, W.Y. Hsu, J.D. Luttmer, L.K. Magel, H.L. Tsai, A New Process for Depositing Tungsten Nitride Thin Films, Journal of The Electrochemical Society, 145 (1998) L21-L23.